DESIGN AND CONSTRUCTION OF A MACH 2 WIND TUNNEL FOR CAVITY ACOUSTICS RESEARCH

by

Brian P. Davis

A Thesis Submitted to the Graduate Faculty of
Auburn University
In Partial Fulfillment of the
Requirements for the Degree of
Master of Science

Auburn, Alabama
May 5, 2013

Wind Tunnel Design and Development, Cavity Acoustics, Aero Acoustics

Approved by

Anwar Ahmed, Chair Professor of Aerospace Engineering
John Cochran, Department Head of Aerospace Engineering
Roy Hartfield, Professor of Aerospace Engineering

Abstract

Cavity flow is encountered in many practical applications of ground and air vehicles operating at high speed. Examples include airflow past open windows, sunroofs, and wheel-wells of automobiles as well as landing gear and weapon bays of aircraft. Cavity flow becomes a design consideration at high-speeds hence research in the area of supersonic cavity acoustics is more motivated by military applications. In a typical cavity, the compressible shear layer separating from the front end of a cavity impinges on the rear wall and initiates a sequence of events consisting of intense edge tones, high decibel acoustics and resonance that leads to fluid-structure coupling, unsteady loads, and structural vibrations. Furthermore, the trajectories of the weapons released from an internal weapon bay become unpredictable resulting in the released store hitting the carrier. A Mach 2 wind tunnel was designed using the method of characteristics with a viscous approximation to conduct research is the area of cavity flow acoustics. Unique features of the supersonic wind tunnel include a modular design for quick changes in cavity configuration and optical access from all sides for qualitative and quantitative design techniques including multiple plane schlieren/shadowgraphy, anemometry, particle image velocimetry and high speed photography. The designed nozzle blocks and windows were machined on a CNC machine of the AE machine shop and assembled in the aerodynamics lab. Pressure signal histories and schlieren images suggest that the wind tunnel operated at designed values.

Acknowledgments

I would like to thank God our father for all the talents and opportunities I have received. I could not have finished this thesis without the love and support of my wife, parents, and extended family. A special thanks to Frank Collazo for his extra contribution without which my education could not have been completed at Auburn University. I would like to show my appreciation to the guidance and patience of advisors, Dr. Anwar Ahmed, Dr. Roy Hartfield and Dr. John Cochran over the two years of the program. I would like to thank Andy Weldon for machining and assembly work, welding, and for practical advice in mechanical designs.

Table of Contents

List of Tables

List of Figures

List of Abbreviations

bar	Bar (unit) Pressure
dB	Decibels (unit)
in	Inches (unit)
K	Kelvin (unit)
m	Meters (unit)
M	Mach Number (unit)
MoC	Method of Characteristics
mm	Millimeters (unit)
ms	Milliseconds (unit)
mW	Milliwatts (unit)
nm	Nanometers (unit)
psia	Pressure per Square Inch Atmosphere (unit)
psig	Pressure per Square Inch Gage (unit)
µs	Microseconds

List of Nomenclature

a	Speed of Sound (ft/s)	R	Gas Constant (J/(mol K))
A	Area (in^2)	R_n	Frequency (n-Mode)
A_{ratio}	Area Ratio	St	Strouhal Number
C_p	Pressure Coefficient	T	Temperature (K)
D	Depth (in)	U_C	Convective Velocity
l	Length (in)	U_∞	Free-stream Velocity
L	Stream-wise Length (in)	V	Local Flow Velocity
f	Frequency (Hz)	α	Rossiter Empirical Constant
f_{tones}	Tone Frequency (Hz)	β	Compressibility Factor
K_+	Right Running Characteristic	γ	Specific Heat Ratio
M	Local Mach Number	ε	Phase Constant
n_c	Number of Characteristics	θ	Flow Turning Angle (deg)
p	Pressure	$\theta_{characteristic}$	Characteristic Angle (deg)
p_0	Total Pressure	$\theta_{toal\ corner\ angle}$	Total Corner Angle (deg)
p_{abs}	Absolute Pressure	μ	Mach Angle
p_{amb}	Ambient Pressure	ν	Prandtl-Meyer Angle
p_{gage}	Gage Pressure	ρ	Density
p_{vac}	Vacuum Pressure		

Chapter 1

INTRODUCTION

Cavity flows are encountered in various practical applications such as landing gear bays, weapons bays, automobile sunroofs, flush inlets, base heating in missiles, optical ports and can even be observed in partially deflected flaps and the recessed areas on wrap-around-fin missiles that contain fins before they are deployed. Interest in cavity flows at high speed is driven by acoustic couplings in weapons bays. Because of the need for stealth operation and minimizing the drag due to externally mounted deliverables, the new generation of fighter/bomber is designed to carry weapons internally. At the time of delivery, however, large unsteady loads are encountered when the weapon bay doors are opened. The weapons bay thus acts a classical cavity. One such weapons bay is shown in Figure 1.

Figure 1: F-35 Weapon Bay

1.1 Fundamentals of Cavity Acoustics and Cavity Flow

1.1.1 Engineering Challenges

Understanding the engineering challenges of cavity flow is essential to development of high-speed vehicles that are subjected to increased design and performance requirements. An open aircraft weapons bay presents both steady and unsteady loads induced on stores (munitions) at the time of release. The trajectories of the weapons released form an internal weapon bay often become unpredictable resulting in the released store, in some instances, hitting the carrier aircraft. In aircraft stores separation, steady flows tend to cause large nose-up pitching moments on stores and structural vibrations in addition to a significant increase in drag. The flow field accompanied by high intensity pressure fluctuations within rectangular cavity flow is very complex. The interaction between the oscillating shear layer impinging on the trailing edge produces intense acoustic disturbances up to 170 dB.

Resonant modes generated by fluid traversing the cavities causes other undesirable affects such as vibration, structural damage to aircraft and stores, in addition to noise. Chan [1] pointed out that stealth aircraft exhibiting a noise signature from cavity acoustics could compromise the stealth capability.

Flow-acoustic coupling originates when the boundary layer separates at the leading edge due to the sudden discontinuity in cavity geometry. A shear layer forms whereby the Kelvin–Helmholtz instability mechanism triggers coherent vortical structures. The shear layer oscillates transversely and impinges on the trailing edge of the cavity, as shown in Figure 2. This interaction generates acoustic waves which travel upstream. In supersonic flow, disturbances do

not travel upstream, however, within a cavity, there exists a region or multiple regions of locally subsonic flow [2].

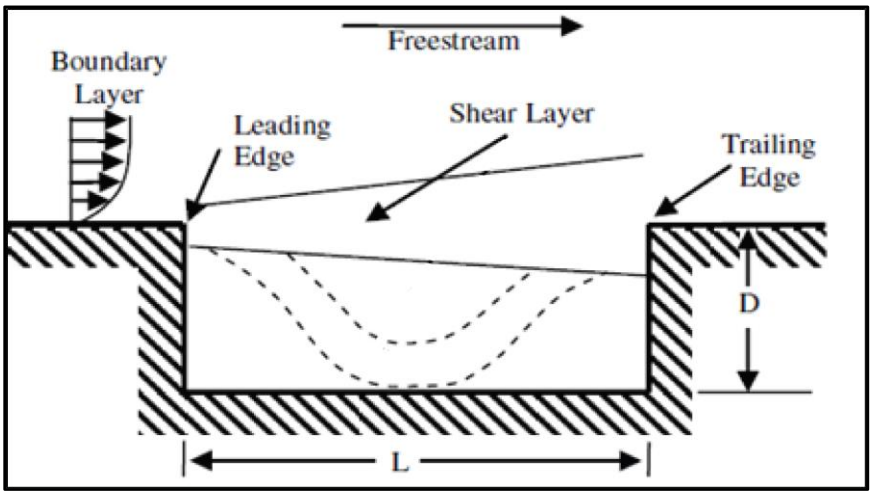

Figure 2: Basic Cavity Flow

The acoustic waves carry energy which, upon arriving at the leading edge, add energy to the shear layer and establish a feedback loop. For the situation in which the frequency of the acoustic waves coincide with the frequency of the coherent structures in the shear layer, acoustic resonance results. This amplifies the normal modes of the shear layer as a consequence of the feedback described in Figure 3.

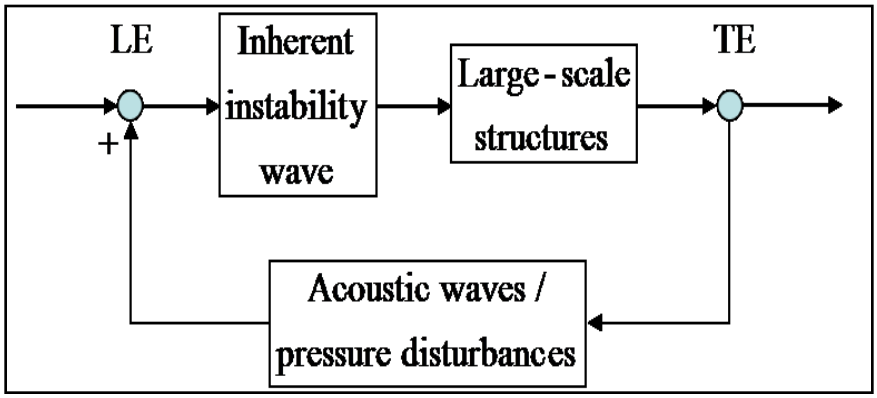

Figure 3: Acoustic Feedback Loop

1.1.2 Types of Cavity Flow

Important geometric parameters that govern cavity fluid dynamics are length to depth ratio (L/D), Mach number, and the ratio of boundary layer height to cavity height. Depending on the length to depth ratio (L/D), flows are classified as open, closed, or transitional open or transitional closed. Open Cavity flow consists of the range of length to depth ratio up to 10 and closed greater than or equal to 13. Furthermore, the tone amplitudes and bandwidths are dramatically different from subsonic to transonic to supersonic Mach numbers and through different length to depth ratios. Acoustic tones occur at discrete frequencies that correspond to standing waves or modes in the cavity and therefore exhibit a distinct pressure pattern that can be studied.

Figure 4 illustrates a subsonic open cavity flow that is characterized by dividing streamline spanning the open cavity, separation point at forward face, and stagnation point at rear face. This usually occurs when the cavity is “deep” and such cavities are found in the bomb bays of long range bombers (B-52, B-1, B-2 etc.).

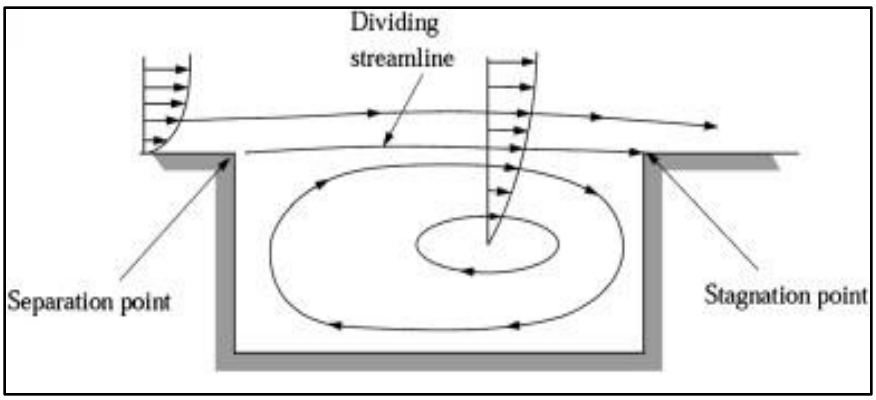

Figure 4: Subsonic Open Cavity Flow [2]

Unlike their closed flow broadband counterparts, open flow regimes tend to exhibit distinct peaks in measured sound pressure spectra. A shear layer "bridges" the cavity and a weak shock wave can form near the leading edge of the cavity as a result of the flow being compressed slightly by the shear layer. A nearly uniform static pressure distribution is produced when the cavity flow is open which is desirable if a successful separation of the store is the objective. However, the open cavity is fraught with high intensity acoustic tones inducing vibrations in the surrounding structure that may lead to structural fatigue.

Figure 5 illustrates a subsonic closed cavity flow and the flow is characterized by a dividing streamline, a forward separation point, an intermediary impingement point followed by separation point, and stagnation point at the rear face. With acoustic spectra that follow a more broadband acoustic distribution, closed cavity flows are associated with "shallow" cavities.

The flow separates at the leading edge of the cavity and reattaches somewhere along the floor of the cavity. The flow then proceeds to separate again near the trailing edge, or rear face of the closed cavity. Characterized by these two separation points, adverse static pressure gradients contribute to a large nose-up pitching moment of whatever stores that may be released from the cavity. Acoustic tones are typically nonexistent for shallow cavities. The local flows over the

cavity front and rear faces are very similar to the flows over rearward-facing and forward-facing steps, respectively [2].

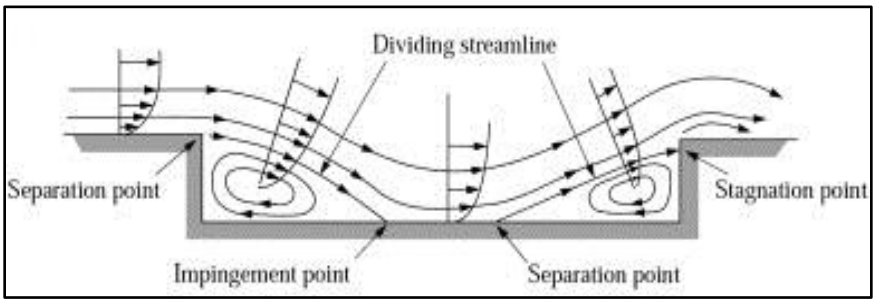

Figure 5: Subsonic Closed Cavity Flow [2]

Figure 6 depicts a supersonic open cavity flow and is characterized by a forward separation point, rear stagnation point and a shear layer spanning the cavity. The pressure coefficients over the cavity floor are slightly positive and relatively uniform with the exception of a small adverse gradient occurring ahead of the rear face at the shear layer impingement location.

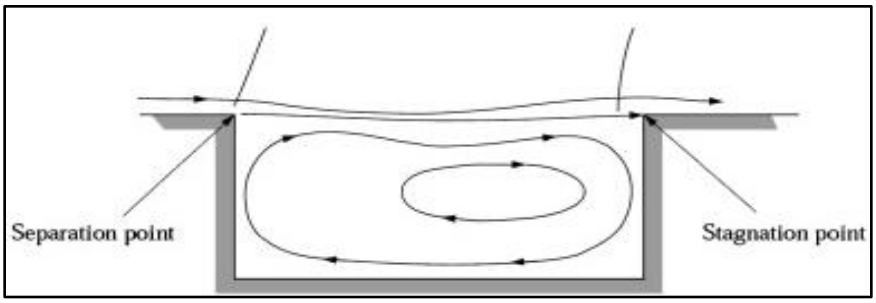

Figure 6: Supersonic Open Cavity Flow [2]

Figure 7 depicts a supersonic closed cavity flow and is characterized by a forward separation point where an expansion fan is often located, an exit shock, a rear stagnation point, an intermediary impingement point but with a floor impingement shock. Supersonic closed

cavity flow generally occurs where L/D ≥ 13. During supersonic closed cavity flow, the shear layer expands at the cavity leading edge, impinges on the cavity floor and exits ahead of the rear face. Low base pressures occur at the backstep. Higher pressure is registered at the reattachment point and continues to increase as the flow approaches the rear wall [2].

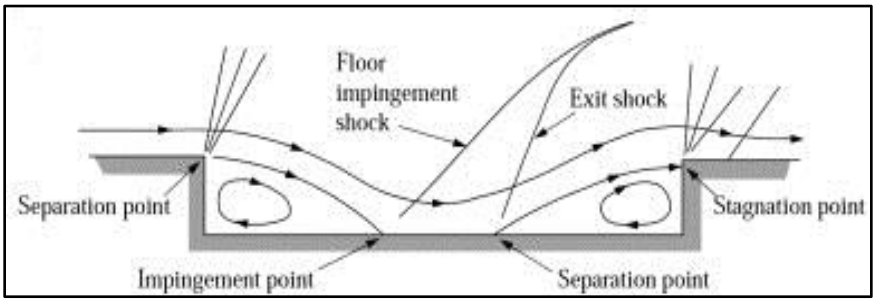

Figure 7: Supersonic Closed Cavity Flow [2]

Transitional open and transitional closed cavity flows are sometimes referred to as "mean" flow types. This is because they occur for length to depth ratios that fall in between those for open and closed cavities, usually found to be for 10 ≤ L/D ≥ 13. In cases of supersonic transitional flow, the exit shock that normally occurs for closed cavity flow can coincide with the floor impingement shock to yield a single shock thereby producing a large longitudinal pressure gradient. A small reduction in the length to depth ratio moves the flow regime to a transitional open cavity flow without a large longitudinal pressure gradient. The acoustic fields for the transitional open cavity flow are not well established as pointed out by Tracy and Plentovisch. It is known that for transitional flow types the shear layer turns through an angle to exit from the cavity coincident with impinging on the cavity floor resulting in the impingement shock and the exit shock of closed cavity flow collapsing into a single wave [2].

Figure 8 describes the trends of pressure coefficient as it varies with length to depth ratio. The l/h ratio is equivalent to the L/D ratio discussed in this section. As the length to depth ratio increases from values corresponding to open cavity flow to those associated with closed cavity flow, the pressure spectra becomes increasingly nonlinear as the flow regime undergoes changes. The critical values for which transitional flows occur vary according to the experimental conditions must be experimentally obtained for a specific aerodynamic configuration.

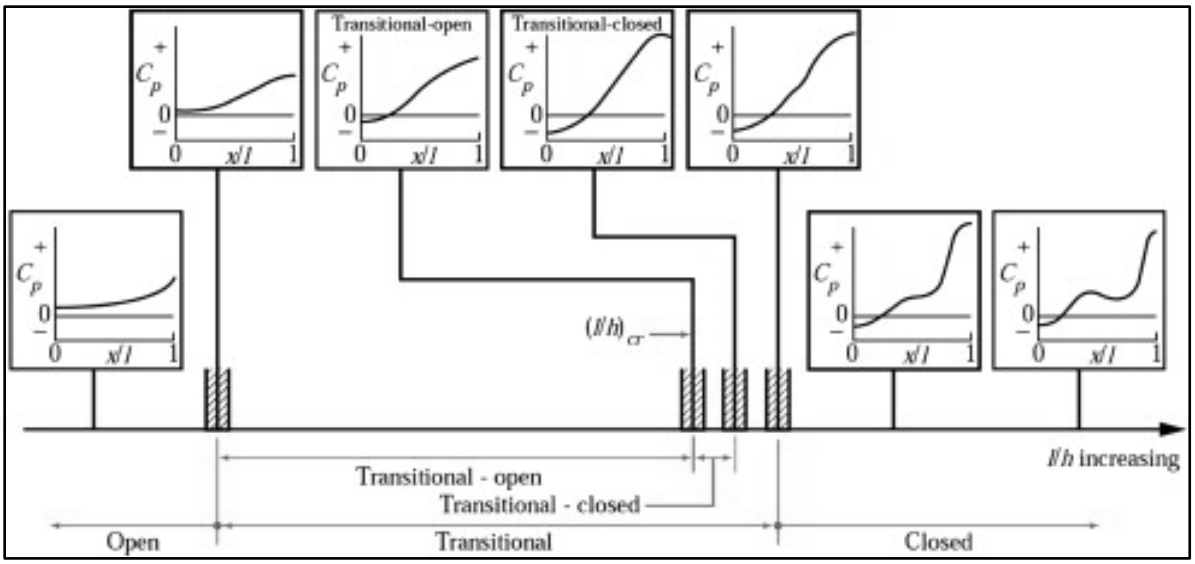

Figure 8: Pressure Coefficient of Cavity Flows for Increasing L/D [2]

1.1.3 Shear Layer Oscillations and Resonance

Compressible turbulent flows consist of eddy motions of different scales and of compressed/expanded motions such as acoustic and shock waves. These constituent motions have their own energy that can be either kinetic or internal energy. Interaction among different motions of compressible turbulent flows is generally accompanied by the transfer and/or exchange of energy [3]. Acoustic waves play a leading role in the exchange of energy. Large-scale motions are first generated by the action of some external forces, and subsequently small-

scale motions are excited through nonlinear couplings among different scales of turbulence [3]. The flow instability, indicated by the presence of feedback oscillations, is responsible for wall pressure fluctuations, pressure drag and aerodynamic noise radiation [4].

Strouhal number, or the reduced frequency, is a Mach number dependent variable and is often used to characterize the feedback oscillations. The L/D ratio plays an instrumental role in the relaxation of sound waves by the bottom floor of the cavity [5]. Similarly, the ratio of cavity length to the thickness of the shear layer also affects the Strouhal number. However, in older works the thickness of the shear layer was not measured. First examples of the "Rossiter modes", which are merely the first few peaks in frequency, were identified by Rossiter through examining plots of Strouhal number vs. Mach number [6].

In the time-averaged flow, the presence of the shear layer, its rate of growth once separated from the forward face of the cavity, the pressure distribution around the walls, the characteristics of the in-coming boundary layer, and the characteristics of the re-attached flow downstream of the cavity all influence the cavity mean drag [4].

Cavity flow is dominated by the convective amplification of the large-scale instability in the shear layer and of the accompanying unsteady convected vorticity. The shear layer interaction at the downstream cavity edge dominates the pressure fluctuations throughout the cavity [4].

Experiments indicate a varying shear layer growth in the spanwise direction. Often within one cavity height of the leading edge the shear layer develops as a free shear layer [4]. It is this shear layer oscillation that "drives" the self-sustaining flow-instability. The growth rate of the shear layer and the normal displacement of the shear layer vary in the streamwise direction that leads to complex wave patterns, aerodynamic noise, above the rectangular cavity [4]. This

combination of interactions constitutes an unsteady aerodynamic pressure field. Areas of high acoustic strength are found at the cavity edges. The vortex roll up near the upstream edge and the unsteady mass exchange near the downstream edge provide the fluctuations in momentum flux necessary for noise generation [4]. Because of those reasons the geometric modifications to the front and rear edges are acceptable as plausible solutions to reduce aerodynamic noise and cavity drag as well.

It should be noted that the shear layer spanning a cavity is not simply a mixing layer. Cavity shear layers differ in two important aspects. As Rowley and Basu point out, the intense acoustic environment is constantly exciting instabilities and the entrainment is modified by the presence of the cavity, and they suggest using vorticity thickness within a shear layer as a source of instability [7].

1.2 History of Cavity Acoustics

Crocco and Lee published a very general integral approach to the calculation of laminar and turbulent separated flow-fields thereby establishing a way to evaluate cavity flows [8].

As early as 1954 Norton investigated the bomb bay of a B47 aircraft for military purposes and noted that the bomb bay induced buffeting [9].

Krishnamurthy extensively studied the problem of sound radiating out of the cavity. He was the first to conclude that the phenomenon was likely to be associated with the inherent instability of the separated boundary layer, which permits amplification of disturbances within certain wavelength limits. Krishnamurthy measured the predominant frequencies of cavity-induced flow oscillation by using a hot wire for free-stream Mach numbers of 0.4 to 1.5 and length to depth ratios of 0.95 to 6.7. Krishnamurthy evaluated the measured frequencies by using the following equation at each free stream Mach number,

$$f = C\frac{1}{L} \tag{1}$$

Where f was the oscillation frequency and C is a constant. Oscillation frequencies measured at Mach 1.5 conformed to this equation for L/D = 2. This indicated that the flow oscillation predominantly occurred in the longitudinal direction for this L/D. The data failed to conform to this observation for L/D = 2. He suggested that the transition from longitudinal oscillation to transverse oscillation will occur around the length to depth ratio equaling 2 under supersonic conditions [10]. These results were verified by Chandra and Chakravarthy [11].

In the 1950s, Chapman solved the boundary layer equations for laminar flow over a cavity [12]. Larson used Chapman's mathematical model to design an experiment to perform wind tunnel tests in the supersonic speed range [13].

Plumbee (1962) proposed that the observed discrete tones in cavity flow were likely the result of cavity resonance. He suggested that the frequencies of the tones were identical to those that corresponded to the maximum acoustic response of the cavity. Accordingly, the turbulent shear layer that spanned the open end of his cavity provided a broadband noise source, which drove the cavity oscillation; He suggested that the response of the rectangular cavity to this broadband excitation was instrumental in selecting certain narrow band frequencies for amplification [14].

Following Plumbee, Larson et.al. performed turbulent base flow investigations at Mach 3. However, these theoretical approaches were not sufficient to calculate the separated flow over a cavity for the base of a vehicle. He did note that the flow was extremely sensitive to the effects of the incoming boundary layer [13].

Rossiter (1964) pointed out where this theory has difficulties. Experiments revealed that laminar flow produces louder tones even when the broadband noise, such as that pointed out by Plumbee, was not present. Therefore, Plumbee's theory did not apply when the flow was laminar [6].

In the same time period as Rossiter, Tani, Iuchi, and Komodo conducted low speed measurements on the flow separation associated with a backward facing step [15]. The distribution of pressure along the surface and the distributions of mean and fluctuating velocities across several transverse sections were studied and the pressure distribution was found to be rather insensitive to the changes in step height and thickness of the approaching boundary layer for low subsonic flow and variable step heights. Additionally, a fence was placed after the rearward-facing step and was found to be ineffective until fence height was about 1/2 of the total step height. The lack of sensitivity was attributed to the flow behind the step. They explained that the flow was maintained in equilibrium such that that the pressure exerted by the solid surface was balanced by the shear stress which was set up in the mixing region approximately independently of the step height and the approaching boundary layer.

In the late 1960's J. P. Rhudy and J.D. Magnan investigated turbulent cavity flows at Mach numbers of 4 and 8. For all tests, the initial ratio of boundary layer thickness to cavity depths was 0.2. Crocus linear relation between velocity and total temperature was found to be reliable at Mach 8. Recirculating fluid total temperature was of main interest in this study and averaged 75% of the freestream temperature [16].

Also occurring in the late 1960's, East obtained further evidence to support Plumbee by citing that the depth mode, which is the lowest normal mode, is often excited at very low subsonic Mach numbers [17]. It was later determined that at slightly more moderate Mach

numbers, the discrete tones exhibit characteristics that cannot be explained by this normal mode resonance concept. For Mach numbers above M = 0.15 a sequence of tones was observed. Rossiter observed the Strouhal number plotted versus the Mach number. From such a plot very distinctive bands that demonstrate the frequencies of periodic pressure fluctuations in rectangular cavities can be visualized. From the presentation of data in Figure 9 combined with his shadowgraph observations; Rossiter was one of the first researchers to deduce that the observed phenomenon was a result of acoustic feedback.

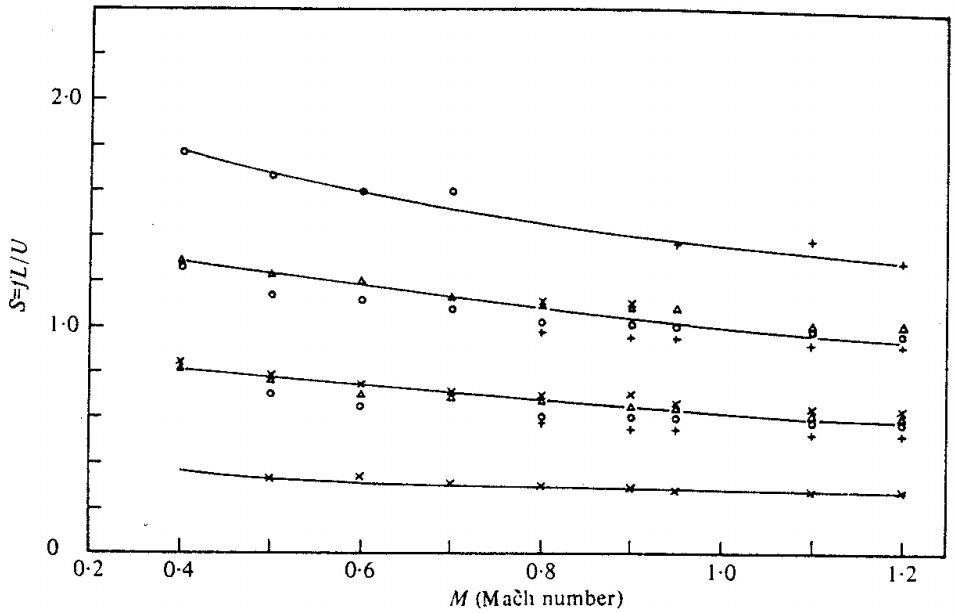

Figure 9: Rossiter's Results for Mach Number vs. Strouhal Number [6]

These early investigations ranged in Mach numbers from 0.4 to 1.2 where Rossiter observed that vortices traveled downstream along the shear layer which spanned the open end of the cavity. Rossiter then prescribed a model that he believed to be responsible for the generation of cavity tones. Vortices were shed periodically from the cavity leading edge and convected downstream in the shear layer until they reach the trailing edge of the cavity. The interaction with the trailing edge generated what he termed as acoustic pulses which propagate back upstream in the cavity towards the leading edge of the cavity. Upon making it back to the leading

edge, the pulses cause the shear layer to separate at the upstream edge and result in the shedding of new vortices. This constitutes a feedback loop mechanism. Using this knowledge a semi-empirical Rossiter formula was derived for the tone frequencies.

$$\frac{f_{tones}L}{U_\infty} = \frac{m - \gamma_{factor}}{M + \frac{1}{k'}} \tag{2}$$

Where f is the frequency of the tones, L is the length of the cavity, U_∞ is the free stream velocity, m is an integer mode number, M is the Mach number, and k is the ratio of convection velocity of vortices to free stream velocity, γ is a factor to account for the lag time between the passage of a vortex and the emission of a sound pulse at the downstream corner of the cavity. The constant k can be expressed mathematically as the following ratio of convective velocity and free-stream velocity:

$$k = \frac{U_c}{U_\infty} \tag{3}$$

Rossiter measured values of the empirical constants k and γ and found them to be 0.57 and 0.25 respectively for the cavity with length to depth ratio of L/D = 4 and this worked well for a variety of cavity geometries up to L/D = 10 [18]. Rossiter's formula was largely inaccurate when the Mach number exceeded the boundaries in Figure 9. Within these boundaries, the time averaged power spectra often exhibit multiple peaks that result from flow coupling described above. These peaks are named after Rossiter and are called the "Rossiter modes" and are accurately predicted by the semi-empirical formula. Rossiter's model was highly dependent on localized vortices. As proved later by Krishnamurthy [10] and Heller and Bliss [18] through Schlieren and water table visualization respectively, vortex shedding was not always present even through the fluid in the cavity and the free shear layer was undergoing violent oscillation

even in supersonic flow. Schlieren observations by Heller [18] supported these findings for high subsonic and supersonic flows and modified Rossiter's equation for supersonic flows. They also concluded that vortex shedding was not the most important factor over the entire Mach number range even though Rossiter's model was based on these localized cavity vortices and provided an explanation for the inaccuracy of the Rossiter empirical formula [18].

In 1970 Heller extended Rossiter's formula to account for the free-stream Mach number and the cavity Mach number. This proved to be applicable for flows in high subsonic, transonic, and supersonic flow regimes. This resulted in what is called the modified Rossiter mode equation and is as follows:

$$St_n = \frac{R_n L}{U_\infty} = \frac{n - \varepsilon}{M_\infty (1 + \frac{\gamma - 1}{2} M_\infty^2)^{-\frac{1}{2}} + \frac{1}{\beta}} \tag{4}$$

where the included gamma is the specific heat ratio of the gas flowing over the cavity [18].

Also, the details of the physical processes producing acoustic feedback are of great importance to noise suppression techniques. Rossiter's model did not describe how the acoustic disturbances were generated as the acoustic feedback excited the shear layer. The driving mechanism of cavity oscillations in the shear layer was not related to the model until Bilanin and Covert [19]. The free shear layer at the leading edge of the cavity are subject to Kelvin-Helmholtz instabilities and occurs when there is a shear force in a fluid or when there is a velocity difference across a shared boundary between two fluids. Bilanin and Covert assumed a periodic agitation at the leading edge of the cavity that excited instability waves of the shear layer. These waves later grew as they propagated downstream and produced a fluctuating shear layer at the trailing edge of the cavity and a half period later, discharged cavity flow into the external flow and completed a system of mass inflow and outflow. The system was assumed to

be causing acoustic radiation. Acoustic disturbances were allowed to propagate upstream where upon impingement with the upstream wall gave rise to a localized pressure force, which further excited the shear layer, thus closing the feedback loop mechanism [19]. Their model had three major assumptions: a thin vortex sheet idealizing the shear layer, a line source at the trailing edge of the cavity that was allowed to pulsate in a periodic motion and a pressure force placed at the upstream lip of the cavity that simulated the acoustically excited shear layer. By employing an infinitesimally thin vortex sheet, they neglect the fact that the flow becomes stable at sufficiently high Mach numbers. If the total temperature of the fluid above and below this infinitesimally thin vortex sheet is equal, then the flow is stable for $M > 2$. This equates to no driving force for the cavity flow above this Mach number, which is in direct contradiction to experimental observations. For example, in Rossiter's experiment in 1964, the boundary layer thickness was approximately 0.65 inches at the subsonic speeds tested. The phase of the Bilanin and Covert model must increase by a multiple of 2π per cavity cycle. The model was free of any empirical constant and agreed reasonably well with high supersonic Mach number flows. Their measurements and experimental data did not agree as well for low supersonic and high subsonic Mach numbers, however, it was seen as an improvement over Rossiter's formula. The issue of how acoustic disturbances interacted with the leading edge and further excited flow instabilities was not addressed [19].

The aerodynamic noise and acoustic tones are a by-product generated from flow instabilities. Cavity noise was studied in 1973 by Block and also numerically studied by Hardin and Pope. They discussed the tonal characteristics of cavity flow via a radiating sound field for certain flow regimes [19, 20].

Sarohia (1975) appears to have been the first to measure the spreading rate in the shear layer in detail. Although the shear layer is sensitive to all flow conditions, he noted that the spreading was approximately linear and that the spreading rate increased as the ratio of cavity length to boundary layer momentum thickness increased when Reynolds number was held constant. He noted that the spreading rates were significantly lower than for free shear layers. His boundary layers were exclusively laminar [21]. Gharib and Roshko also found linear growth of the shear layer and determined that the spread rate was approximately constant [22]. They also noted that the thickness of the incoming boundary layer was important and they recognized it as a determinant factor for the mode selection, specifically the ratio of cavity length over the momentum thickness of the separating boundary layer. They also were the first to note that there exists a minimum length below which the shear layer cannot roll up [22].

Heller and Bliss observed the temporal variation in the flow fields by using water table visualization. By conducting wind tunnel experiments using cavities with length to depth ratios from 4 to 7 over a Mach number from 0.8 to 3 he was the first to note stronger peaks when the boundary layer was laminar and suggested that a compression wave was generated when the shear layer was deflected downward. They also noted that pressure fluctuations were highest near the trailing edge of the floor falling off inversely with distance towards the leading edge [18]. Various simulations including Nishioka [23] concluded that the compression wave was generated when the shear layer reached its highest position. However later on, in 2012, Handa concluded that the generation of the compression wave was independent of the shear layer oscillation frequency [24].

Block (1976) included the effect of length to depth ratio but did not address the inadequacies of Bilanin, Covert, and Rossiter, mainly the shear layer excitation in the feedback mechanism [25].

In the late 1970s Rockwell and Naudascher described the shallow cavity (L/D < 1) and deep cavity flows (L/D > 1) and determined that flow oscillation occurred predominantly in a transverse direction for deep cavities and in a longitudinal direction for shallow cavities [26].

Tam and Block introduced what is known as the pressure-wave generation mechanism in constructing an oscillation model. They argued that the trailing edge of the cavity is shielded from external flow by the shear layer during the upward motion. When it is shielded then the external fluid flows smoothly over the trailing edge and no compression waves are generated. In addition, when the shear layer is deflected downward, the external fluid flows into the cavity and a high-pressure region. Subsequently a compression shock is emitted near the trailing edge [25]. Successive visualization results by Handa using high-speed cameras to capture the flow features contradicted observation of Tam and Block [25].

In 2012, Handa studied the mechanism behind cavity-induced pressure oscillations in supersonic flows past a deep rectangular cavity. Since pressure oscillations were not well understood, the pressure waves around a deep rectangular cavity over which nitrogen flows at a Mach number = 1.7 and a free stream Reynolds number based on the duct height of 1.48 $X10^5$ were visualized using the Schlieren method and captured using a high speed camera. The high-speed camera was necessary in order to ensure that the Schlieren images showed the flow periodicity [24]. The images showed the shear layer periodically changed its height. Compression waves were visualized that traveled upstream in the cavity. Handa also concluded that the relationship between the shear layer motion and the generation of the compression wave

at the trailing edge is independent of the dominant oscillation frequency [24]. Handa observed many compression waves propagating inside the cavity, all originating from the trailing edge of the cavity. The previous model proposed by Tam and Block was proven incorrect by Handa's visualization, which shows a reflection did not occur near the bottom wall of the cavity. Waves were also observed that seemed to excite the shear layer at the leading edge and play an important role in the feedback mechanism of the self-sustained oscillation. Compression waves were generated at the maximum shear layer height but the visualization contradicted previous work again by showing that the compression wave had already started to propagate at a time when the shear layer still shielded the trailing edge from all external flow [24].

Chandra and Chakravarthy verified Krishnamurthy's evaluation that the transition from predominantly longitudinal oscillation to traverse oscillation under supersonic conditions by setting the Mach number = 1.5 and then varying the L/D from 1.5 to 2.0. Together they verified these results and discovered that the Strouhal numbers calculated based on the cavity length are approximately constant for L/D > 1.5 to 2.0. They captured instantaneous Schlieren images of flows for varying length to depth ratios of the cavity from 0.57 to 2.67. The Schlieren images were locked with respect to the phase of the pressure oscillation. They observed that compression waves were generated at the trailing edge and then propagated upstream inside the cavity [27].

Zhang and Rona [28] conducted supersonic experiments over a shallow cavity at Mach = 1.5 by using both model tests and computational fluid dynamics. While studying, they identified five types of shock/pressure waves around the cavity. Downstream convecting pressure waves associated with large vortices in the driving shear layer were observed [28]. More importantly, they identified two directions of coupled motion, one motion of flapping in the transverse

direction due to the shear layer instability and one vortex convection motion in the streamwise direction due to the non-linear propagation effects leading to wave "steepening" with convection.

1.3 Cavity Flow Control

There are two types of flow control approaches used and consist of passive flow control and active flow control and are described below.

1.3.1 Passive Flow Control

Passive control devices such as spoilers have been attempted in order to attenuate the cavity tones. However, these devices protruding from the cavity cause an increase in drag and don't always perform well at off design conditions.

Heller and Bliss suggested using a slanted trailing edge and introducing vorticity into the shear layer to eliminate cavity resonance [18]. Smith used multi steps and pins extending into the supersonic approach flow to attenuate cavity tones [29].

Zhang and Rona attempted the attenuation of cavity flow oscillation through leading edge flow control [30]. They tried passive flow control via compression ramps and expansion surfaces via solving the short time Reynolds averaged Navier-Stokes equations with turbulence modeled by a k-ω model. Compression ramps were used at supersonic speeds of 1.5 and 2.5 and reported that a strong flapping motion leads to small changes in the frequency and sound pressure level in the cavity compared with baseline cavity. Roll up of the shear layer produced convective vortices, leading to enhanced fluctuations on the downstream surface [30]. An increase in drag was observed because of the high pressure on the compression ramp. Mean pressure drag also increased for the expansion surface, even though the flow physics remained the same as that of the baseline case.

Ukeiley studied both rods and variable height fences and concluded that rods placed in the upstream boundary layer produce a mean wake that in effect modified shear layer development at Mach number 0.6. He concluded that the mean gradient of the shear layer was critical in determining attenuation properties and that the rod also "lifted" the shear layer [31].

Spoilers and fences are commonly installed on aircraft at the production level to specifically reduce the acoustic tones. Fences increase the shear layer which shifts the most unstable shear layer frequencies to lower values [32]. Spoilers and ramps deflect the mean separation streamline higher into the flow so that reattachment occurs downstream of the cavity edge, weakening the feedback acoustic wave and the resulting strength of the Rossiter mode.

1.3.2 Active Flow Control

The advantage of active flow control is that these techniques can suppress resonance over a range of operating conditions and various cavity geometries. Many of these techniques work well for subsonic conditions, their main strategy being to disrupt the Rossiter feedback mechanism. Cattafesta compared suppression by closed-loop flow control to the open loop case and demonstrated that the closed-loop approach used an order of magnitude less power [32]. The active control with open loop forcing of the shear layer is at a non-resonant frequency. Although many significant results have been obtained by using the open loop flow control, the technique of applying a forcing frequency lacks the responsiveness and flexibility to be used in the dynamic flight environment. Methods include lifting the shear layer to change the downstream reattachment point [33, 34], modification of the mean shear profile combined with lifting [33], thickening the shear layer[33], and low frequency excitation of the shear layer at off resonance conditions [32, 34, 35, 36, 37, 38]. Other novel ways include a high frequency, termed hifex

excitation [39, 38], an accelerated energy cascade in inertial range starving the lower frequency modes [39], mean flow alteration changing the stability characteristics [40]. Some attempts have been made to cancel the feedback acoustic wave itself via active flow modification [32].

McGrath and Shaw attempted active control using a low frequency leading edge oscillator and a high frequency tone generator to suppress cavity resonance [41]. Shaw discussed using pulsed jets to eliminate cavity tones [42]. Lamp and Chokani compared the effect of steady and oscillatory blowing and illustrated the advantage of pulsed excitation [43]. Raman et. al. [44] discussed cavity resonance suppression using miniature fluidic oscillators. These experiments were conducted in a supersonic jet facility at the NASA Glenn Research Center.

Hemon and Wojciechowski achieved attenuation of cavity internal pressure oscillations by a shear layer in a subsonic cavity with velocities less than 30 meters per second by shear layer forcing with pulsed micro-jets. They found for their deep cavity that forcing was effective when the forcing frequency was larger than the cavity resonance frequency and that it was ineffective when lower than the resonance frequency [45]. When the forcing frequency coincided with the cavity resonance frequency, the pressure level was strongly amplified.

Williams et. al. [46] attempted open loop supersonic open cavity flow forcing at a Mach number of 1.86 in a cavity very similar to the one designed here. A pulsed blowing type actuator was used to provide controlled inputs of mean and oscillating flow at the upstream edge of the cavity. Nonlinear interactions between the forcing and the naturally occurring Rossiter modes were not observed in their experiment. Amplification of the input disturbances occurred when the forcing frequency was between the Rossiter modes. In the regions where they observed amplifications, the cavity response amplitude was proportional to the input disturbance amplitude, which they suggested means that the overall system behaves linearly. The Rossiter

modes were not in a nonlinear saturated state because they suggested that their amplitude could be increased by up to 20 dB with just small amplitude inputs of external forcing [50].

Bueno used an array of six miniature jets with a fast response of 3 ms just upstream of the leading edge to study orthogonal injection on Mach 2 flow on cavities of length to depth ratios from five to nine. Instantaneous and ensemble-averaged pressure time histories and cross correlations were recorded. Experiments conducted included both short and long cyclical pulses at fifty percent duty cycle. Bueno concluded that continuous mass injection is more effective for acoustic noise suppression than pulsed blowing [34].

Different injection gases were utilized by Ukeiley in an array of eight powered "whistles" mounted in the forward cavity fall. Injection gases chosen were heated air, nitrogen and helium. Whistles were capable of producing high frequency tones on a superimposed on a steady jet. When studied with and without the high frequency component the best results were obtained with steady helium blowing. More importantly Ukeiley noted in conclusions that isolated high frequency forcing effects needs to be more rigorously studied [33].

Effect of a sonic jet array, pictured in Figure 10, mounted upstream of a Mach 2 cavity edge was studied by Zhuang. Using 400 μm diameter jets he observed that an oblique shock was formed that deflected the shear layer thereby altering its trajectory and subsequent impingement point. As seen in his pressure spectra of Mach 2 flow with forcing in Figure 11, Zhuang noted decrease in the broadband and tonal acoustics by 8 dB but increasing the blowing coefficient showed no significant improvement over implementation of sonic jets [47].

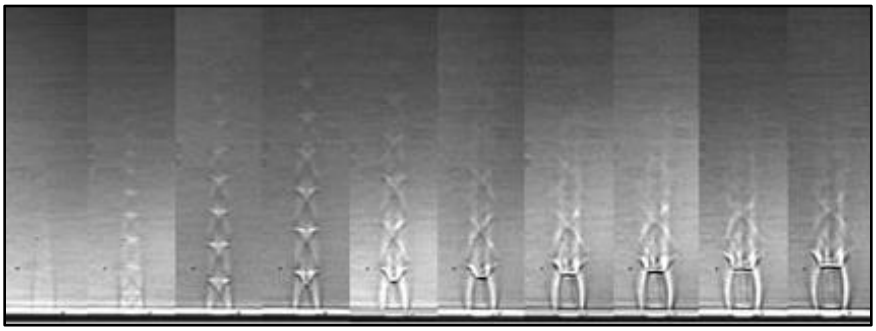

Figure 10: Zhuang Sonic Jet Actuators

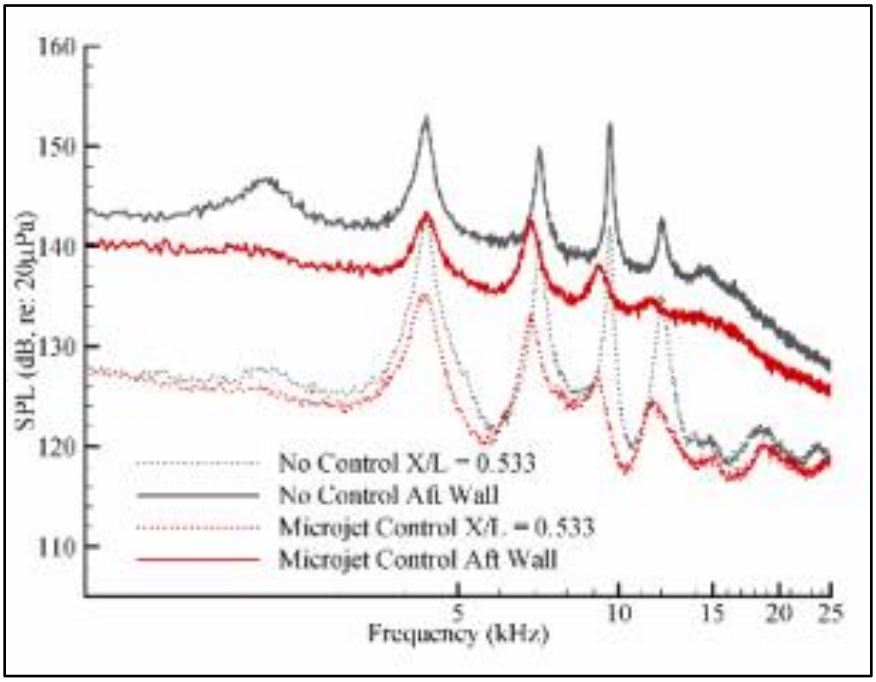

Figure 11: Zhuang SPL Distribution Showing Sonic Jet Effectiveness

It must be noted that a number of these methods incorporate mass injection at the leading edge. These methods basically cause a positive pressure response at the leading edge and operate by producing vorticity locally and thereby production of local vortex shedding as well.

1.4 Objectives of Current Research

As noted previously cavity acoustics remains a very challenging area of research that requires parametric study of a variety of flow control strategies. The primary objective of the present work was to design and construct a Mach 2 tunnel dedicated to cavity acoustics research with the flexibility of utilizing a number of active and passive flow control methodology and with optical access from the throat to the end of the cavity for optical diagnostics and precise instrumentation. A method of characteristics was used to design a 2d nozzle and cavity that had geometric scales similar to the cavity being tested in the Trisonic Gasdynamics Facility at Wright Patterson Air Force Base.

1.5 Introduction to Supersonic Wind Tunnels

Wind Tunnels are instrumental tools for studying cavity flow and a general understanding of their design and operation principles is included as a foundation for this research. For a varying area flow system the area ratio can be defined as:

$$\frac{A_2}{A_1} = \frac{\rho_1 V_1}{\rho_2 V_2} \tag{5}$$

The variable a is defined as the speed of sound and is defined as

$$a = \sqrt{\gamma RT} \tag{6}$$

Where R is defined as the universal gas constant. Mach number is denoted by M and is defined as

$$M = \frac{V}{a} \tag{7}$$

where V is the velocity and a is the speed of sound. For a variable area flow system the temperature ratio is defined as:

$$\frac{T_2}{T_1} = \frac{1 + [\frac{\gamma - 1}{2}]M_1^2}{1 + [\frac{\gamma - 1}{2}]M_2^2} \tag{8}$$

For a perfect gas, the general relationship between static and stagnation pressures is defined as the following:

$$p_t = p(1 + \frac{\gamma - 1}{2} M^2)^{\frac{\gamma}{\gamma - 1}} \tag{9}$$

Therefore, for a variable area flow system the ratio of total pressures is defined as

$$\frac{p_{t2}}{p_{t1}} = \frac{p_2}{p_1}\left(\frac{1+\left[\frac{\gamma-1}{2}\right]M_2^2}{1+\left[\frac{\gamma-1}{2}\right]M_1^2}\right)^{\frac{\gamma}{\gamma-1}} \tag{10}$$

And the variable area ratio is

$$\frac{A_2}{A_1} = \frac{M_1}{M_2}\left(\frac{1+\left[\frac{\gamma-1}{2}\right]M_2^2}{1+\left[\frac{\gamma-1}{2}\right]M_1^2}\right)^{\frac{(\gamma+1)}{2(\gamma-1)}} \tag{11}$$

It is from this state that the sonic reference state involving the throat for a supersonic flow is formulated and involves setting the Mach number to 1 and solving for the exit Mach number. The resulting equation with reference to the sonic condition at the throat is defined as the following:

$$A_{ratio} = \left(\frac{1}{M}\right)\left[\frac{2}{\gamma+1}\left[1+\frac{(\gamma+1)*M^2}{2}\right]\right]^{\frac{(\gamma+1)}{2(\gamma-1)}} \tag{12}$$

Nozzle operation follows these relationships. For the sake of this discussion two types of nozzles are possible, namely converging-only and converging-diverging. A nozzle is considered "choked" if the nozzle outlet pressure remains at the critical pressure causing the throat to have a sonic (M = 1) condition. Any further reduction of the back pressure, the pressure on the receiver side of the flow, will have no effect on the flow conditions inside the nozzle.

For a converging diverging nozzle, the throat is the section of minimal area. The area ratio is the main distinguishing characteristic with the objective of this type of nozzle being supersonic flow. If the nozzle is operating at the so-called "design operating condition" the nozzle flow is subsonic to the throat, sonic at the throat, and supersonic thereafter. Employing the isentropic relations with a design exit area and Mach number will allow the pursuit of other

variables such as pressures at the throat and chamber needed to drive the flow. If the device is operating well below the design condition it will simply act as a venture tube whereby the converging portion will act as a nozzle and the diverging part a diffuser. It is important to note that after the pressure that drives sonic flow at the throat has been reached; further lowering of the receiving pressure does not change the flow rate.

Geometry alone can set the maximum available Mach number. However, flow conditions inside a converging-diverging nozzle are determined by the operating pressure ratio, the ratio of the receiver pressure to the inlet stagnation pressure. Nozzle pressure ratios are distinguished by three critical points. The first critical point is usually given by the pressure ratio that results in flow that is subsonic in both the converging and diverging sections but sonic at the throat. For any pressure ratio above this critical point, the nozzle is not choked and will be subsonic throughout. The third critical point is usually defined as the pressure ratio that will yield the design operating condition where the flow is subsonic in the convergent portion, sonic at the throat, and then supersonic throughout the divergent portion. These are the only two points where there is isentropic flow throughout a sonic throat and the exit pressure equal to the receiver pressure. Subsonic flow at the exit means that the receiver pressure equals the exit pressure.

If the pressure ratio is lowered below the first critical point, a normal shock will form in the area downstream of the throat, and the remainder of the nozzle will act as a diffuser according to the rules where area is increasing and the flow being subsonic. The operating pressure ratio determines the location and the strength of the shock. The shock acts in a way such that the combination of the pressures ahead of the shock, across the shock, and downstream of the shock produce a pressure that exactly matches the outlet pressure. The second critical point is

the pressure ratio that creates a shock located at the exit plane. However, these are considered ideal points and in reality we have boundary layer effects, reflected shocks, and lambda shocks. Between the second and third critical points are all of the pressure ratios that cause compressions outside of the nozzle called over-expansions because the compression will be outside the nozzle. If the receiver pressure itself is below the third critical point an expansion will take place outside the nozzle meaning that an under expansion will take place.

Converging-Diverging nozzles are required to operate a supersonic wind tunnel. Adding a diffuser makes the tunnel operate more economically. This means that a user must operate the tunnel at a pressure ratio above the second critical point. Furthermore, for supersonic tunnel design, special care must be placed on design of the nozzle and is discussed in detail in Chapter 2. Any discontinuities can cause unwanted shocks and contribute to the "uncleanliness" of the fluid at the testing position. Figure 12 is a basic schematic detailing supersonic wind tunnel converging diverging nozzles.

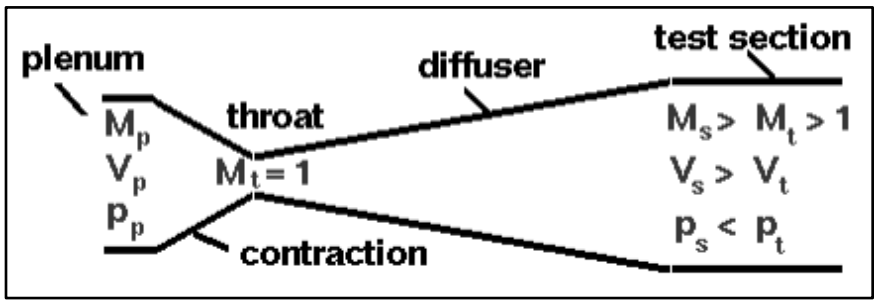

Figure 12: Supersonic Wind Tunnel [48]

Present in supersonic flow is a converging diverging nozzle compared to the subsonic flow where only the converging portion is present. Air density for supersonic flows is not constant. Compressibility effects are ever present; the increasing area causes a direct decrease in velocity and an increase in pressure until it reaches the throat. At the throat the flow is termed

"choked" and the local Mach number is equal to 1. Following the throat, the high level of pressure is exchanged for velocity as the area increases until desired test section area is achieved. The most critical stage of design is the nozzle contour designed by using the Method of Characteristics. A typical blow-down configuration, chosen for this research is visualized in Figure 13.

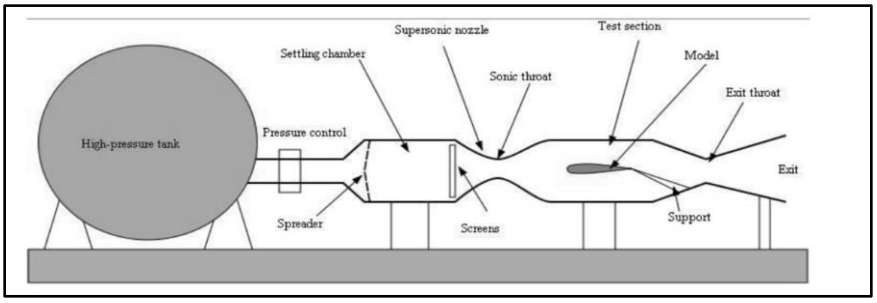

Figure 13: Typical Blow-down Wind Tunnel [2]

Wind tunnels are actively designed to mimic the Reynolds and Mach number of real world flow via dynamic similarity. Reynolds number, a dimensionless parameter, is a ratio of inertial forces to viscous forces and is defined as the following:

$$Re = \frac{\rho V l}{\mu} \tag{13}$$

Where ρ is the density, V velocity, l is a characteristic length, and μ the dynamic viscosity. Using these two methods to provide dynamic similarity, wind tunnels provide a test environment. Dynamic similarity is critical for the test environment as to accurately characterize the flow regimes, i.e. laminar flow where viscous forces dominate or turbulent flow where inertial forces dominate.

While the Mach number is fixed by the geometry, the Reynolds number is varied by controlling the delivery pressure. The density term in the formula for Reynolds number in

combination with the equation of state can easily show how the Reynolds number is dependent on pressure. By substituting in the equation of state seen below, the Reynolds number formula becomes the following:

$$p = \rho RT \tag{14}$$

$$Re = \frac{\frac{p}{RT} Vl}{\mu} \tag{15}$$

where , R is the universal gas constant, and T is the local temperature. The delivery pressure is controlled by a manual control determining how much the stagnation pressure is allowed to rise. The delivery pressure range for the wind tunnel designed at Auburn University while still achieving Mach 2 is approximately 40 psi to 70 psi where the 70 psi is the upper limitation of the pressurizing system and not the tunnel itself.

Chapter 2

WIND TUNNEL DESIGN AND SELECTION OF COMPONENTS

2.1 Tunnel Components

All Tunnel components were custom designed in SolidWorks and machined at Auburn according to the tunnel requirements for open cavity flow, modularization, and test section size. A nozzle was designed by a method of characteristics and verification procedures were undertaken along with the designing of the test section and diffuser. Aside from the design of the tunnel itself, instruments were chosen for analysis and existing air supply components were incorporated.

2.1.1 Nozzle

A nozzle is a device that converts enthalpy, or pressure energy for the case of an incompressible flow, into kinetic energy. An increase in velocity is accompanied by an increase or decrease in area depending on whether or not the flow is subsonic or supersonic. For subsonic flow area, if velocity is to increase, the area must decrease. For supersonic flow as velocity increases, the area increases to a desirable area ratio defined by the previous equation.

A Method of Characteristics solution was developed for design Mach = 2 and compared to a method of Characteristics solution supplied by open source from Virginia Tech for educational use. The code developed at Auburn University is listed in the Appendix 2 of this document. Both codes generated relatively close solutions but the open source code was chosen because the flow field was “cleaner”, indicated by the larger region of Mach 2 flow at the exit plane. The results were verified using a MATLAB Euler code as well as a hybrid Euler code

developed at Auburn University and the results are displayed below using TECPLOT in Figure 14.

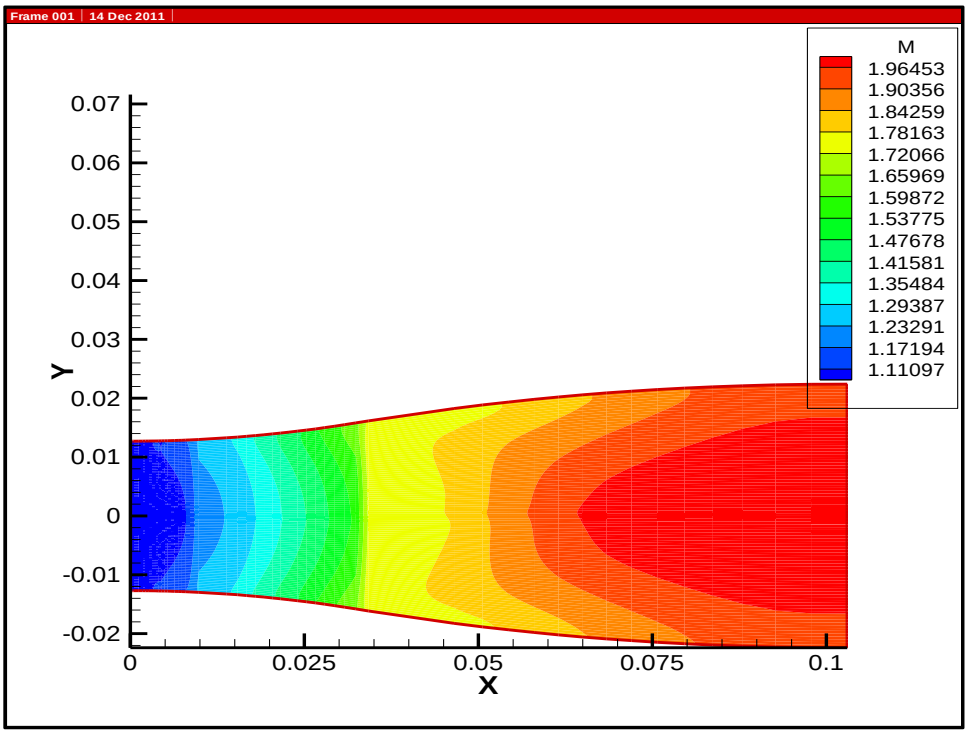

Figure 14: Hybrid Euler Code Simulation Output for a Mach 2 Wind Tunnel Nozzle

A method of characteristics is a very elaborate procedure for the creation of an accurate set of data points to create a nozzle, be it for a sharp expansion nozzle or a wind tunnel nozzle with a radius placed at the throat for more uniform flow at the exit plane. A supersonic wind tunnel uses this method to create an expansion nozzle similar to those found on axisymmetric rocket engines to expand air to supersonic speeds at the test section. The flow accelerates through a converging duct (M <1) and arrives at the throat (A_{min}) beyond which the geometry for smooth expansion is derived from the Method of Characteristics.

2.1.1.1 Finite Expansion Circle Method of Characteristics

To utilize the method of characteristics with an expansion circle, an initial assumption is used of M = 1 at the throat. This is commonly referred to as the sonic line. Since the flow has to be accelerated to an exit Mach number,M_{exit}, the total corner angle is the Prandtl-Meyer Function evaluated at this value of Mach number divided by two. The Prandtl-Meyer function is given by the following equation:

$$\nu(M) = \sqrt{\frac{\gamma+1}{\gamma-1}}tan^{-1}\left(\sqrt{\frac{\gamma+1}{\gamma-1}(M^2-1)}\right) - tan^{-1}\sqrt{(M^2-1} \tag{16}$$

The variable $\nu(M)$ is the Prandtl-Meyer angle corresponding to the design Mach number. The maximum wall angle is found following this initial calculation by dividing the total expansion angle by 2. This is intuitive as the nozzle has an expansion and a straightening section over the course of the total length of the nozzle.

$$\theta_{total\ corner\ angle} = \upsilon(M)/2 \tag{17}$$

Once the corner angle is obtained, the expansion fan can be replaced by a number of characteristics lines originating from finite expansion points such that the flow turns by the total corner angle with the angle in between the characteristics given as follows:

$$\theta_{characteristics} = \theta_{total\ corner\ angle}/n_c \tag{18}$$

where n_c is the number of characteristics. For each of these right running characteristic lines the value of $\nu(M)$ is equal to their value.

For a wind tunnel nozzle the method of characteristics must implement an initial finite expansion through what is termed the "expansion circle". The total expansion angle is given by

evaluating the Prandtl-Meyer function at the design Mach number. The variable θ_{max} is given by one half of the total expansion angle, and this θ_{max} is divided into "s" number of increments where s is the desired number of characteristics, as seen in Figure 15 . Following this determination of the spacing in-between expansions, the x and y position of the center of the expansion circle is selected. The left running characteristics of the finite expansion, termed K^-, are equal to their individual angles of expansion multiplied by 2 and the right running characteristics, termed K^+, are simply equal to zero. An example of such an expansion is given in Figure 15 whereby the design Mach number was 2 and for γ=1.4.

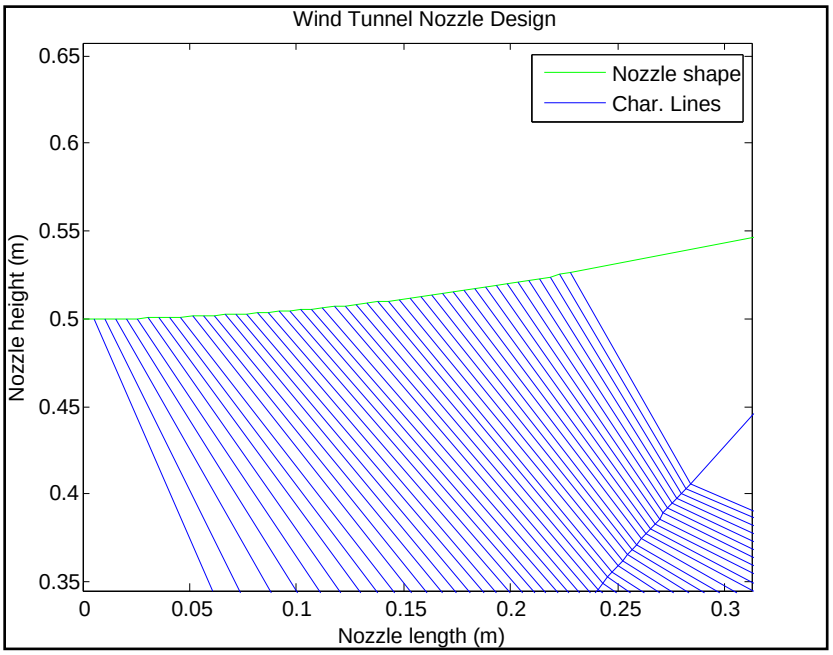

Figure 15: Smooth Throat Radius of Curvature in Method of Characteristics (M=2)

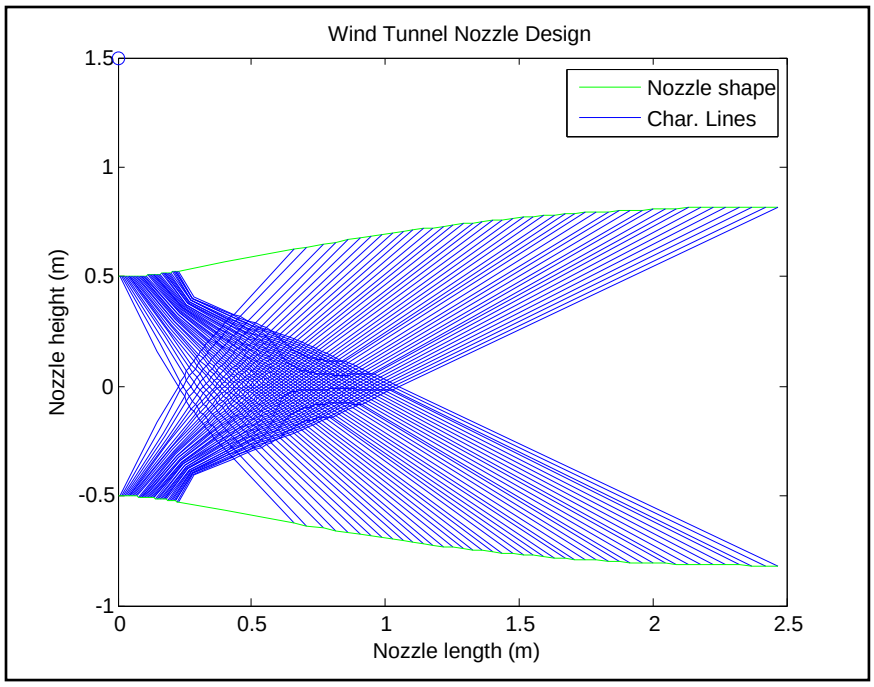

Figure 16: MoC Wind Tunnel Nozzles

K^+ and K^- are the right and left running characteristics running along the interior of the nozzle. These values can be found by using the following

$$K_- = \theta + \upsilon \tag{19}$$

$$K_+ = \theta - \upsilon \tag{20}$$

Two more useful relationships show how these characteristics relate to ν, and θ.

$$\theta = \frac{1}{2}(K_- + K_+) \tag{21}$$

The slopes of the characteristic lines can be found by using the following where mu (μ) is the Mach angle:

$$\frac{dy}{dx} = \theta \pm \mu \tag{22}$$

The nozzle grid is defined by calculating the slopes of the characteristic lines and then finding their points of intersection and defining θ, μ, v, and M at these locations.

2.1.1.2 Prandtl-Meyer Function (Iterative Technique)

The Prandtl-Meyer function is accomplished, when not directly applied, using a simple Newton Raphson iterative technique. The Prandtl-Meyer equation must be solved whenever Mach number is not explicitly known using an iterative technique because of the M^2 terms. Resolution is set to 0.1 in order to determine acceptable numbers. The function works as follows:

$$x_1 = x_0 - \frac{f(x_0)}{f'(x_0)} \tag{23}$$

The process is repeated as

$$x_{n+1} = x_n - \frac{f(x_n)}{f'(x_n)} \tag{24}$$

until a sufficiently accurate value is reached as determined by the resolution of the function. Geometrically the method is described by guessing an initial root close to the true root. An approximation of the function by gathering a tangent line follows this guess. Then the x-intercept of this tangent line is calculated as a better approximation to the functions real root than the original guess and the procedure is iterated. The slope of the tangent line is given by

$$f'(x_{n)} = \frac{dy}{dx} = \frac{f(x_n) - 0}{x_n - x_{n+1}} \tag{25}$$

Also, it may be noted that in the absence of an initial guess when performing the Newton Raphson method then the intermediate value theorem from calculus can also be used.

The area Mach number relationship gives the correct ratio for area of the exit divided by the area of the throat for a converging diverging nozzle. The relationship states that this ratio is a function only of Mach number and γ

$$\frac{A}{A^*} = \left(\frac{1}{M}\right)\left[\frac{2}{\gamma+1}\left[1 + \frac{(\gamma+1) * M^2}{2}\right]\right]^{\frac{(\gamma+1)}{2(\gamma-1)}} \tag{26}$$

For M =2, A/A^* = 1.688.

2.1.1.3 Hybrid Euler Code

A hybrid Euler code, Euler_V3_Nozzles, developed by Vivek Ahuja at Auburn University was utilized to calculate the flow field. As a prerequisite to running the code a grid must be established that spans the entire nozzle and is relatively easily spaced. Due to the nature of the method of characteristics, the lattice that is set up by Euler_V3_Nozzles, the hybrid Euler code specified must be made using a tabular method. For example, a 30 characteristic nozzle would closely space thirty vertical gridlines in roughly the first quarter of the nozzle. The following quarter would probably have very few if any grid lines associated with it, meaning that the entire grid for that quarter would be made up of two grid lines. The remaining 30 characteristics would be in the second half of the nozzle where the straightening section would take place. This causes some rather odd results when plotting the output from the hybrid Euler code. In order to maintain a good solution, accurate precautions must be undertaken to ensure

that grid refinement doesn't become an issue. Depending on the number of characteristics the solution could converge in few minutes. An inviscid approximation is initially done by Euler's Equations given by:

$$\frac{\partial \rho}{\delta t} + \nabla \cdot (\rho \boldsymbol{u}) = 0 \tag{27}$$

$$\frac{\partial \rho u}{\delta t} + \nabla \cdot \left(u \otimes (\rho \boldsymbol{u})\right) + \nabla \mathrm{p} = 0 \tag{28}$$

$$\frac{\partial E}{\delta t} + \nabla \cdot \left(u(E + p)\right) = 0 \tag{29}$$

Where ρ is the fluid mass density and u is the fluid velocity vector with components u and v and $\otimes$ denotes a tensor product.

An evenly spaced grid through the nozzle did not yield the best solution. Increased fidelity at the throat was accomplished by dividing the curvature of the nozzle into primary, secondary and tertiary curves and increasing the number of points used in the program in the primary smooth throat curve in excel. The curves and lattice data for the Euler code are referenced in the appendix of this document.

2.1.2 Diffuser

A diffuser is a device that is used to convert kinetic energy into enthalpy, pressure energy for an incompressible flow. For subsonic operation diffuser area increases and for supersonic flow, diffuser area decreases.

Initially after the second throat the flow was allowed to diffuse in a straight duct. A normal shock-generating block was placed in downstream locations variable to determine the

best placement. This was, in effect, making a second throat and therefore a diffuser. Efficiency was increased after the block was subsequently moved closer to the exit of the test section to one and a half cavity lengths past the test section cavity. The distance between the two peaks was increased until the proper non-choked flow in the second throat was achieved. This design is illustrated in Figure 17.

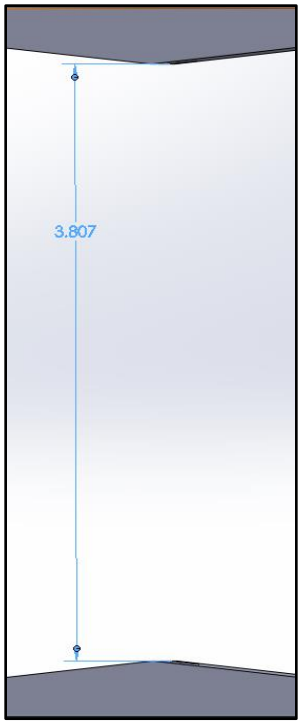

Figure 17: Second Throat Spacing

Ideally speaking, the area at this diffuser was calculated in the following manner. Although this calculation gives a reasonable area for the second throat, a diffuser throat area should always be bigger than the following calculated in order to account for the non-ideal flow, which is actually occurring at the diffuser throat location. This process is detailed here and a MATLAB solution is attached in the Appendix to calculate this area. A reasonable stagnation pressure is chosen to add detail to the calculations and to give an example of how to obtain mass flow rate at the desired condition.

A few values must be specified to begin the calculation. The stagnation pressure for this example is equal to 50 psi. International units are used because MATLAB functions to be called require metric input. For supersonic flow it is a reasonable assumption to assume chocked flow at the first throat in the nozzle and therefore Mach number at that location is equal to unity. Given a value of Mach number and by inputting the ratio of specific heats the inbuilt function titled **flowisentropic** yields values of temperature ratio, pressure ratio and area ratio at the point where Mach number is equal to unity, i.e. the sonic throat, where the ratio is defined as the local divided by the stagnation condition. Pressure at the throat is found by multiplying this ratio by the stagnation pressure.

Furthermore steady operation of the wind tunnel is assumed. Steady operation follows the schematic shown in Figure 18 where a normal shock wave is assumed to be positioned at the second throat.

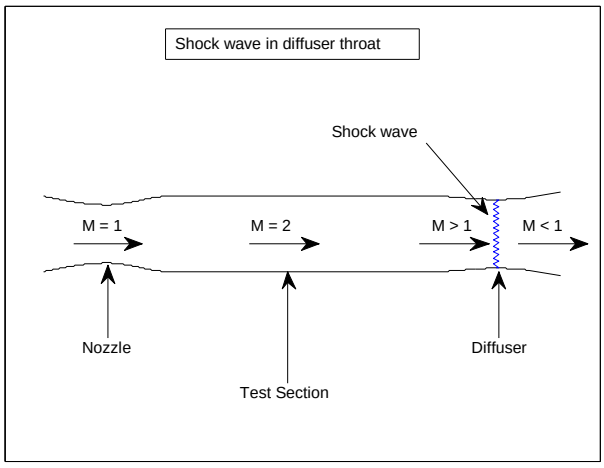

Figure 18: Shock Wave in Second Throat for Steady State Operation

As can be visualized in the figure above, steady conditions imply that Mach number equal to unity at the nozzle throat, test section Mach number equal to Mach number of two and a shock wave positioned at the second throat. On the upstream side of the shock wave the flow is still supersonic, and on the downstream side of the shock wave the flow is subsonic. The process continues as follows,

The nozzle exit plane conditions must be defined. Without making any considerations to the geometry of the nozzle other than the area ratio of the exit to the throat, we define the exit plane conditions. Here we define the test section Mach number equal to two and define the lengths and widths to establish the exit plane area. By defining the altitude at the wind tunnel location the test section temperature speed of sound, pressure, and density can be defined. Altitude is given by calling the standard atmosphere from within MATLAB by using the built-in **atmosisa** function where the function variable is the altitude of Auburn in meters.

Similarly to what was accomplished at the nozzle throat the isentropic temperature, nozzle exit pressure, and area ratios are computed by using the isentropic flow relationships and supersonic equation for area ratio.

By assuming a perfect gas with constant specific heats, we can calculate the factor by which the diffuser area must be smaller than the nozzle area. This calculation is from a simplified form of the conservation of mass equation involving the total pressures and the cross-sectional area. The total pressure ratio, or stagnation pressure ratio, for the diffuser section can be calculated by using normal shock relations at the test section Mach number. Then the area ratio at the shock is given from the conservation of mass by setting the stagnation pressure ratio of the diffuser equal to the area ratio at the shock in the diffuser. Then the diffuser area is simply

calculated by dividing the test section area by the quantity of the area ratio at the shock times the isentropic area ratio.

Because the diffuser throat area is smaller than the test section area, the Mach number of the flow must “converge” towards unity. This time isentropic relationships ascertain the Mach number just upstream of the shock by using the isentropic relations for the reciprocal of the area ratio at the shock:

Normal shock relations can be used to gather the stagnation pressure before the normal shock. Subsequently, mass flow rate can be found, independently of stagnation pressure, by using multiplying the test section density by the test section area, test section Mach number, and test section speed of sound.

The areas and numbers calculated by the procedure discussed here were used as a starting point. A series of diffuser blocks of decreasing height were made and placed in machined slots ahead of a 5 degree sloping ramp.

2.1.3 Test Section

The test area was very carefully considered before construction. Extra care was taken to maximize the testing space. As a preliminary design requirement, optical access from all four sides of the test section was required including the open cavity. A Mach 2 nozzle with an exit plane of 3.5 inches by 4 inches was to mate to the test section as seen in Figure 19. The nozzle exit plane height of 4 inches was maintained for 6 inches in the stream-wise direction to allow the boundary layer to develop after which the test section began. The test section increased the overall height by 1.5 inches to accommodate the cavity depth of 1.5 inches. The internal cavity length was chosen to be 8.5 inches yielding the same length to depth ratio as the AFRL cavity (L/D = 5.67), well within the limits of open cavity flow. The test section ceiling and cavity base, as well as the side walls spanning from nozzle to test section exit, were designed for 1 inch thickness optics grade acrylic. Sealing grooves for which square sealing material was placed on all side walls. Test section removable blocks of 1.5 inch square cross section, highlighted in the picture above, were designed to be removable in order to easily include flow control devices. Furthermore, the tunnel as a whole was designed for quick removal and disassembly by making the tunnel as modular as possible.

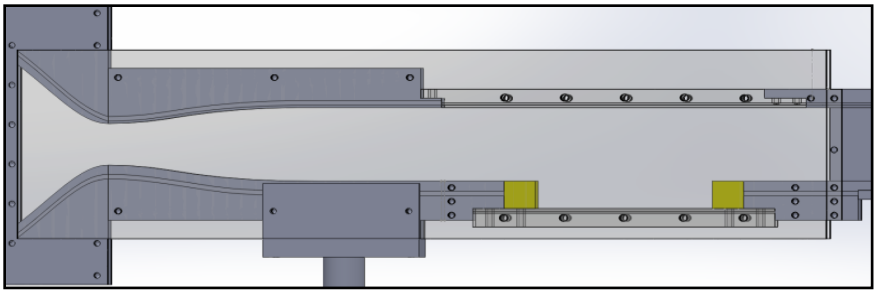

Figure 19: Nozzle and Test Section of Mach 2 Cavity Acoustics Supersonic Wind Tunnel

2.1 Air Supply System

2.1.1 Compression

High pressure air to the tunnel was supplied by an Ingersoll Rand SSR-EP150 150 horsepower compressor. The Ingersoll Rand SSR-EP150 has a rated operating pressure of 125 psig and a max discharge pressure of 128 psig. The Ingersoll and SSR-EP150 is pictured in Figure 20.

Figure 20: Ingersoll Rand SSR-EP150 Compressor

2.1.2 Dryer

Before storage, the compressed air is passed through an Ingersoll Rand HRD45-FHSC compressed air dryer for purpose of removing moisture. The dryer is capable of drying air at a maximum pressure of 150 psig at a max inlet air temperature of 120 F and is pictured in

Figure 21: Ingersoll Rand HRD45-FHSC Compressed Air Dryer

2.1.3 Storage Tanks

Air to the blowdown wind tunnel is supplied by two tanks totaling 625 cubic feet of storage. The two tanks are tied together with an interconnecting t-valve at a storage pressure of 125 psig. The two tanks are pictured in Figure 22.

Figure 22: Compressed Air Storage Tanks

2.1.4 Air Supply Lines and Components

The tunnel was started by a pilot and control valve system supplied by Spence Engineering. The Spence Type E pressure regulating chamber valve, seen in Figure 23, was installed in the line from the storage tanks to the wind tunnel. The valve operates in a unique duty cycle. Upon pressurizing by the compressor, the valve contains a small chamber or passage. The pilot receives the initial pressure through a nipple and union connector and a control line connects the pilot diaphragm chamber to the delivery piping. An electronically actuated type 86 piloting valve was chosen. When a solenoid receives a 5 volt input the pilot valve opens provided that there is pressure behind the pilot. Connecting tubing conducts fluid from the pilot to the main valve diaphragm and a bleedport. When the pilot is open, the fluid flows through the pilot faster than it can escape at the bleedport creating a loading pressure which forces the main

valve open. At this point the delivery pipe and control line are being filled with fluid from the main valve. As the delivery pressure rises it overcomes the force of the pilot throttles allowing the main valve to throttle just enough to maintain the set delivery pressure.

A Spence type 85 solenoid pilot valve was installed to the chamber valve for pressure regulation purposes. According to the manufacturer, the pilot designates a delivery to loading, storage to stagnation, pressure ratio of 1 to 1.8125 meaning that if 125 psi is supplied the maximum delivery pressure would be around 69 psi. Additional details of this combination are given in the Appendix 1 of this document.

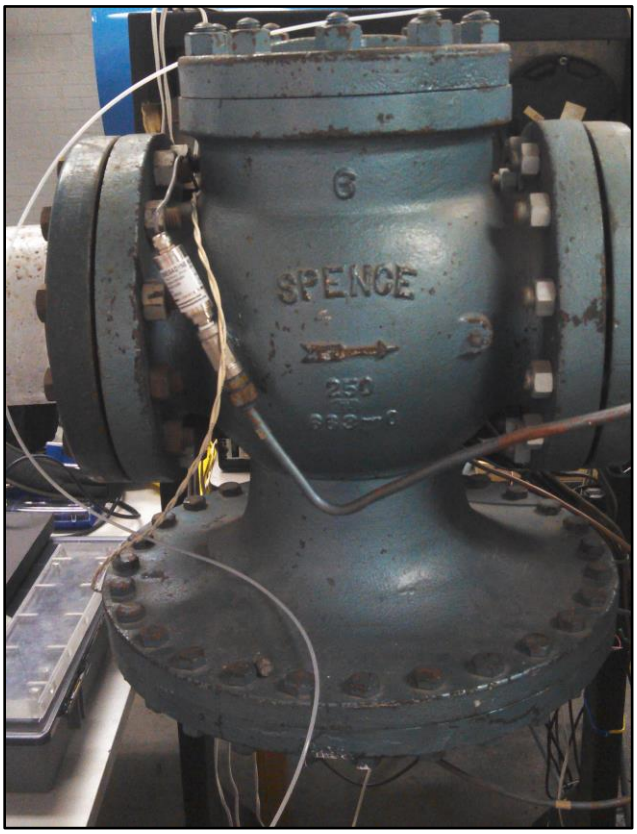

Figure 23: Spence Chamber Throttling Valve

2.2 Tunnel Instrumentation

2.2.1 Pressure Measurement.

The cavity pressures, storage pressures, stagnation pressures were sampled with a National Instrument A/D Converter. A custom designed LabVIEW controller was designed by and integrated to work with the cavity acoustics facility in a manual measurement mode.

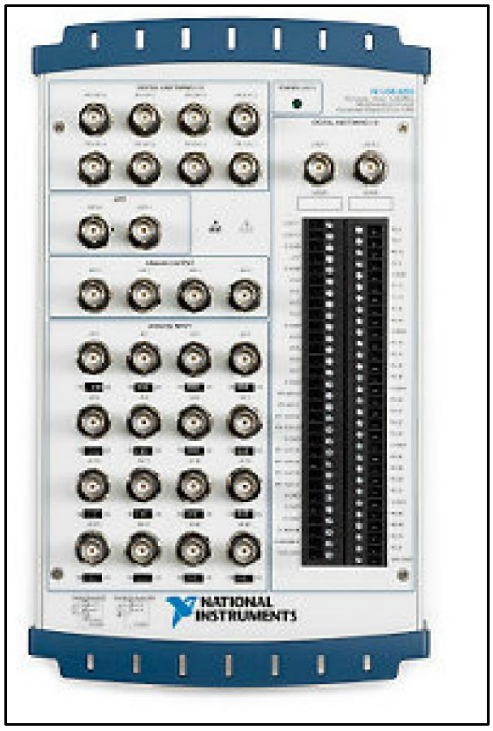

Figure 24: National Instruments USB-6259 Data Acquisition Device

The national instruments usb-6259 DAQ board consisted of 16 differential analog inputs (16-bit) capable of measurements at 1.25 MS. Picture in Figure 24, it also had 4 analog outputs and 48 digital input/outputs and was suitable for sustained high-speed data streams over USB.

The visual interface, **tunnelcontroller.vi**, is pictured in Figure 25. Real time visuals included storage pressure, stagnation pressure, pressure at port 1, pressure at point 2 and Mach number based off either pressure port 1 or pressure port 2. The **tunnelcontroller.vi** was only modified slightly for the purposes of this tunnel to incorporate a manual mode. Data was

exported from the tunnelcontroller.vi into a text file and read into MATLAB to a customized program for data management and plotting.

Figure 25: LabVIEW Visual User Interface for Tunnel Controller

Tunnel test section pressure was acquired via Omegadyne PX209 pressure transducers, pictured in Figure 26. The gages, measuring absolute pressure, consist of a silicon deflectable diaphragm when excited by 5 volt input will yield a 0 to 5 volt output. The PX209 is capable of measuring anywhere from ±15 psi pressures. The output is measured at 0 volts at vacuum and 5 volts at ambient pressures.

Figure 26: Omegadyne PX209 Absolute Pressure Transducer

2.2.2 Centerline Flow Visualization

A sting was designed. This was necessary to test the centerline Mach number right after the nozzle exit and to demonstrate the capabilities of the tunnel. One method to perform was to make a sting whereby a wedge would be attached to the sting in order to measure the shock wave angle via Schlieren visualization. If a cone was employed then the custom designed Taylor Maccolli Solution included at the end of this document in the appendix could be used to "read" the Mach number.

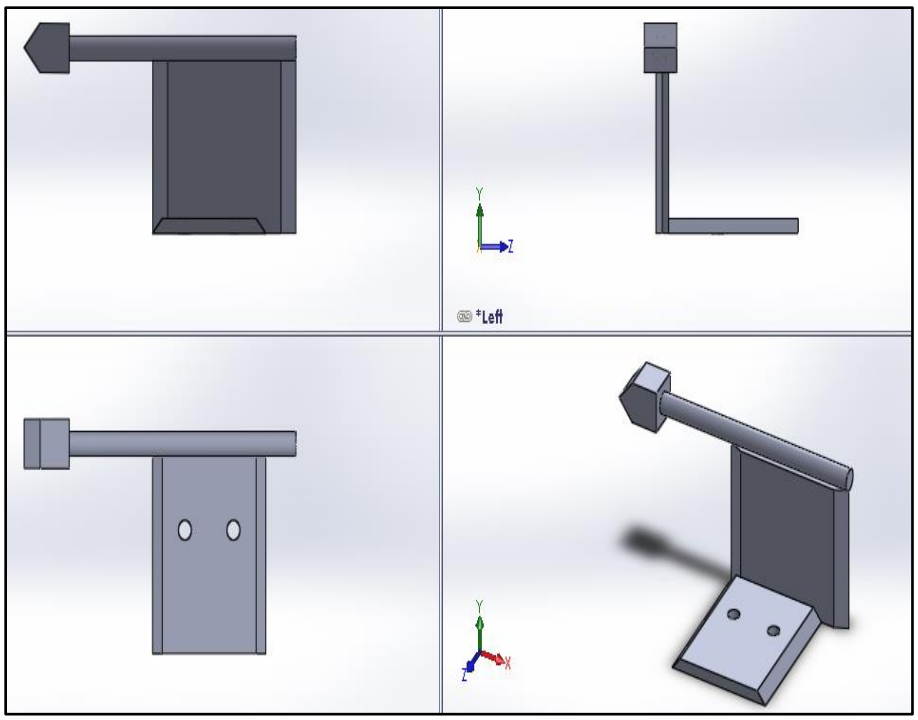

Figure 27: Sting Assembly

2.2.3 HeNe Laser Light Source

A Thor Labs HNL210Lcoherent laser source, as seen in Figure 28, was acquired from Thor Labs Company for the purpose of Schlieren and shadowgraphy. The laser selected was a 632.8 nm central wavelength Helium-Neon laser with a linearly polarized output beam. Output beam power measured 21.0 milliwatts and the beam divergence measured 1.15 milliradians. From the figure below, the laser was a cylindrical tube design that was designed to mount easily in a custom optical setup. Other important features include a beam diameter of 0.7 millimeters, polarization ratio of 500:1, and longitudinal mode spacing of 257 megahertz.

For quality Schlieren flow visualization, all optics and imaged flow must lie in same horizontal plane at a common vertical distance off the ground. To set up for flow visualization, the coherent laser light source was mounted in a cage mounted to an optical breadboard. The

cage mount allowed for four sliding rods to pass thorough on which the diverging optic was placed. This setup is picture in Figure 28.

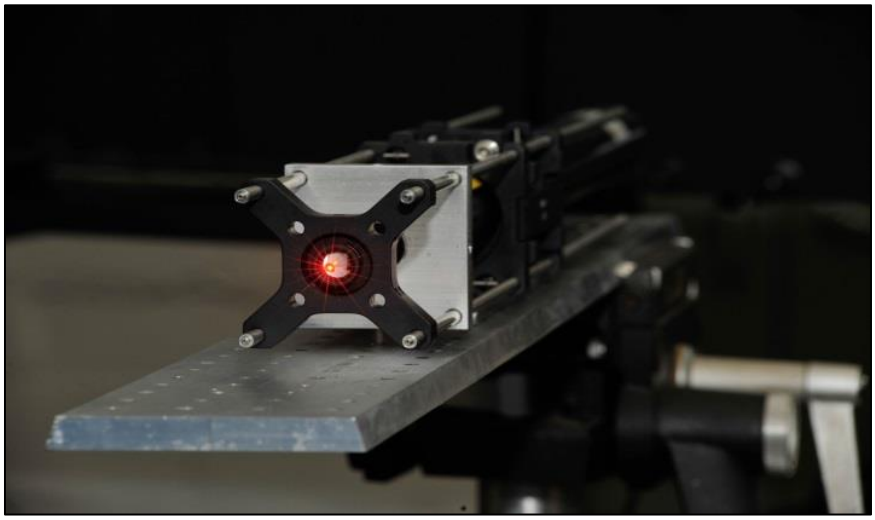

Figure 28: Laser Cage Mounted System

Chapter 3

WIND TUNNEL ASSEMBLY

3.1 Assembly Instructions

After the design of the wind tunnel components, assembly was initiated. Integrity of the wind tunnel assembly during the construction process was important. All parts were designed in SolidWorks after which all machined components were taken to be electrochemically anodized. To begin construction a flange was machined with a hole pattern identical to that of its corresponding stagnation chamber flange. Before bolting the flange to the stagnation chamber with one inch bolts, 4 flow guides were installed on the side of the flange to extend into the stagnation chamber for purpose to direct the flow towards the nozzle. The combination of the flange and the guides is illustrated in Figure 29. The guide slopes were given a sharp edge to ensure the integrity of the startup flow. Following the placement of the guides the flange was bolted to the stagnation chamber with careful precision given to making sure the flange was perfectly level and to ensure that the nozzle was squared.

Nozzle placement was one of the most critical aspects of the assembly process because if not done correctly, then the flow at the joints in the aluminum had a great potential to be compromised. The flange possessed a rectangular cutout that secured c shaped aluminum blocks holding the windows into place. This allowed for the nozzle to be recessed within the flange which is ideal for sealing and structural integrity. The geometry is illustrated in Figure 30.

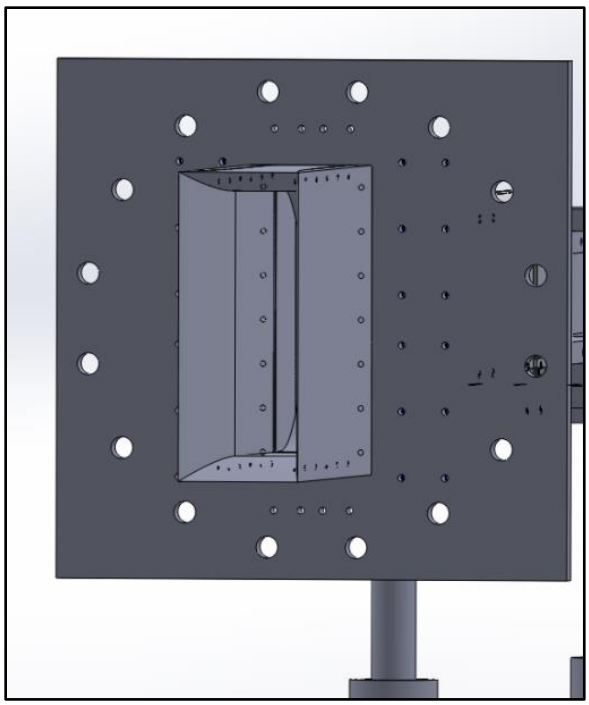

Figure 29: Forward Flange and Flow Guides for Mating to the Stagnation Chamber

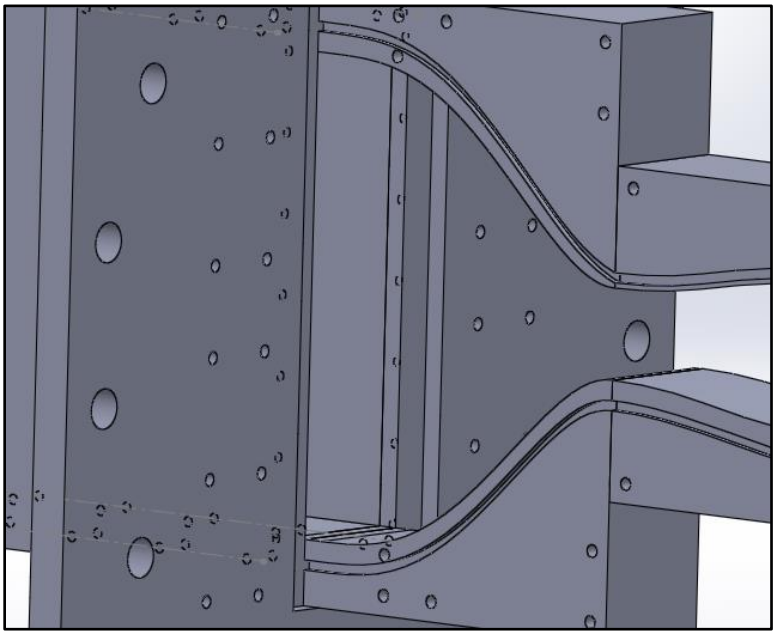

Figure 30: Illustration of Nozzle-Flange Mate

Two L-shaped brackets further secured the nozzle into place anchoring the nozzle blocks to the forward flange. The two blocks, pictured in blue below, were designed with a total of 8 possible adjusting bolts of 3/8 inch diameter. These were loosened and tightened in an organized fashion until both nozzle blocks were perfectly leveled and all gaps between the mating surfaces between the converging portion of the nozzle, the flange, and the stagnation guides were eliminated.

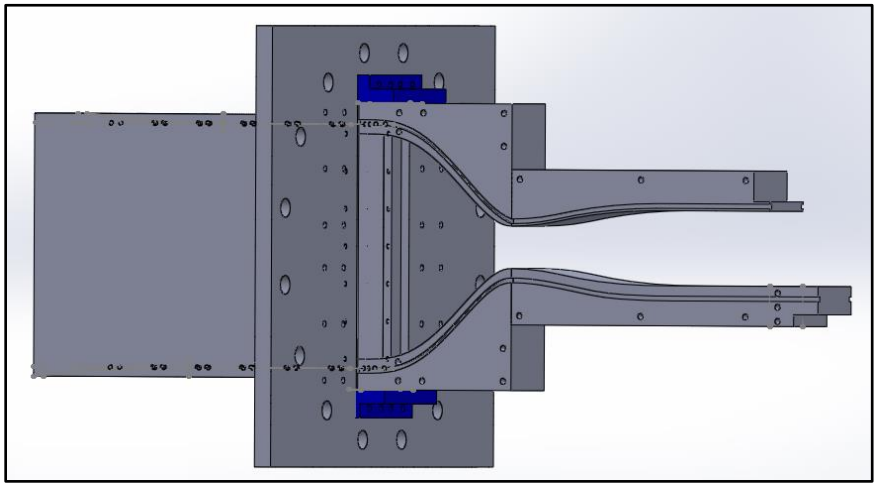

Figure 31: Illustration of Nozzle Adjustment Blocks

Following nozzle alignment, a casting support system and side windows were incorporated. Windows were machined out of 1 inch optics grade acrylic with a special extrusion made to fit in a groove located within the C-shaped aluminum pieces shown in Figure 32.

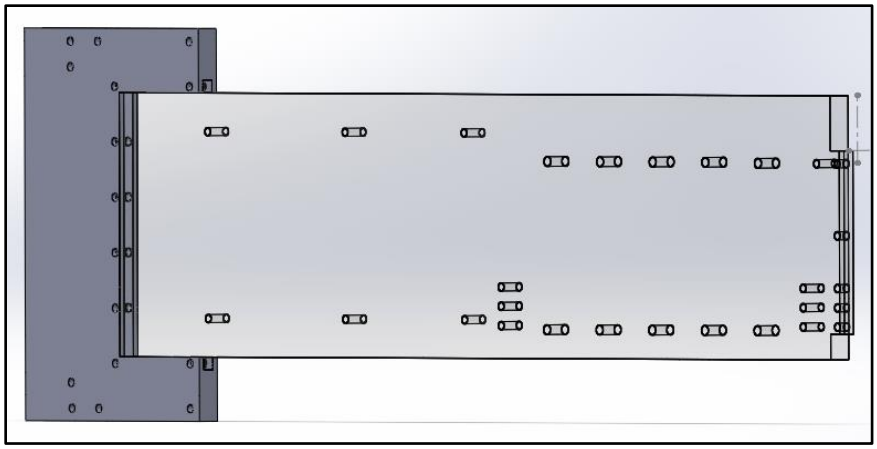

Figure 32: Acrylic Windows With Permanent Aluminum Flange

This assembly was inserted into the recessed area of the flange and between the mount of the casting system pictured in Figure 33.

The support system was designed with two ultra high strength rolling casters capable of supporting up to 500 punds per wheel. An optimum distance of 57 inches between the two trusses of the casting system was chosen to evenly support the weight of all of the components. The two jacks located in the center of the post were designed with 2 inch thick all-threaded rods. These jacks were designed to level all components which in turn made sure that there were not any gaps between any of the components.

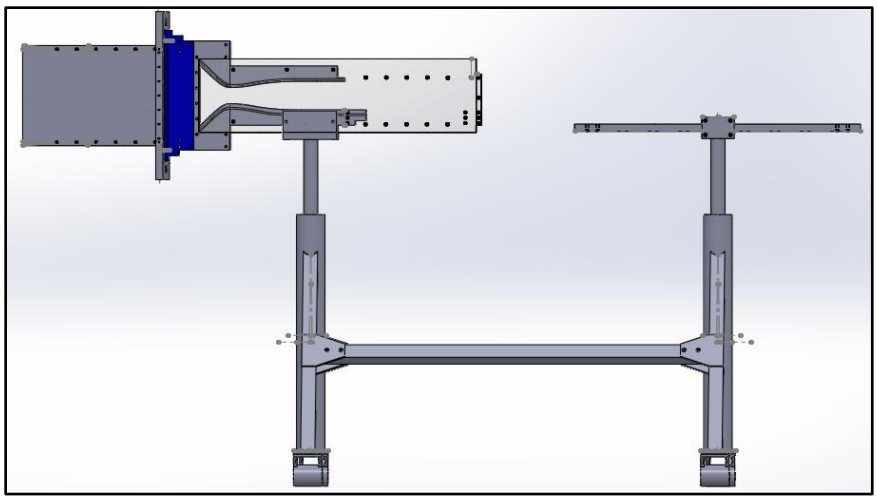

Figure 33: Wind Tunnel with Glass and Support System

Once the support system was in place, the downstream portion of the tunnel was assembled. The downstream section was placed on the support system and fastened using two square clamp mounts constructed out of aluminum. It was then aligned using the jacks and the 16 holes in the window designed to mate with the downstream section. The reason that this step was accomplished before the test section was inserted was to ensure unreasonable loads weren't placed on the acrylic test section.

Followinng insertion of the downstream section of the tunnel. The cavity base portion of the test section and the test section ceiling of the test section were inserted. Square 1.5 inch cross section blocks were placed in the cavity space to give the cavity a length to depth ratio (L/D) of 1.67. The completed virtual design is shown in Figure 34. All solid models with dimensional information are included in Appendix 5.

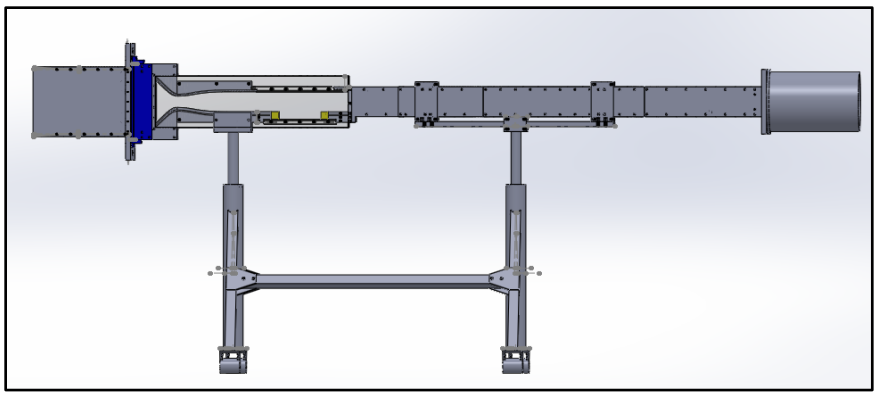

Figure 34: Completely Assembled Wind Tunnel

3.2 Startup

To operate the wind tunnel the compressor was allowed to reach a sump pressure of 40 psi and then compression was initiated. The air is cycled through the Ingersoll Rand dryer and pumped to the storage tanks until the pressure of the air in the storage tanks reached 125 psi. At this point the tunnel is ready to operate with an input excitation voltage to the piloting valve.

3.3 Flow Visualization Setup

Schlieren was used to visualize shock/expansion and shear layer. This mechanism takes advantage of the fact that light refracts as it passes through materials with different densities.

3.3.1 Schlieren and Shadowgraph Setup

The Thor Labs 21.5 mW coherent light source was placed at a focal distance of 52 inches from a parabolic mirror of a 9.5 inch diameter. The resulting collimated laser light was projected through the tunnel test section towards an identical second parabolic mirror. The resulting light was allowed to reflect off of a flat front surface mirror where it converged to a point and expanded again onto a viewing screen completing the shadowgraph setup. A flat surface mirror was used due to space restraints. The setup is pictured in Figure 35.

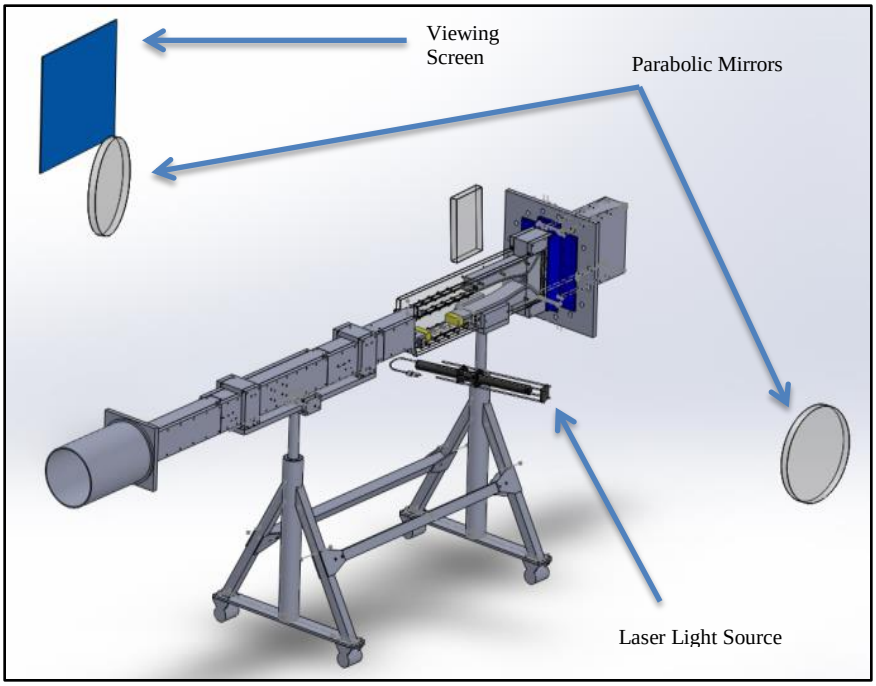

Figure 35: Shadowgraph Setup

This system was easily transitioned to the Schlieren Setup from the shadowgraph setup by the insertion of a knife edge at the focal point of the second mirror directly before the image projected to the viewing screen. This was used to partially block the light at the focal point. A razor was used to prevent flaring. The setup can be seen in Figure 36 and Figure 37.

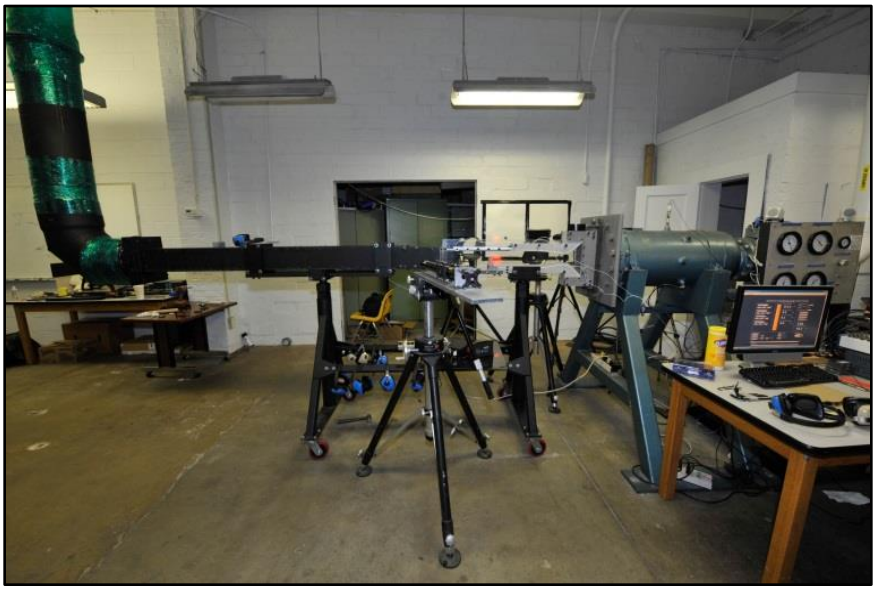

Figure 36: Optical Setup

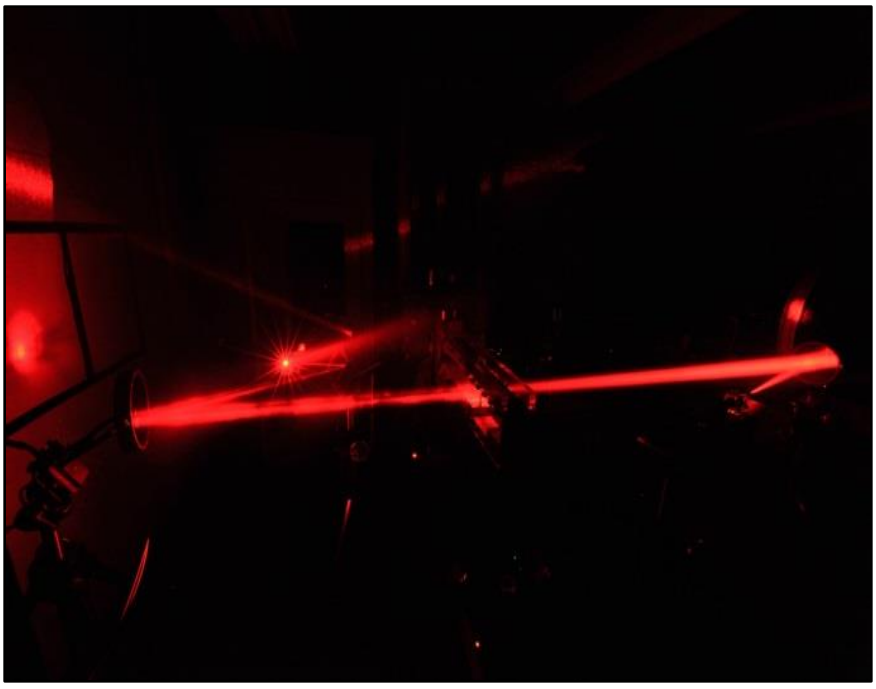

Figure 37: Smoke Trace of Laser During Schlieren Studies

3.4 Quantitative Data Acquisition Setup

Three different variants of Omegadyne PX209 pressure transducers were used. Two pressure transducers capable of reading pressures up to 200 psi were used to read the regulated pressures across the chamber valve pictured in Figure 23 and the storage pressure. An Omegadyne px209 pressure transducer capable of reading up to 100 psi was used to monitor the stagnation pressure measured just upstream of the nozzle guides shown in Figure 29 . Two Omegadyne px209 pressure transducers capable of reading ±15 psi were used to monitor the static pressure. Their calibration curves were inputs into the LabVIEW program and are pictured in the following figures.

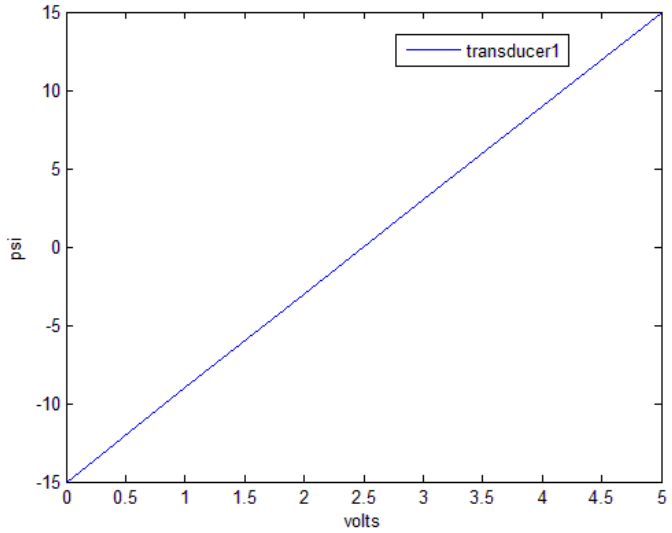

Figure 38: Calibration of PX209-30V15G5V Pressure Transducer

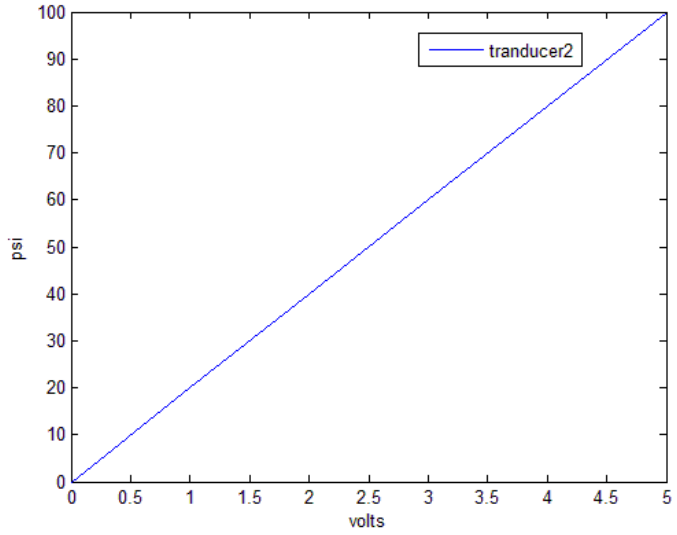

Figure 39: Calibration of PX209-100G5V Pressure Transducer

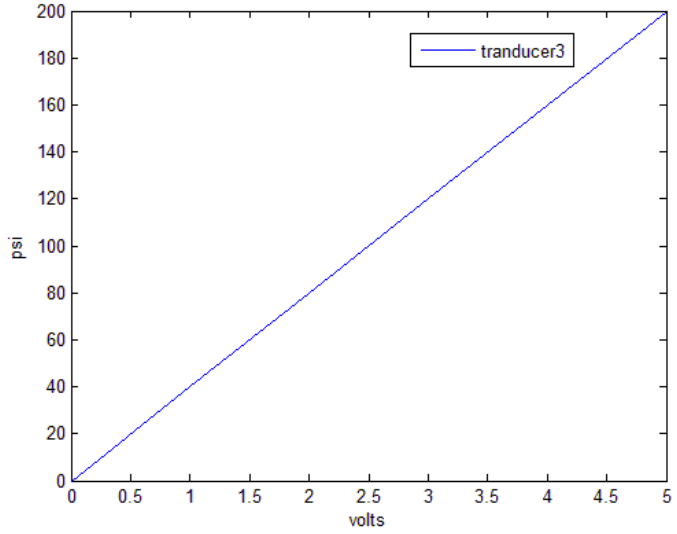

Figure 40: Calibration of PX209-200G5V Pressure Transducer

Chapter 4

QUALIFICATION OF THE WIND TUNNEL

4.1 Completed Tunnel Design

The primary objective of this research was to design a modular wind tunnel for open cavity flow acoustics measurements and shear layer analysis via optical measurement tools. Of upmost importance was to design a cavity acoustics facility that had optical access from the nozzle throat extending well past the cavity and in the test section from all sides. This objective was successfully achieved.

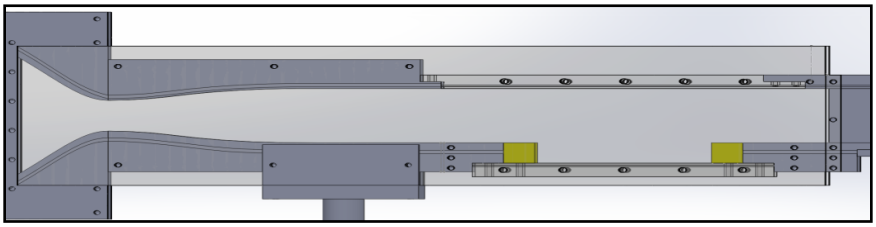

Figure 41: Lateral View of Nozzle and Test Section

Shadowgraphy was used to examine the nozzle throat for inspection of the flow characteristics at the throat. Pictured below was the first set of characteristics lines in the nozzle. The center of the nozzle corresponded to the center of the intersection. The sharp symmetrical intersection was indicative of the cleanliness of flow at the throat and the alignment of the two nozzle blocks.

Figure 42: Mach Lines at Nozzle Throat

4.2 Tunnel Flow Validation

Pressure data was acquired via a National Instruments data acquisition in conjunction with a LabVIEW controller, discussed earlier, to monitor storage pressure, stagnation pressure, and test section pressure. Two Omegadyne PX209 pressure transducers were placed above the test section on the ceiling of the wind tunnel, one being right after the exit of the nozzle and one being on the roof slightly aft of the rear face of the cavity. The resulting pressures were recorded to assess the performance of the newly designed wind tunnel. A supersonic run time of 30 seconds was achieved followed by a sharp decrease to the subsonic flow regime. A maximum Mach number of approximately 1.9 was repeatedly achieved. Short run times were directly attributed to viscous effects and a decrease in back pressure dictated by an existing piloting valve.

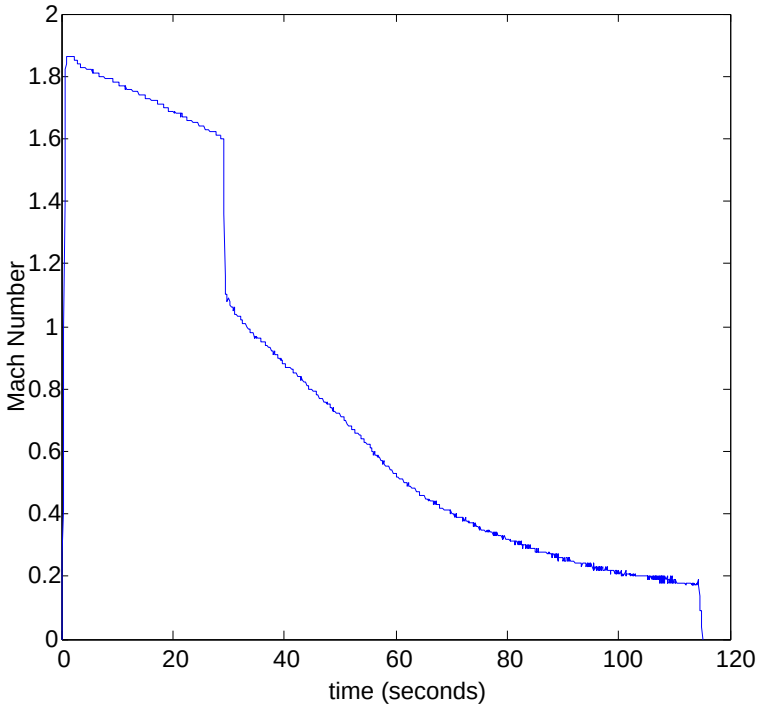

Figure 43: Mach Number Time History

Maximum stagnation pressures of approximately 69 psi were noted. This was in part due to storage-to-stagnation pressure ratio of 1.8125 established by the piloting valve system. A sharp decrease in pressure was observed and approximately 40 percent of maximum stagnation pressure was lost in the opening 10 seconds. By 20 seconds over 60 percent of maximum stagnation pressure was lost and the flow was instantly driven subsonic by the pressure ratio. An identical trend was observed in the stagnation as the storage-to-stagnation pressure ratio was being driven by the 1.8125 pressure ratio across the valve which was simply a manufacturing specification.

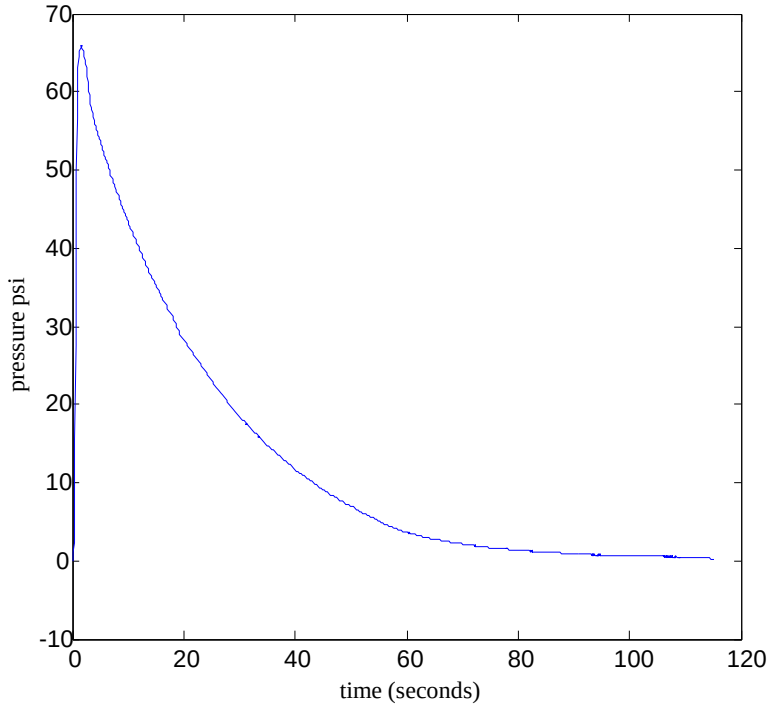

Figure 44: Stagnation Pressure Time History

The test section pressure history was recorded in Figure 45. This trend showed a very noticeable downward trend in stagnation pressure in the supersonic region followed by a sharp pressure rise at the sonic point indicating that the pressure ratio, test section pressure to stagnation, had reached critical levels and Mach number becoming subsonic. As this pressure ratio decreased flow velocity decreased until completion of the run. Pressure port location 2, located downstream of the cavity, displayed slightly lower pressures for the majority of the run as the flow was expected to slightly increase in velocity as it expanded slightly over the trailing edge of the cavity.

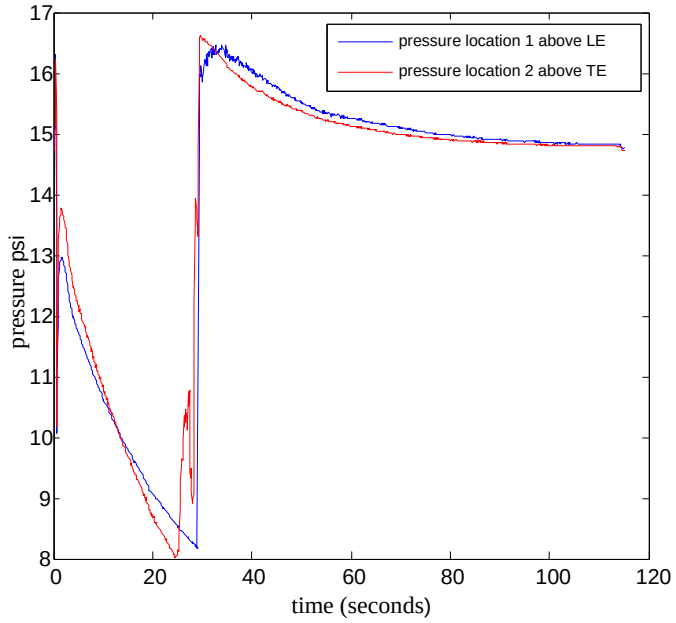

Figure 45: Test Section Pressure Time History

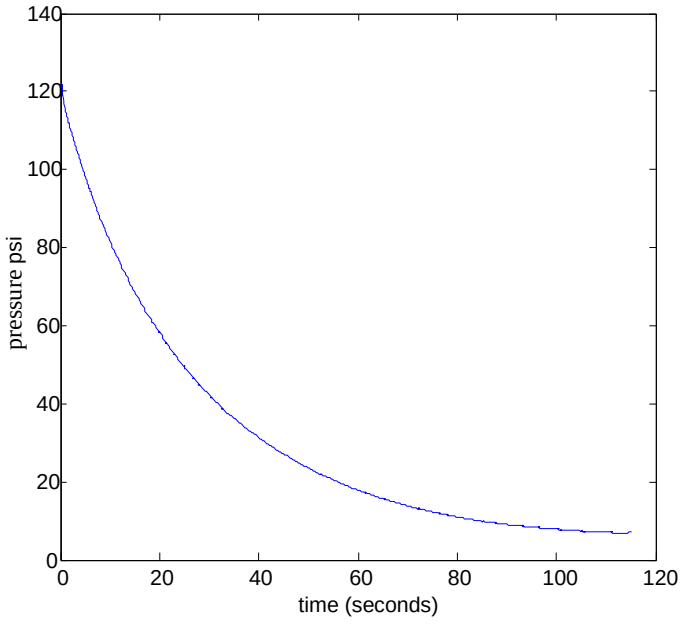

Figure 46: Storage Pressure Time History

4.3 Baseline Cavity Tunnel Case

Shadowgraphy was used to confirm the open cavity flow regime. Still photos were sufficient to confirm open flow with a visible shear layer emanating from the leading edge of the forward face. An expansion was clearly evident which is typical for supersonic flows with a sudden discontinuity in geometry of angle greater than ninety degrees.

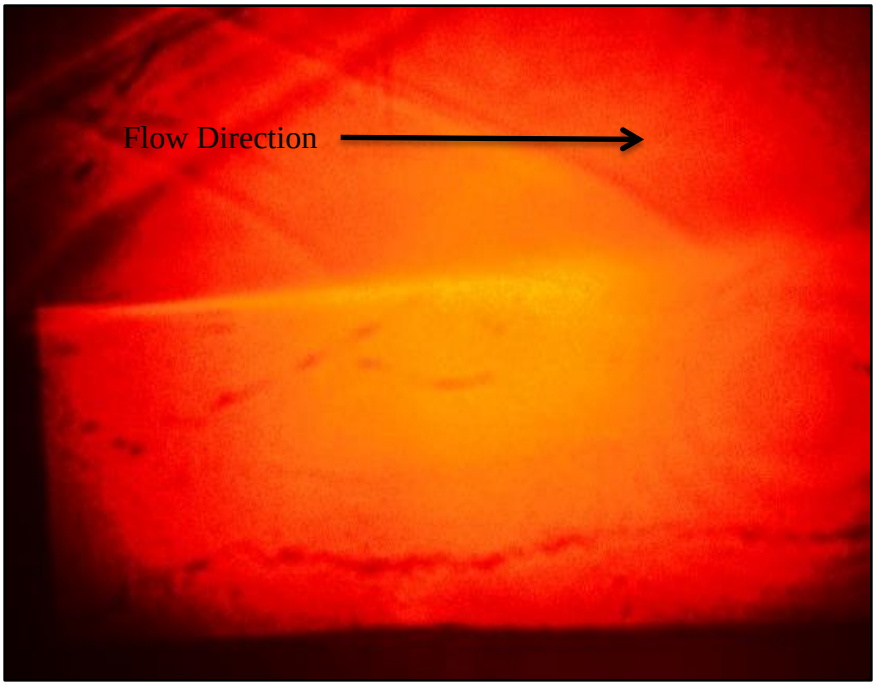

Figure 47: Leading Edge Shadowgraphy

Shadowgraphy was also paired with a high resolution camera and used to visualize the flow that spanned the cavity. The resulting Schlieren photograph, reference in Figure 48, shows the entire shear layer. The shear layer exhibited fairly rapid growth as it spanned the cavity and impinged on the rearward face, an interaction critical for both flow acoustic coupling and the production of edge tones. As the shear layer separated from the leading edge it grew at approximately the rate of thirteen degrees for half of the cavity length after which this growth rate significantly decreased. Visible fluctuations were observed within the shear layer

particularly near the impingement point located at the rear face of the open cavity. Shadowgraphy provided evidence of shed vortices being deflected into the cavity while other vortices, and cut vortices, escaped over the cavity. Video evidence suggested that the shear layer oscillated up and down in a reoccurring “flapping” motion as mentioned by previous researchers such as Zhang [30]. Bifurcation of the shear layer into inward flow and outward flow is evident incating the temporal nature of the cavity oscillations.

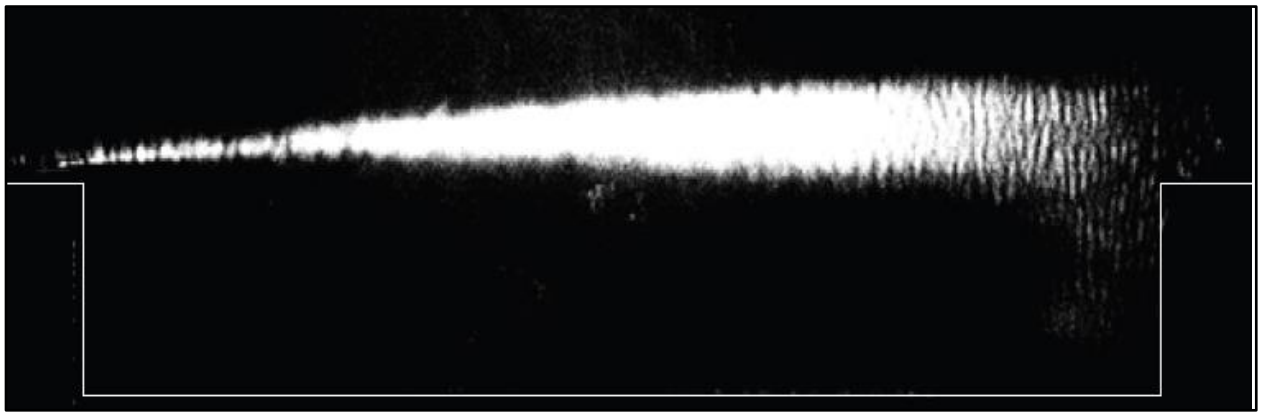

Figure 48: Full Scale Schlieren Photograph (Mach=1.9)

Chapter 5

CONCLUSIONS AND RECOMMENDATIONS FOR FUTURE RESEARCH

5.1 Conclusions

A Mach 2 wind tunnel for cavity acoustics research was successfully completed. Schlieren and shadowgraphy were used to verify that clean open cavity flow was achieved, and pressure transducers were used to verify the operating conditions. The aim was to design a system means to answer several important questions regarding the propagation of pressure waves in a shear layer impinging on the rearward face of an open cavity flow.

The tunnel is very modular in nature, and is capable of incorporating both active and passive flow control devices and modification of both the forward and rear faces of the cavity. The cavity acoustics tunnel will be an excellent facility for research in the area of aero-acoustics.

5.2 Recommendation for Piloting System

The chamber valve was observed to be operating normally. However, stagnation pressures need to be higher in order to hold Mach 2 for a period of time. This will allow the user to adjust the Reynolds number pertaining to the flow. A more reasonable pilot choice is suggested. Spence Engineering manufactures a piloting valve, Type A, that would dramatically increase the availability of future results capable with all tunnels connected to the chambering system. The Type A has a more favorable 1 to 1 delivery to loading pressure ratio over the 1 to 1.8125 Type 86 currently in-use.

5.3 Unsteady Pressures Measurement

To take full advantage of the novel wind tunnel design, instantaneous vertically oriented optical shear layer analysis in coordination with unsteady pressures measurement along the cavity base would certainly need to be implemented. No researchers have recorded observations looking through the supersonic shear layer.

Multiple peaks, referred to as cavity “modes”, characterize the frequency spectra of unsteady cavity pressures. If research only monitors the time averaged spectra, no clear observations could be made about whether or not these modes coexist with one another or experience mode switching where the energy, peaks, in one mode would shift to another mode.

Joint time frequency analyses in the forms of Fourier transform and wavelet transform can be an effective tools. By Employing the Fourier transform, a two dimensional map in the time frequency space could be visualized to show how the frequency content of the signal evolves with time. Kegerise and Spina accomplished time space frequency mapping [49]. It should be noted that the short time Fourier transform has a limited temporal resolution

The power spectra sometimes exhibit peaks at the sum and difference frequencies of the Rossiter modes and can also be used when outside the Rossiter range discussed above. According to Kegerise and Spina, the power spectrum alone is incapable of providing any conclusive proof of nonlinear interactions between harmonic components because the power spectrum suppresses all phase information [49]. Using higher order spectral methods can retain the phase information establishing their usefulness quantifying the phase coupling between frequency pairs.

The power spectral density should be examined to observe the certain multiple peaks. If we were in the region where the Rossiter Equation is valid, then these would show the Rossiter

modes. At Mach 2, the plot would show us peaks indicating the harmonics of the tones. With the existence of multiple peaks in the power spectral density plot, it should be studies whether the modes coexist independent of one another or dependent of one another. If they are independent of one another, then control of them should be rather easy because it would mean that the flow is stationary from a statistical point of view [49].

The energy spectrum will be used as a quantity to express the relative magnitudes of the energy associated with eddy motions of different scales.

5.4 Shack Hartman Shear Layer Analysis

Shack Hartman analysis is used to study the wavefront distortions when a beam traverses a shear layer or some aberrating medium. A Shack Hartman sensor measures the change in slope of an optical wave-front passing through the test section. From the change in phase angle distribution the density distribution can be found in the wind tunnel. One of the benefits of having a dedicated cavity acoustics tunnel discussed here involves such a sensor. A shack Hartman sensor has an acceptable size space on the sensor for which a fixed amount of light is able to travel towards. By having a large cavity available, such as the one designed here, the sensor will be able to measure the slopes of wavefront associated with the shear layer with much better spatial resolution. The shear layer will be quantified.

5.5 3-Dimensional Particle Image Velocimetry

One of the main advantages of this new tunnel is that research at Auburn University will be able to use the optical access from all sides to apply particle image Velocimetry for quantitative cavity measurements. The application of PIV in supersonic flows can be a

particularly challenging solution. Because of the instantaneous velocity changing nature of shock waves, particle tracers must have a high frequency response [50]. Shock waves also introduce large density gradients influencing the beam propagation. Also future work must consider quantifying the optical distortion of the observation light that passes through the aerodynamic field with density differences causing the light to bend [50]. Thus, the main considerations must be accurate flow tracing and determining the correct particle seeding density. Research shows that light pulses need to be on the order of one microsecond in order to capture all information, thereby specifying a requirement in turn for the CCD camera and possible synchronization devices.

5.6 Pressure Sensitive Paint

Also of particular experimental usefulness could be pressure sensitive paint. Using this technique, a model surface is coated with the pressure sensitive paint using an airbrush of some sort. Pressure sensitive paint consists of an oxygen sensitive probe suspended in an oxygen permeable binder. Depending on the paint, the model must be placed in an oven to cure after which it can be placed in a wind tunnel. Specific LED provided wavelengths of light can then be used to excite the pressure probe that is in the makeup of the paint. Once excited the probe shifts to a higher energy state where it will emit a photon or be quenched by oxygen [50]. The luminescent light intensity is inversely proportional to the partial pressure of oxygen. Using a series of images where there is no wind tunnel flow, wind tunnel flow is on, and possibly a background image containing all ambient light, the wind tunnel flow can be examined. Pressure sensitive paint can be used to map the steady pressures within the cavity for all operating conditions.

5.7 Other future Research

Wheel well cavities of aircraft are often shaped with rounded leading edges and this tunnel could accommodate such a design for academic purposes; clearly landing gear would never be deployed supersonically.

The facility can accommodate a lid driven cavity driven by a translating wall extending from the leading edge of the cavity. Unique wall vortices are observed emanating from the tip of the lid "driving" the cavity.

An easily modified cavity such as the one designed here could accommodate a missile model whereby structural properties could be evaluated. Adjustable blocks to modify the angle of attack could simulate deployment and loads could be measured on existing stores.

References

[1] Y.L. Chan, " A Numerical study of Two Dimensional Natural Convection in Square Open Cavities," *Numerical Heat Transfer,* Vol. 8, No. 1, April 1985, pp. 65-80.

[2] B. M. Tracy and E. Plentovisch and J. Hemsch and F. Wilcox, "Effect of Sweep on Cavity Flow Fields at Subsonic and Transonic Speeds," NASA TM-217577, 2012.

[3] H. Miura and S. Kida, "Acoustic Energy Exchange in Compressible Turbulence," *Journal of Physics Fluids,* Vol. 7, No. 7, July 1995, pp. 1732-1742.

[4] A. Rona, "Self-Excited Supersonic Cavity Flow Instabilities as Aerodynamic Noise Sources," *International Journal of Aeroacoustics,* October 2006.

[5] P. Block, "Noise response of cavities of varying dimensions at subsonic speed," NASA Technical Note D-8351, 1976

[6] J.E. Rossiter, "Wind-Tunnel Experiments on the Flow over Rectangular Cavities and Subsonic and Transonic Speeds", Aeronautical Research Council Reports and Memo 3838, October 1964.

[7] C. Rowley and T. Colonius and A Basu, " On self-sustained oscillations in two-dimensional compressible flow over rectangular cavities," *Journal of Fluid Mechanics,* Vol. 455, No. 2, 2002, pp. 315-346.

[8] L. Crocco and L. Lees, "A Mixing Theory for the Interaction Between Dissipative Flows and Nearly Isentropic Streams," *Journal of the Aeronautical Sciences,* Vol. 19, No. 10, 1952, pp. 649-676.

[9] D. A. Norton, "Investigation of B47 Bomb Bay Buffet," Boeing Airplane Co Document No. D12675, 1954.

[10] K. Krishnamurthy, "Sound radiation from surface cutouts in high speed flow," California Institute of Technology, 1956, Doctors Dissertation.

[11] U. Chandra and B. Chakravarthy, "Experimental Investigation of Cavity-Induced Acoustic Oscillations in Confined Supersonic Flow," *Journal of Fluids Engineering,* Vol. 127, 2005, pp. 761-769.

[12] D.R. Chapman, “Laminar Mixing of a Compressible Fluid,” NACA Report 958, 1950.
[13] R.E. Larson and C.J. Scott and D.R Elgin and R.E Seiver, “Turbulent Base Flow Investigations at Mach Number 3,” NASA CR-55718, 1962.

[14] H.E. Plumbee and J.S. Gibson and L.W. Lassiter, “A Theoretical and Experimental Investigation of the Acoustic Response of Cavities in an Aerodynamic Flow,” U.S. Air Force WADD-TR-61-75, March 1962.

[15] I. Tani and M. Iuchi and H. Komodo, “Experimental Investigation of Flow Separation Associated with a Step or Groove,” Aeronautical Research Institute, University of Tokyo Rept. No. 364, 1961.

[16] J.P. Rhudy and J.D. Magnan, “Turbulent Cavity Flow Investigation at Mach Numbers 4 and 8,” U.S. Air Force AEDC-TR-66-73, June 1966.

[17] L.F. East, “Three Dimensional Flow in Cavities,” *Journal of Fluid Mechanics*, Vol. 16, No. 4, 1963, pp. 620-632.

[18] H.H. Heller and D. B. Bliss, “The physical mechanism of flow induced pressure fluctuations in cavities and concepts for their suppression,” AIAA Paper No. 75-491, 1975.

[19] A.J. Bilanin and E.E. Covert, “Estimation of Possible Excitation Frequencies for Shallow Rectangular Cavities,” *AIAA Journal*, Vol. 11, No. 3, March 1973, pp. 347-351.

[20] J.C. Hardin and D. S. Pope, “ An acoustic/viscous splitting technique for computational Aeroacoustics,” *Theoretical and Computational Fluid Dynamics*, Vol. 6, No. 5, 1973, pp. 347-351.

[21] V. Sarohia, “Experimental investigation of oscillations in flow over shallow cavities,” *AIAA Journal*, Vol. 15, No 7, 1977, pp. 984-991.

[22] M. Gharib and A Roshko, “ The effect of flow oscillations of cavity drag,” *Journal of Fluid Mechanics*, Vol. 177, 1987, pp.501-530.

[23] M. Nishioka and T Heijima and T. Sunami and S Sakaue,” *Proc. Int. Sym., On Dynamics and Statics of Coherent Structures in Turbulence: Roles of Elementary Vortices*, pp. 217-228.

[24] T. Handa, “Visualization of an Oscillatory Supersonic Cavity Flow Using LIF and Schlieren Methods,” *Transactions of the Japan Society of Mechanical Engineers*, Series B, No. 78.791, 2012, pp. 1318-1326.

[25] C. K. W. Tam and P.J. Block, “ On the tones and pressure oscillations induced by flow over rectangular cavities,” *Journal of Fluid Mechanics*, Vol. 89, No. 2, 1978, pp. 373-399.

[26] D. Rockwell and E. Naudascher, "Self-sustaining oscillations of flow past cavities," *Journal of Fluids Engineering*, Vol. 100, 1978, pp. 152-165.

[27] U. Chandra and B. Chakravarthy, "Experimental Investigation of Cavity-Induced Acoustic Oscillations in Confined Supersonic Flow," *Journal of Fluids Engineering*, Vol. 127, 2005, pp. 761-769.

[28] X. Zhang and A. Rona, "An Observation of Pressure Waves Around a Shallow Cavity," *Journal of Sound and Vibration*, Vol. 214, No. 4, 1998, pp. 771-778.

[29] R. A. Smith and E. Gutmark and K.C. Schadow, "Mitigation of pressure oscillations induced by supersonic flow over slender cavities," *Journal of Aircraft*, Vol. 29, pp. 999-1004.

[30] X. Zhang and A. Rona, " Attenuation of Cavity Oscillation Through Leading Edge Flow Control," *Journal of Sound and Vibration*, Vol. 221, No. 1, 1999, pp. 23-47.

[31] L. S. Ukeiley and M.K. Ponton and J.M. Seiner and B. Jansen, "Suppression of Pressure loads in resonating cavities through blowing," AIAA Paper 2003-0181, January 2003.

[32] L.N. Cattafesta and S. Garg and M. Choudhari and F. Li, "Active Control of Flow Induced Cavity Resonance," AIAA Paper 97-1804, June 1997.

[33] L. S. Ukeiley and M. K. Ponton and J. S. Seiner and B. Jansen, "Suppression of pressure loads in cavity flows," AIAA Paper 2002-0661, January 2002.

[34] P.C. Bueno and H. Nalmis and N.T. Clemens and D.S. Dolling, "The effects of upstream mass injection on a Mach 2 Cavity Flow," AIAA Paper 2002-0663, January 2002.

[35] R. L. Sarno and M. E. Franke, "Suppression of Flow-Induced Pressure Oscillations in Cavities," *Journal of Aircraft*, Vol. 31, No. 1, 1994, pp. 90-96

[36] D. Fabris and D. R. Williams, " Experimental Measurements of cavity and shear layer response to unsteady bleed forcing," AIAA Paper 99-0606, January 1999.

[37] G. Raman and S. Raghu and T.J. Bencic, " Cavity Resonance Suppression using Miniature Fluidic Oscillators," AIAA Paper 99-1900, May 1999.

[38] R.F. Schmit and D.R. Schwartz and V Kibens and G. Raman and J. A. Ross, "High and Low Frequency Actuation Comparison for a Weapons Bay Cavity," AIAA Paper 2005-0795, January 2005.

[39] M. Stanek and G. Raman and V. Kibens and J. Ross and J Odedra and J. Peto, " Control of Cavity Resonance through Very High Frequency Forcing," AIAA Paper 2000-1905, June 2000.

[40] M. Stanek and G. Raman and J.A. Ross and J. Odedra and J. Peto and F. Alvi and V. Kibens, " High Frequency Acoustic Suppression- The Mystery of the Rod in Crossflow Revealed," AIAA Paper 2003-0007, January 2003.

[41] L. Shaw and S. McGrath, "Weapons Bay Acoustics: Passive or Active Control," AIAA Paper No. 1617-CP. 1996.

[42] L. Shaw, "Active Control for cavity acoustics," AIAA Paper No. 30885.1998

[43] A.M Lamp and N. Chokami, " Control of cavity resonance using steady and oscillatory blowing," AIAA Paper No. 99-0999, 1999.

[44] S. Raghu and E. Chesnutis and A. Bawa, "Miniature fluidic devices for flow control," ASME FEDSM 99-7256, 1999.

[45] P Hemon and J Wojciechowski, "Attenuation of cavity internal pressure oscillations by shear layer forcing with pulsed micro jets," *European Journal of Mechanics*, Vol. 25, 2006, pp. 939-947.

[46] D.R. Williams and D Cornelius and C. W. Rowley, " Supersonic Cavity Response to Open Loop Forcing," Princeton University, Princeton NJ 08544, USA.

[47] N. Zhuang and F.S. Alvi and M.B. Alkislar and C. Shih and D. Sahoo, "Aeroacoustic Properties of Supersonic Cavity Flows and Their Control," AIAA Paper 2003-3101, May 2003.

[48] NASA, *http: //www.grc.nasa.gov/WWW/k-12/airplane/tunnozd.html*., March 5, 2013.

[49] M. A. Kegerise and E. F. Spina, " Mode-switching and nonlinear effects in compressible flow over a cavity," *Journal of the Physics of Fluids*, Vol. 16, No. 3, 2004, pp. 673-687.

[50] R.K. Van Der Draai and R. Van Schinkel and A. Telesca, "Application of PIV in the DNW Industrial Supersonic Wind Tunnel SST," *PIVNET II International Workshop on the Application of PIV in Compressible Flows*, June 2005.

[51] K. Lynch, "Development of a 3-D Fluid Velocimetry Technique Based on Light Field Imaging," Auburn University, 2011, Master's Thesis.

[52] J.Z. Reid, "Development of a Direct Density Measurement Technique for Aero-Optic Analysis of a High-Velocity, Compressible Flow," Auburn University, 2011, Master's Thesis.

[53] Thor Labs, *http: //www.thorlabs.com*. March 5, 2013.

[54] Spence Engineering, *http: //www.spenceengineering.com*. March 5, 2013.

Appendix 1

SPENCE ENGINEERING HARDWARE

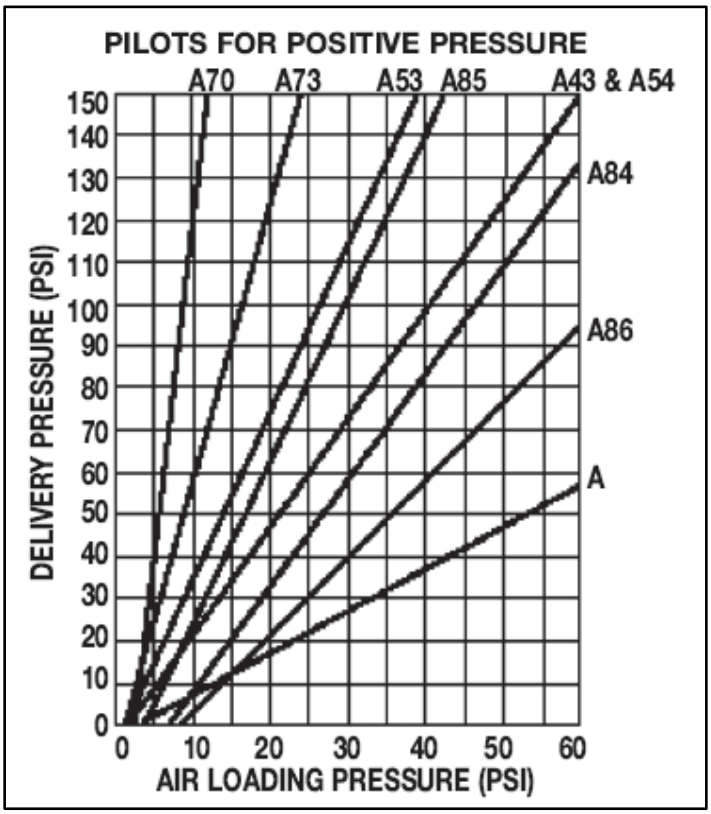

Figure 49: Spence Loading Pressure vs. Delivery Pressures [54]

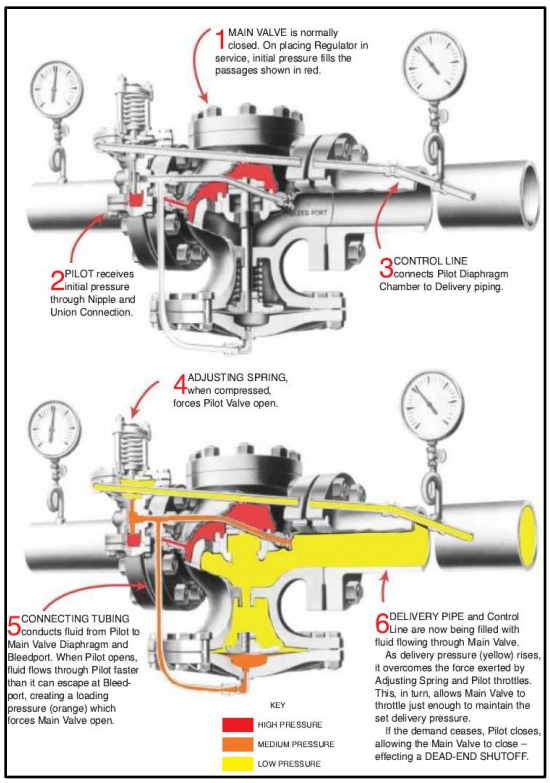

Figure 50: Operating Cycle of a Spence Type E Pressure Regulator [54]

Figure 51: Spence Type E Pressure Reducing Main Valve [54]

Appendix 2

MATLAB - METHOD OF CHARACTERISTIC SOLUTION

The following code was used to generate a wind tunnel nozzle with a smooth throat in order for the graduate researcher to understand radius of curvature effects and Mach profiles after boundary layer approximations have been made.

```
clear all
clc
format long
%%
plot_trigger = 1;%Turns on plotter
k = 1.4
M_design = 2.1;
s = 90;
theta_design = P_Mv(M_design,k)

%P_Mv put into a function file but the main Prantl Meyer Newton Raphson
%Method is included below as a way to show how it works.
theta_max = theta_design/2
del_theta = (theta_max/s)
%Total Throat Height(i.e. twice the height from the centerline)
Total_Throat = 1;
Centerline_Height = Total_Throat/2;
% Expansion circle Calculations
radius =1 ;
x_circle = 0;
y_circle = (Centerline_Height) + radius%*Centerline_Height;
expansion_radius = y_circle - Centerline_Height;
ang = (3*pi)/2;
exp_ang = theta_max*(pi()/180)
d_exp_ang = exp_ang/s
%Indexing for Speed
x_exp=zeros(s,1);
y_exp=zeros(s,1);
theta_exp=zeros(s,1);
K_minus_designxp=zeros(s,1);
K_plus_exp=zeros(s,1);
nu1=zeros(s,1);
nu2=zeros(s,1);
M_designxp=zeros(s,1);
mu_exp=zeros(s,1);
for i=1:s
```

```
    x_exp(i) = x_circle + expansion_radius*(cos(ang+d_exp_ang*i));
    y_exp(i) = y_circle + expansion_radius*(sin(ang+d_exp_ang*i));
    theta_exp(i) = del_theta*i;
    K_minus_designxp(i) = theta_exp(i)*2;
    K_plus_exp(i) = 0;
    nu1(i) = K_minus_designxp(i)-theta_exp(i);
    nu2(i) = theta_exp(i)+K_plus_exp(i);
    M_designxp(i) = M_nu(nu1(i),k);
    mu_exp(i) = mu(M_designxp(i));
end
%%
for i=1:s
    for j=1:s
        if i==1
        %Theta for each line (first lines)
        theta(i,j) = theta_exp(j);
        nu(i,j) = theta(i,j);
        K_minus(i,j) = theta(i,j) + nu(i,j);
        K_plus(i,j) = theta(i,j) - nu(i,j);
        elseif i > 1
        K_plus(i,j) = -K_minus(1,i);
        % Find Thetas
        if j >= i
        theta(i,j) = del_theta*(j-i);
        else
        %theta(i,j) = theta(j,i-1);
        theta(i,j) = theta(j,i);
        end
        nu(i,j) = theta(i,j) - K_plus(i,j);
        K_minus(i,j) = theta(i,j) + nu(i,j);
        end
        % Prandtl-Meyer function (using Newton Rhapson)
        dM = .1; % Leave at about .1
        if j == 1
        M_ex(i,j) = 1.00;
        else
        M_ex(i,j) = M_ex(i,j-1);
        end
        M = M_ex(i,j);
        res = 1;

        while res > .01
            M2 = M + dM;
            funv1 = (-nu(i,j)*(pi/180)+(sqrt((k+1)/(k-1))*...
                atan((sqrt((k-1)*(M^2-1)/(k+1))))-atan(sqrt(M^2-1))));
            funv2 = (-nu(i,j)*(pi/180)+(sqrt((k+1)/(k-1))*...
```

```
            atan((sqrt((k-1)*(M2^2-1)/(k+1))))-atan(sqrt(M2^2-1))));
        dv_dm = (funv2-funv1)/dM;
        M = M - funv1/dv_dm;
        res = abs(funv1);
    end
    M_ex(i,j) = M;
    mu(i,j) = (180/pi)*asin(1/M_ex(i,j));
  end
  % Add last point to char line
  theta(i,s+1) = theta(i,s);
  nu(i,s+1) = nu(i,s);
  K_minus(i,s+1) = K_minus(i,s);
  K_plus(i,s+1) = K_plus(i,s);
end

% x_exp
% y_exp
char = zeros(s,s+1,2);
for i=1:s
  for j=1:s+1
    %Loop Required to Draw points of intersection
    %Point 1 Of ALL Characteristic Lines
    if j == 1
      char(i,j,1) = x_exp(i);
      char(i,j,2) = y_exp(i);
    end
    %Where first line hits the symmetry line
    if i == 1 && j==2
      char(i,j,1) = (-Total_Throat/2)/tan((pi/180)*...
        (theta(1,j-1)-mu(1,j-1)));
      char(i,j,2) = 0;
    end
    %Where all other lines hit the symmetry line
    if j == i+1 && j>2
      char(i,j,1) = -char(i-1,j,2)/tan((pi/180)*(.5*theta(i,j-2)...
        -.5*(mu(i,j-2)+mu(i,j-1)))) + char(i-1,j,1);
      char(i,j,2) = 0;
    end
    %All other data points for char 1 calculated
    if i == 1 && j > 2 && j ~= i+1
      C_p = tan((pi/180)*(.5*(theta(i,j-2)+theta(i,j-1))+.5*...
        (mu(i,j-2)+mu(i,j-1))));
      C_m = tan((pi/180)*(.5*(theta(j-1,1)+theta(i,j-1))-.5*...
        (mu(j-1,1)+mu(i,j-1))));
      A = [1,-C_m;1,-C_p];
      B = [char(1,1,2) - char(1,1,1)*C_m;
```

```
            char(1,j-1,2) - char(1,j-1,1)*C_p];
            iterm(1,:) = A\B;
            char(i,j,1) = iterm(1,2);
            char(i,j,2) = iterm(1,1);
        end
        %All other points for all char lines calculated
        if i > 1 && j~=i+1 && j>2
            C_p = tan((pi/180)*(.5*(theta(i,j-2)+theta(i,j-1))+.5*...
                (mu(i,j-2)+mu(i,j-1))));
            C_m = tan((pi/180)*(.5*(theta(i-1,j-1)+theta(i,j-1))-.5*...
                (mu(i-1,j-1)+mu(i,j-1))));
            A = [1,-C_m;1,-C_p];
            B = [char(i-1,j,2) - char(i-1,j,1)*C_m; char(i,j-1,2)...
                - char(i,j-1,1)*C_p];
            iterm(1,:) = inv(A)*B;
            char(i,j,1) = iterm(1,2);
            char(i,j,2) = iterm(1,1);
        end
    end
end
% Get Characteristics Where The Characteristic Lines Share The Same Points
for i = 2:s
    for j=2:s
        char(j,i,1) = char(i-1,j+1,1);
        char(j,i,2) = char(i-1,j+1,2);
    end
end
%%
%=========>Make the nozzle shape and extend the char lines to wall<========
%============>Initial start point of the nozzle (at throat)<===============
      nozzle(1,1) = 0;
      nozzle(1,2) = Total_Throat/2;
for i=2:s
      x(i,1) = x_exp(i);
      y(i,1) = y_exp(i);
      nozzle(i,1) = x_exp(i);
      nozzle(i,2) = y_exp(i);
end
      i2=s+1;
%=============>Now we can find all the points in the nozzle<===============
for i = 2:s
      %Find different slopes and points to intersect
      m1 = tan((pi/180)*(theta(i-1,s)+mu(i-1,s)));
    if i ==2
      m2 = (pi/180)*theta_max;
    else
```

```
      m2 = ((pi/180)*(theta(i-1,s+1)));
   end
      m3 = ((pi/180)*(theta(i-1,s)));
      m4 = tan((m2+m3)/2);
       A = [1,-m4; 1,-m1];
       B = [nozzle(i2-1,2) - nozzle(i2-1,1)*m4; char(i-1,s+1,2)...
           - char(i-1,s+1,1)*m1];
      iterm(1,:) = A\B;
      nozzle(i+s-1,1) = iterm(1,2);
      nozzle(i+s-1,2) = iterm(1,1);
      %Extend char lines to wall
      char(i-1,s+2,1)= nozzle(i+s-1,1);
      char(i-1,s+2,2)= nozzle(i+s-1,2);
      i2=i2+1;
end
%Now For The Last and Final Line
m1 = tan((pi/180)*(theta(s,s)+ mu(s,s)));
m2 = ((pi/180)*(theta(s-1,s)));
m3 = ((pi/180)*(theta(s,s+1)));
m4 = tan((m2+m3)/2);
A = [1,-m4; 1,-m1];
B = [nozzle(i2-1,2) - nozzle(i2-1,1)*m4; char(s,s+1,2)...
   - char(s,s+1,1)*m1];
%iterm(1,:) = inv(A)*B;
iterm(1,:) = (A)\B;
nozzle(i2,1) = iterm(1,2);
nozzle(i2,2) = iterm(1,1);
%Extend char lines to wall
char(s,s+2,1)= nozzle(i2,1);
char(s,s+2,2)= nozzle(i2,2);

%%
if plot_trigger ==1
   %Plot the nozzle shape
   figure(1);clf;
   plot(nozzle(:,1),nozzle(:,2),'g','LineWidth',3)
   hold on;
   %Plot for loop for char lines
for i = 1:s
       figure(1)
       hold on;
       plot(char(i,:,1),char(i,:,2))
       hold on;
       plot(char(i,:,1),-char(i,:,2))
end
       %Plot the nozzle shape (bottom side)
```

```
        figure(1)
        hold on;
        plot(nozzle(:,1),-nozzle(:,2),'g','LineWidth',3)
        hold on;
        title('Wind Tunnel Nozzle Design')
        xlabel('Nozzle length (m)')
        ylabel('Nozzle height (m)')
        legend('Nozzle shape','Char. Lines')
end
        %Visualization Expansion circle
        hold on
        plot(x_circle,y_circle,'o')
for s=1:14
        xvalues(s)=nozzle(s,1);
        yvalues(s)=nozzle(s,1);
end
```

Appendix 3

A CONVERGING NOZZLE VIA A 5TH ORDER POLYNOMIAL

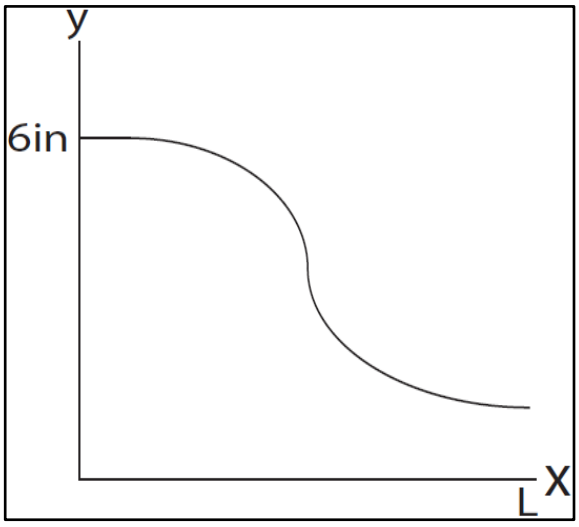

Figure 52: Converging Nozzle 5th Order

Polynomial

X=L, y=1.65199 “

X=0, $\frac{dy}{dx} = 0$

X=L, $\frac{dy}{dx} = 0$

X=0, $\frac{d^2y}{dx^2} = 0$

X=L, $\frac{d^2y}{dx^2} = 0$

Supersonic Throat = 1.65199”

Coefficient	Value	Coefficient	Value
a	-.00088162	d	0
b	0.01763233	e	0
c	-.09403908	f	6

Appendix 4

EXCEL - DATA FOR GENERATION OF MOC WIND TUNNEL NOZZLE

RAW DATA INCHES			**RAW DATA INCHES**		
0	1.2091	0	0	-1.2091	0
0.0167	1.209177	0	0.0167	-1.209177	0
0.02505	1.209273	0	0.02505	-1.209273	0
0.033399	1.209408	0	0.033399	-1.209408	0
0.041748	1.209581	0	0.041748	-1.209581	0
0.050095	1.209792	0	0.050095	-1.209792	0
0.058442	1.210042	0	0.058442	-1.210042	0
0.066787	1.21033	0	0.066787	-1.21033	0
0.075131	1.210657	0	0.075131	-1.210657	0
0.083473	1.211022	0	0.083473	-1.211022	0
0.091814	1.211425	0	0.091814	-1.211425	0
0.100152	1.211867	0	0.100152	-1.211867	0
0.108489	1.212348	0	0.108489	-1.212348	0
0.116823	1.212866	0	0.116823	-1.212866	0
0.125155	1.213423	0	0.125155	-1.213423	0
0.133484	1.214019	0	0.133484	-1.214019	0
0.14181	1.214653	0	0.14181	-1.214653	0
0.150133	1.215325	0	0.150133	-1.215325	0
0.158453	1.216035	0	0.158453	-1.216035	0
0.16677	1.216784	0	0.16677	-1.216784	0
0.175083	1.217571	0	0.175083	-1.217571	0
0.183392	1.218396	0	0.183392	-1.218396	0
0.191698	1.219259	0	0.191698	-1.219259	0
0.199999	1.220161	0	0.199999	-1.220161	0
0.208296	1.221101	0	0.208296	-1.221101	0
0.216589	1.222079	0	0.216589	-1.222079	0
0.224877	1.223095	0	0.224877	-1.223095	0
0.233161	1.22415	0	0.233161	-1.22415	0
0.241439	1.225242	0	0.241439	-1.225242	0
0.249712	1.226373	0	0.249712	-1.226373	0
0.257981	1.227542	0	0.257981	-1.227542	0
0.266243	1.228749	0	0.266243	-1.228749	0
0.2745	1.229993	0	0.2745	-1.229993	0
0.282751	1.231276	0	0.282751	-1.231276	0
0.290996	1.232597	0	0.290996	-1.232597	0
0.299235	1.233956	0	0.299235	-1.233956	0

RAW DATA INCHES			RAW DATA INCHES		
0.307468	1.235353	0	0.307468	-1.235353	0
0.315694	1.236787	0	0.315694	-1.236787	0
0.323914	1.238259	0	0.323914	-1.238259	0
0.332126	1.23977	0	0.332126	-1.23977	0
0.340332	1.241318	0	0.340332	-1.241318	0
0.34853	1.242904	0	0.34853	-1.242904	0
0.356721	1.244527	0	0.356721	-1.244527	0
0.364904	1.246188	0	0.364904	-1.246188	0
0.37308	1.247887	0	0.37308	-1.247887	0
0.381248	1.249624	0	0.381248	-1.249624	0
0.389407	1.251398	0	0.389407	-1.251398	0
0.397559	1.25321	0	0.397559	-1.25321	0
0.405701	1.255059	0	0.405701	-1.255059	0
0.413836	1.256945	0	0.413836	-1.256945	0
0.960205	1.384993	0	0.960205	-1.384993	0
1.568932	1.521755	0	1.568932	-1.521755	0
1.676639	1.545433	0	1.676639	-1.545433	0
1.811081	1.57434	0	1.811081	-1.57434	0
1.92695	1.598696	0	1.92695	-1.598696	0
2.032691	1.620415	0	2.032691	-1.620415	0
2.13159	1.640255	0	2.13159	-1.640255	0
2.225637	1.658671	0	2.225637	-1.658671	0
2.316122	1.675958	0	2.316122	-1.675958	0
2.403941	1.692316	0	2.403941	-1.692316	0
2.489739	1.70789	0	2.489739	-1.70789	0
2.574003	1.722785	0	2.574003	-1.722785	0
2.657108	1.73708	0	2.657108	-1.73708	0
2.739351	1.750838	0	2.739351	-1.750838	0
2.820974	1.764107	0	2.820974	-1.764107	0
2.902189	1.776925	0	2.902189	-1.776925	0
2.983126	1.789318	0	2.983126	-1.789318	0
3.063948	1.801312	0	3.063948	-1.801312	0
3.144778	1.812928	0	3.144778	-1.812928	0
3.225723	1.82418	0	3.225723	-1.82418	0
3.306878	1.835081	0	3.306878	-1.835081	0
3.388327	1.845639	0	3.388327	-1.845639	0
3.470147	1.855863	0	3.470147	-1.855863	0
3.552406	1.865758	0	3.552406	-1.865758	0
3.63517	1.875326	0	3.63517	-1.875326	0
3.718495	1.884571	0	3.718495	-1.884571	0

RAW DATA INCHES			RAW DATA INCHES		
3.802437	1.893494	0	3.802437	-1.893494	0
3.887047	1.902093	0	3.887047	-1.902093	0
3.972373	1.910369	0	3.972373	-1.910369	0
4.058461	1.918319	0	4.058461	-1.918319	0
4.145354	1.92594	0	4.145354	-1.92594	0
4.233095	1.933228	0	4.233095	-1.933228	0
4.321724	1.940179	0	4.321724	-1.940179	0
4.411279	1.946788	0	4.411279	-1.946788	0
4.5018	1.95305	0	4.5018	-1.95305	0
4.593322	1.958957	0	4.593322	-1.958957	0
4.685883	1.964504	0	4.685883	-1.964504	0
4.779517	1.969682	0	4.779517	-1.969682	0
4.874261	1.974485	0	4.874261	-1.974485	0
4.970148	1.978903	0	4.970148	-1.978903	0
5.067214	1.982927	0	5.067214	-1.982927	0
5.165491	1.986549	0	5.165491	-1.986549	0
5.265015	1.989757	0	5.265015	-1.989757	0
5.36582	1.992543	0	5.36582	-1.992543	0
5.467938	1.994894	0	5.467938	-1.994894	0
5.571405	1.9968	0	5.571405	-1.9968	0
5.676208	1.998247	0	5.676208	-1.998247	0
5.782471	1.999226	0	5.782471	-1.999226	0
5.890191	1.999722	0	5.890191	-1.999722	0
5.99919	1.999973	0	5.99919	-1.999973	0

Table 1: EXCEL - Data for Generation of MoC Wind Tunnel Nozzle

INCHES		METERS	
0	1.2091	0	0.030711
0.06	1.210093	0.001524	0.030736
0.12	1.213074	0.003048	0.030812
0.18	1.218054	0.004572	0.030939
0.24	1.225049	0.006096	0.031116
0.3	1.233027	0.00762	0.031319
0.36	1.24583	0.009144	0.031644
0.42	1.258852	0.010668	0.031975
0.48	1.272068	0.012192	0.032311
0.54	1.285454	0.013716	0.032651
0.6	1.298988	0.01524	0.032994
0.66	1.312646	0.016764	0.033341
0.72	1.326407	0.018288	0.033691
0.78	1.340251	0.019812	0.034042
0.84	1.354157	0.021336	0.034396
0.9	1.368106	0.02286	0.03475
0.96	1.38208	0.024384	0.035105
1.02	1.39606	0.025908	0.03546
1.08	1.410029	0.027432	0.035815
1.14	1.423971	0.028956	0.036169
1.2	1.437871	0.03048	0.036522
1.26	1.451713	0.032004	0.036874
1.32	1.465484	0.033528	0.037223
1.38	1.47917	0.035052	0.037571
1.44	1.492759	0.036576	0.037916
1.5	1.506238	0.0381	0.038258
1.56	1.519596	0.039624	0.038598
1.62	1.532823	0.041148	0.038934
1.68	1.54591	0.042672	0.039266
1.74	1.558848	0.044196	0.039595
1.8	1.571628	0.04572	0.039919
1.86	1.584243	0.047244	0.04024
1.92	1.596686	0.048768	0.040556
1.98	1.608952	0.050292	0.040867
2.04	1.621035	0.051816	0.041174
2.1	1.632931	0.05334	0.041476
2.16	1.644636	0.054864	0.041774
2.22	1.656147	0.056388	0.042066
2.28	1.667463	0.057912	0.042354
2.34	1.678581	0.059436	0.042636

INCHES		METERS	
2.4	1.689501	0.06096	0.042913
2.46	1.700224	0.062484	0.043186
2.52	1.710749	0.064008	0.043453
2.58	1.721079	0.065532	0.043715
2.64	1.731215	0.067056	0.043973
2.7	1.741162	0.06858	0.044226
2.76	1.750922	0.070104	0.044473
2.82	1.7605	0.071628	0.044717
2.88	1.769901	0.073152	0.044955
2.94	1.779133	0.074676	0.04519
3	1.7882	0.0762	0.04542
3.06	1.800201	0.077724	0.045725
3.12	1.808838	0.079248	0.045944
3.18	1.817263	0.080772	0.046158
3.24	1.825475	0.082296	0.046367
3.3	1.833477	0.08382	0.04657
3.36	1.841269	0.085344	0.046768
3.42	1.848853	0.086868	0.046961
3.48	1.856228	0.088392	0.047148
3.54	1.863397	0.089916	0.04733
3.6	1.87036	0.09144	0.047507
3.66	1.877118	0.092964	0.047679
3.72	1.883672	0.094488	0.047845
3.78	1.890024	0.096012	0.048007
3.84	1.896175	0.097536	0.048163
3.9	1.902125	0.09906	0.048314
3.96	1.907876	0.100584	0.04846
4.02	1.913429	0.102108	0.048601
4.08	1.918785	0.103632	0.048737
4.14	1.923945	0.105156	0.048868
4.2	1.928911	0.10668	0.048994
4.26	1.933684	0.108204	0.049116
4.32	1.938264	0.109728	0.049232
4.38	1.942654	0.111252	0.049343
4.44	1.946854	0.112776	0.04945
4.5	1.950866	0.1143	0.049552
4.56	1.95469	0.115824	0.049649
4.62	1.958329	0.117348	0.049742
4.68	1.961784	0.118872	0.049829
4.74	1.965055	0.120396	0.049912

INCHES		METERS	
4.8	1.968145	0.12192	0.049991
4.86	1.971055	0.123444	0.050065
4.92	1.973785	0.124968	0.050134
4.98	1.976338	0.126492	0.050199
5.04	1.978715	0.128016	0.050259
5.1	1.980917	0.12954	0.050315
5.16	1.982946	0.131064	0.050367
5.22	1.984803	0.132588	0.050414
5.28	1.986489	0.134112	0.050457
5.34	1.988007	0.135636	0.050495
5.4	1.989358	0.13716	0.05053
5.46	1.990542	0.138684	0.05056
5.52	1.991563	0.140208	0.050586
5.58	1.99242	0.141732	0.050607
5.64	1.993117	0.143256	0.050625
5.7	1.993653	0.14478	0.050639
5.76	1.994032	0.146304	0.050648
5.82	1.994255	0.147828	0.050654
5.88	1.994322	0.149352	0.050656
5.94	1.994237	0.150876	0.050654
6	1.994	0.1524	0.050648

Table 2: EXCEL - Converted Data for Generation of MoC Wind Tunnel Nozzle

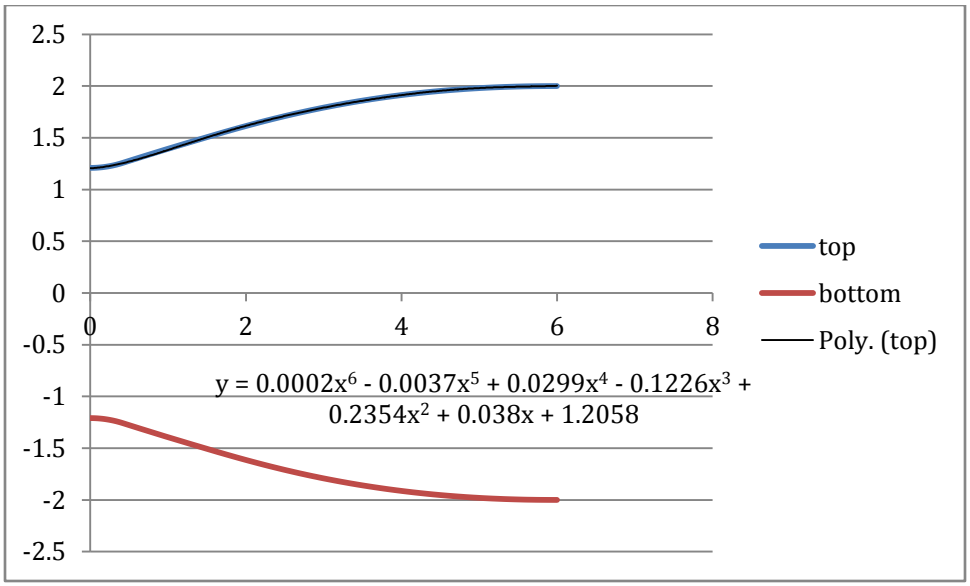

Figure 53: Excel Supersonic Nozzle

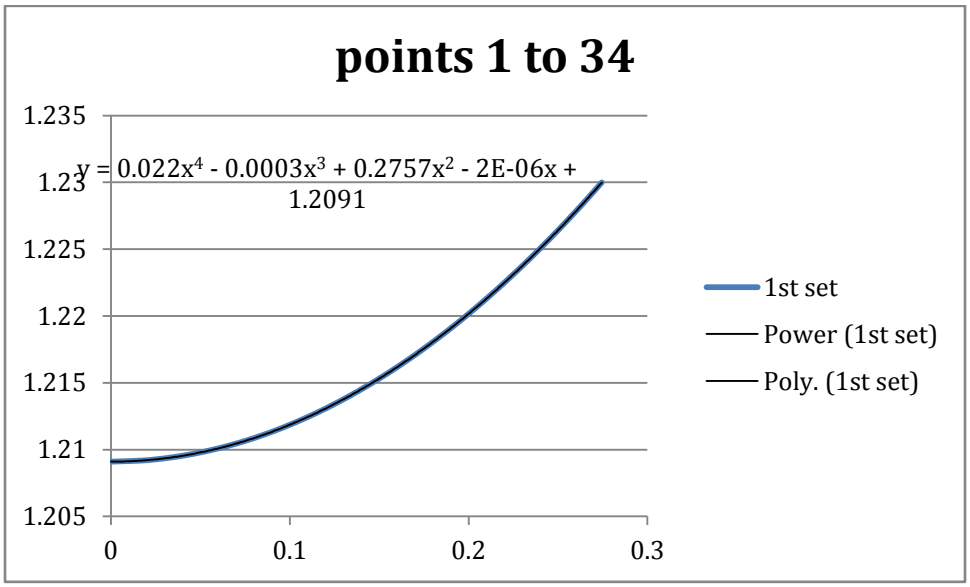

Figure 54: Initial Curve for Euler Code Visualization

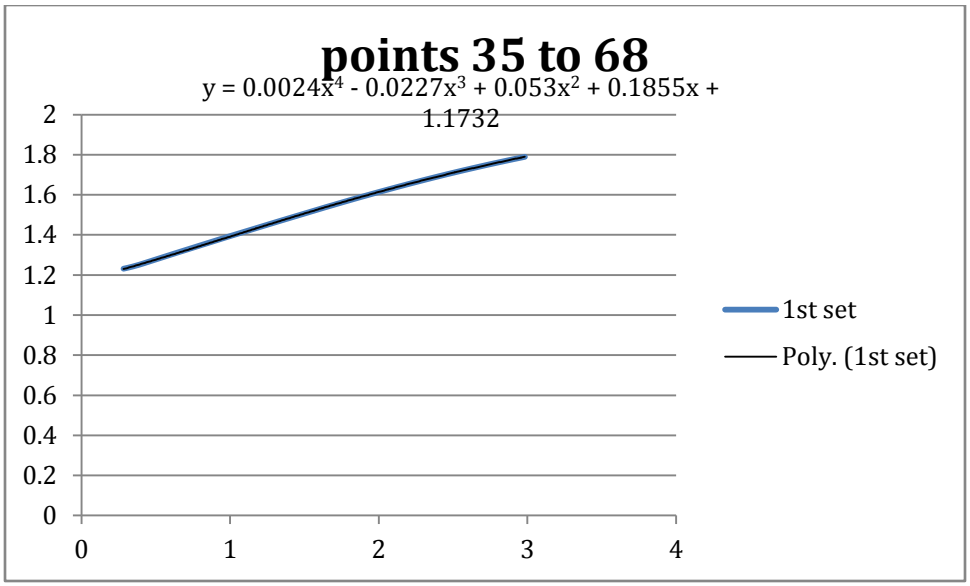

Figure 55: Secondary Curve for Euler Visualization

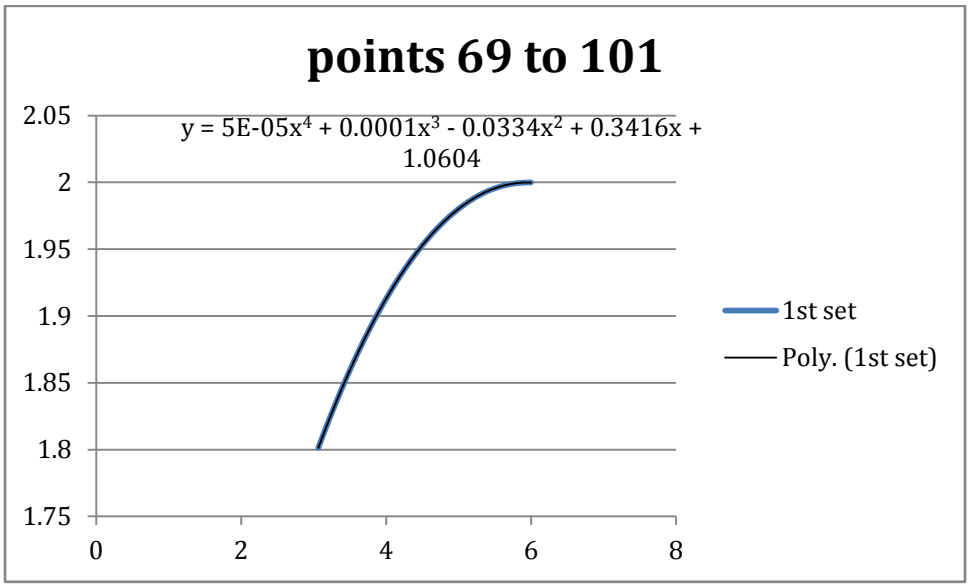

Figure 56: Tertiary Curve for Euler Visualization

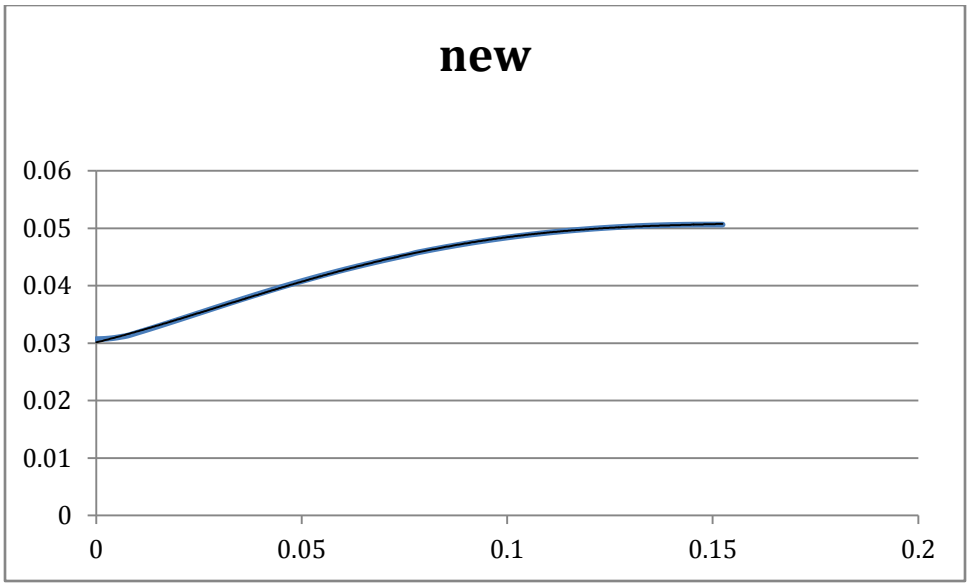

Figure 57: Excel Nozzle Formulation from Primary, Secondary, and Tertiary Curves

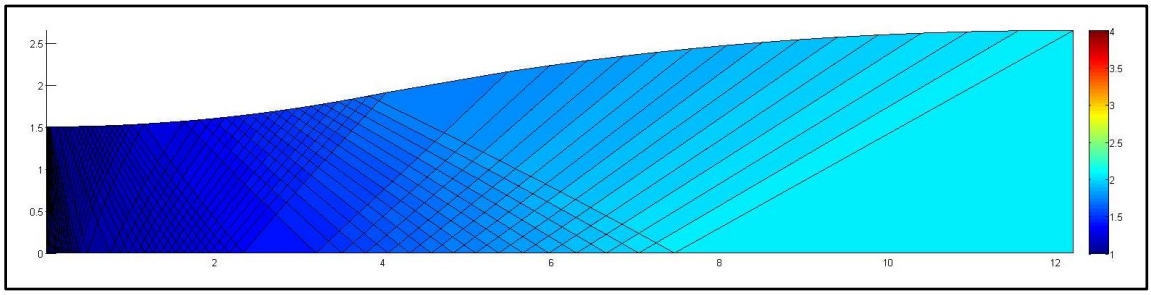

Figure 58: Mach 2.1 Wind Tunnel Nozzle MoC Solution

Appendix 5

WIND TUNNEL SOLID MODELS

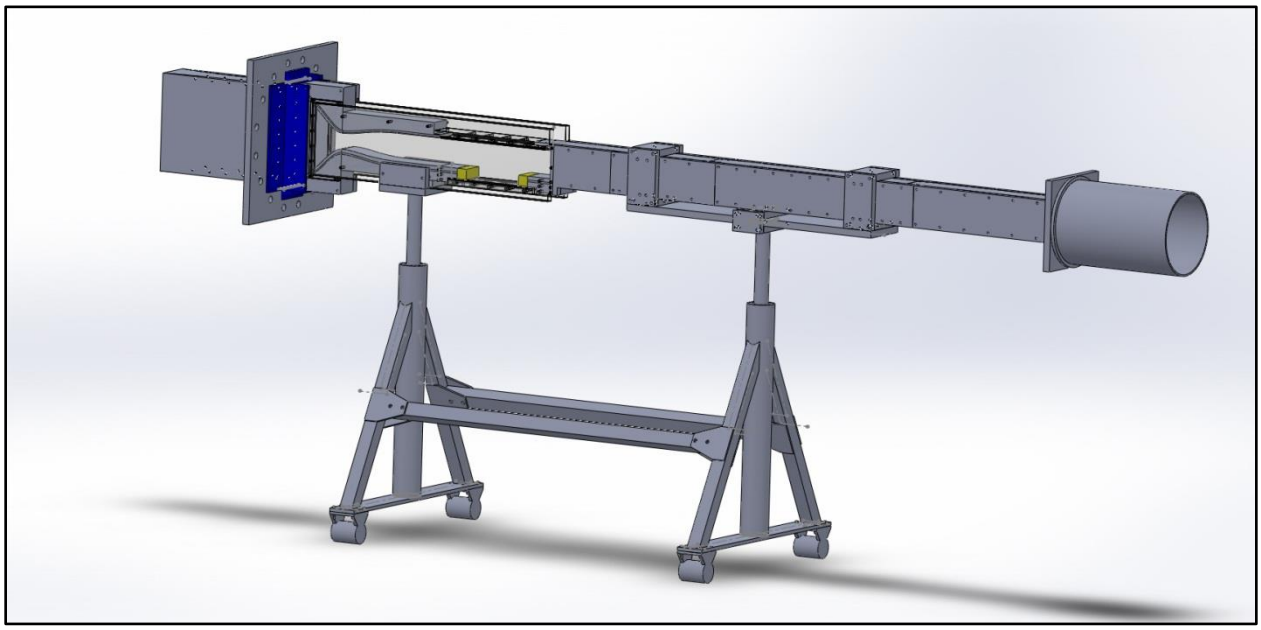

Figure 59: Complete Wind Tunnel Solid Model

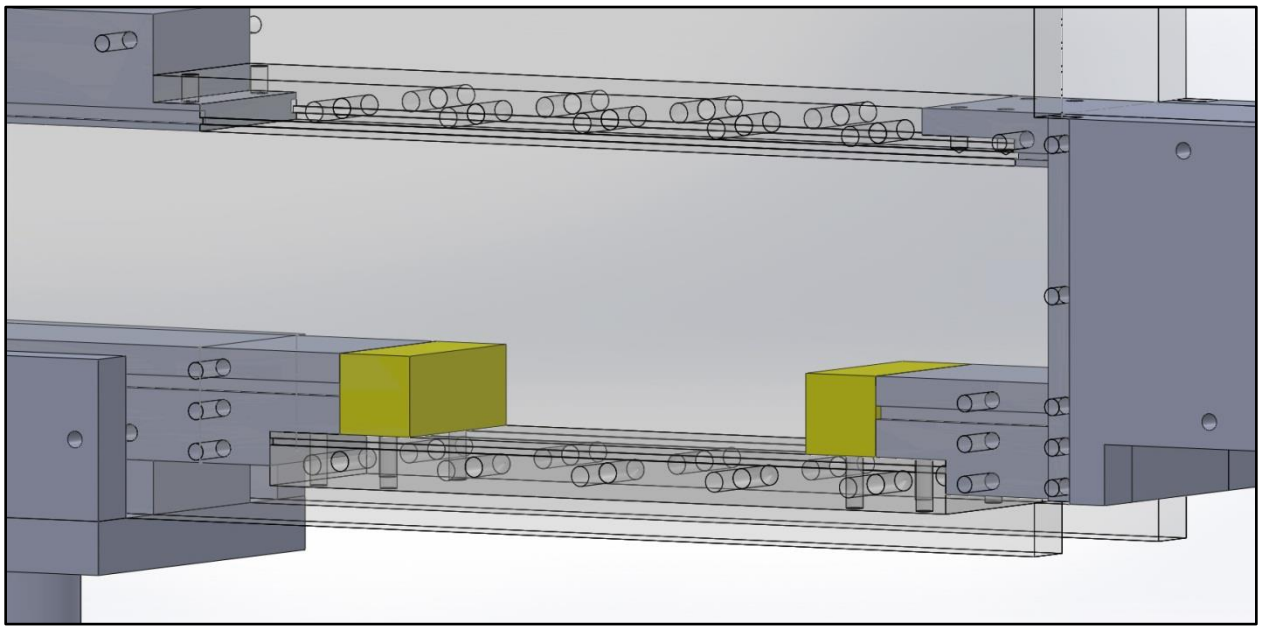

Figure 60: Cavity Solid Model

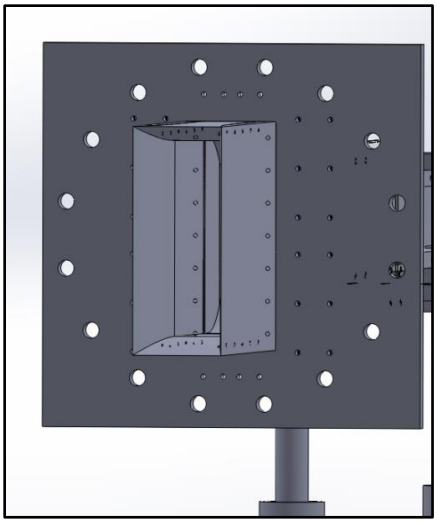

Figure 61: Forward Flange and Stagnation Guides

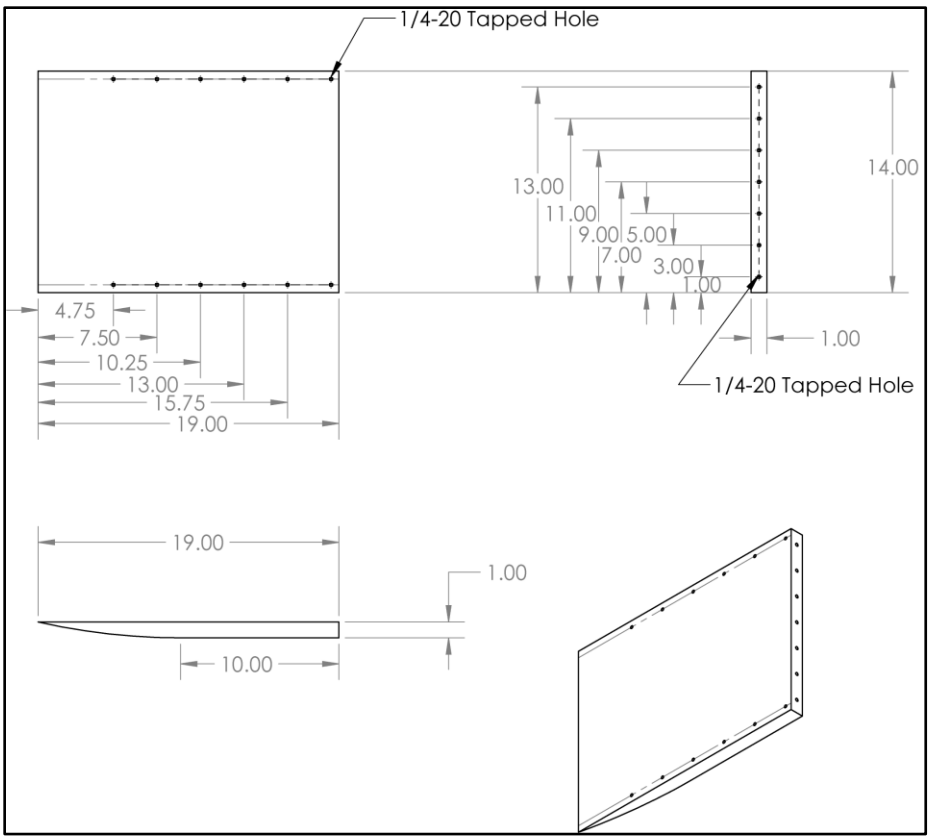

Figure 62: Vertical Stagnation Guide Drawing

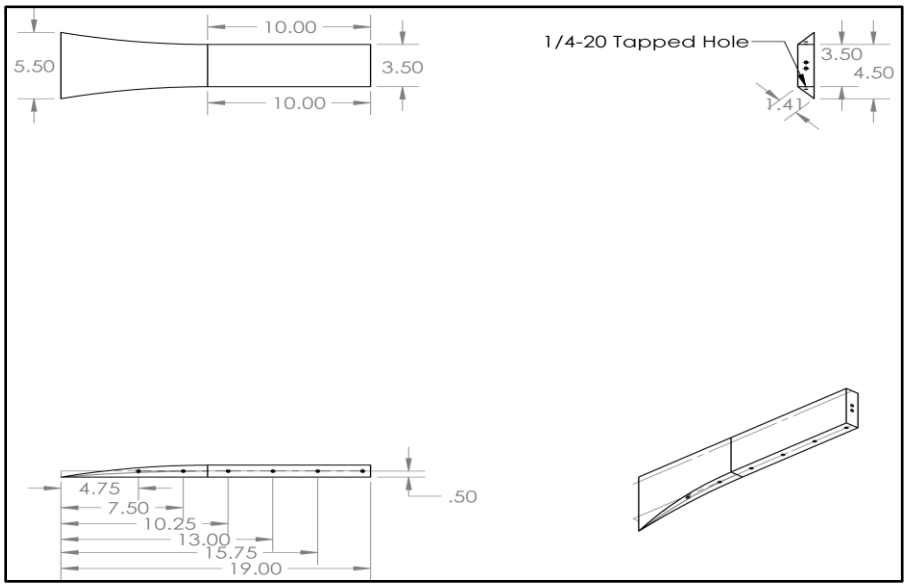

Figure 63: Horizontal Stagnation Guide Drawing

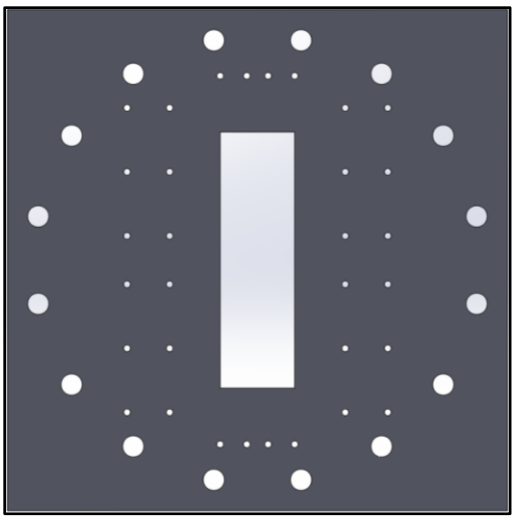

Figure 64: Forward Flange Solid Model

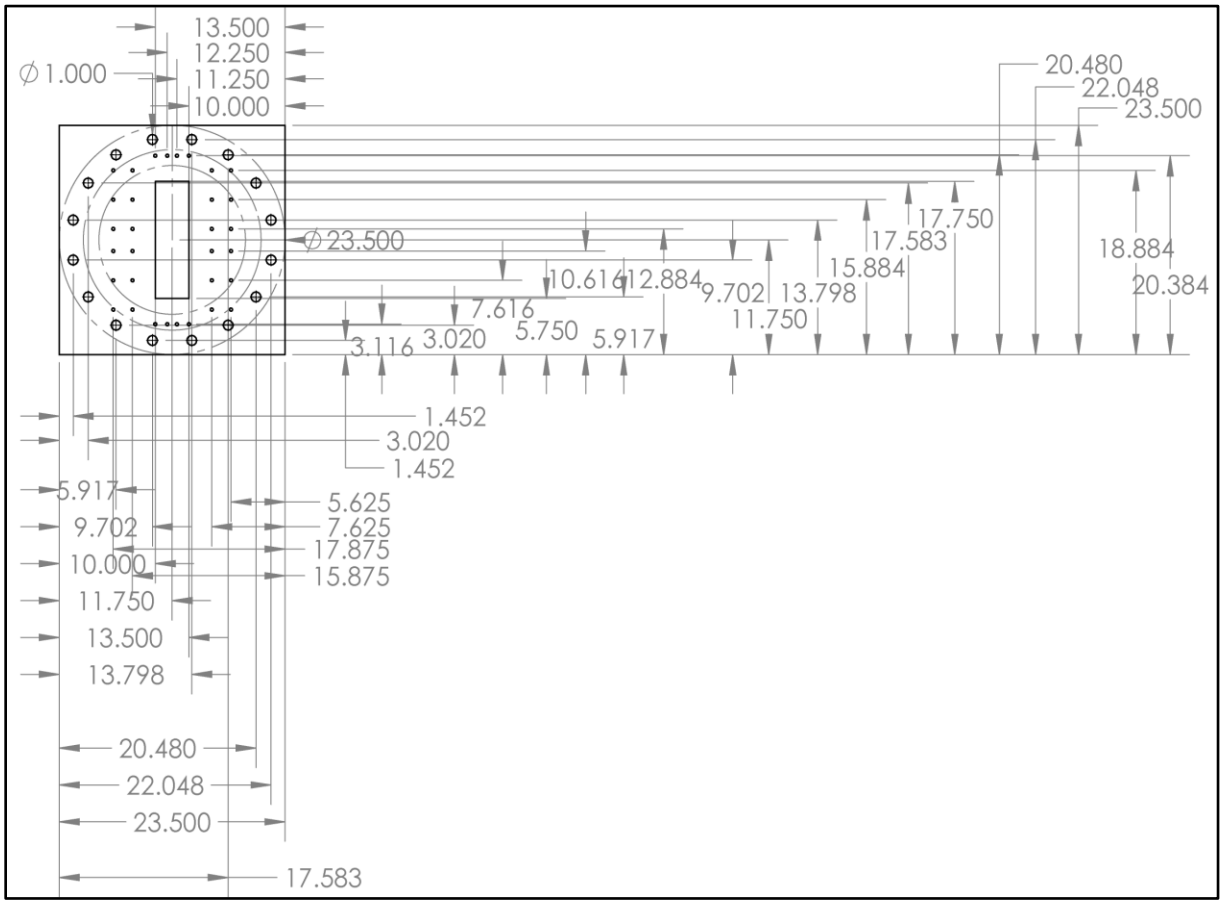

Figure 65: Forward Flange Drawing

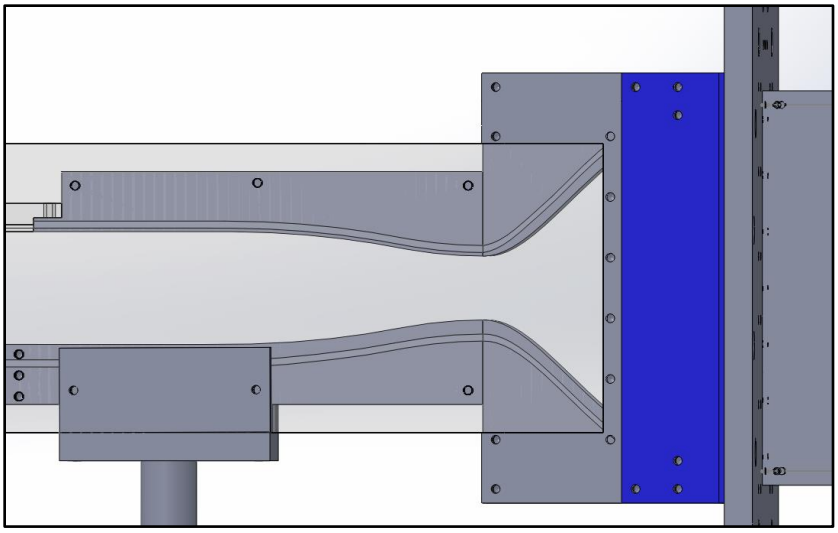

Figure 66: C-shaped Glass Housing Solid Model

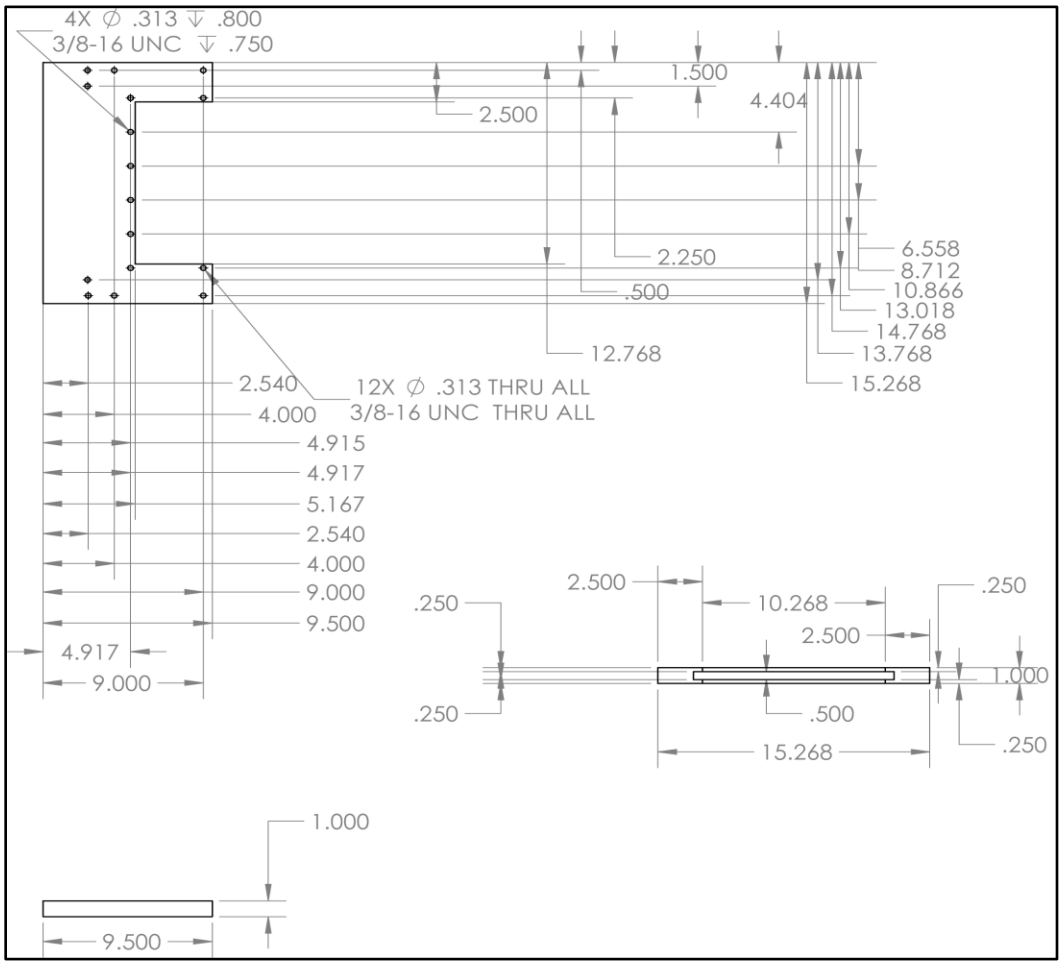

Figure 67: C-shaped Aluminum Glass Housing Drawing

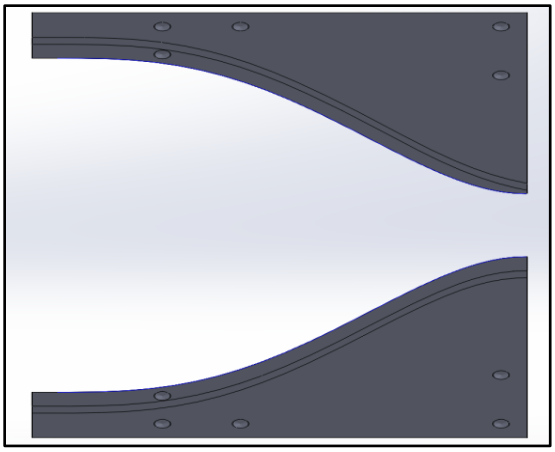

Figure 68: Subsonic Converging Section Solid Model

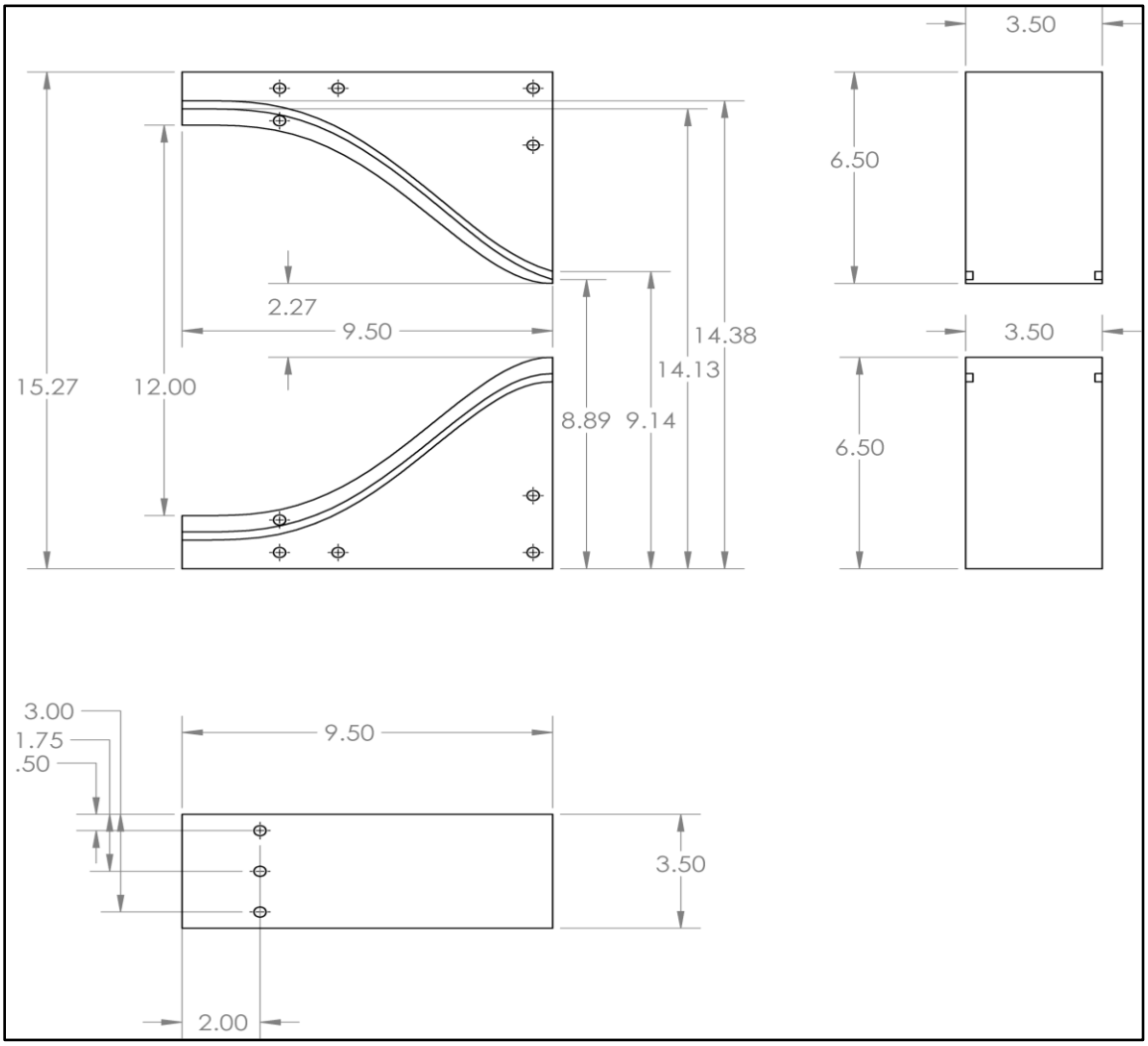

Figure 69: Subsonic Converging Section Drawing

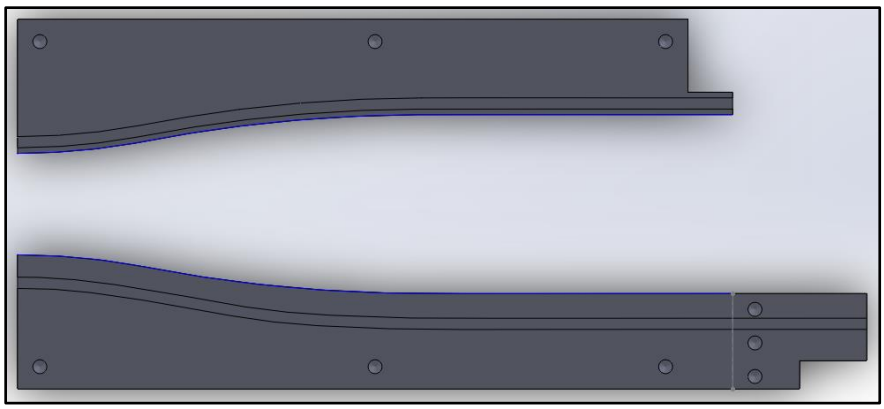

Figure 70: Supersonic Diverging Section Solid Model

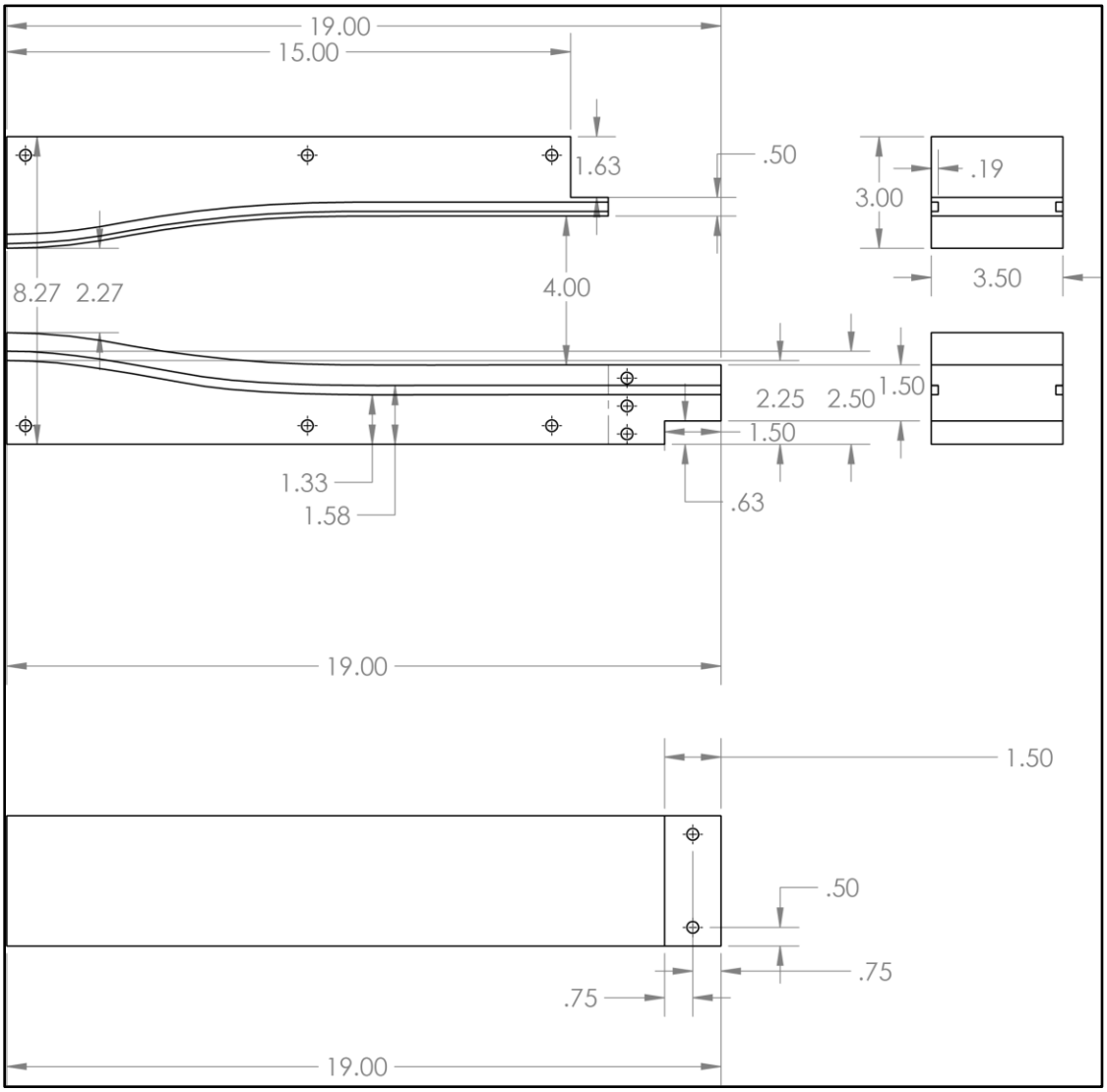

Figure 71: Supersonic Diverging Section Drawing

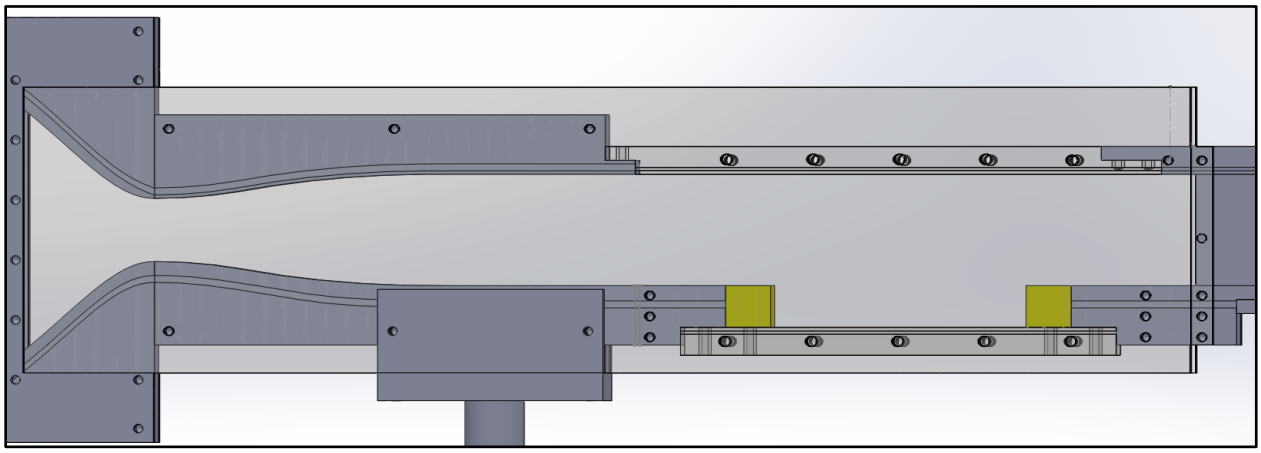

Figure 72: Solid Model Test Section View

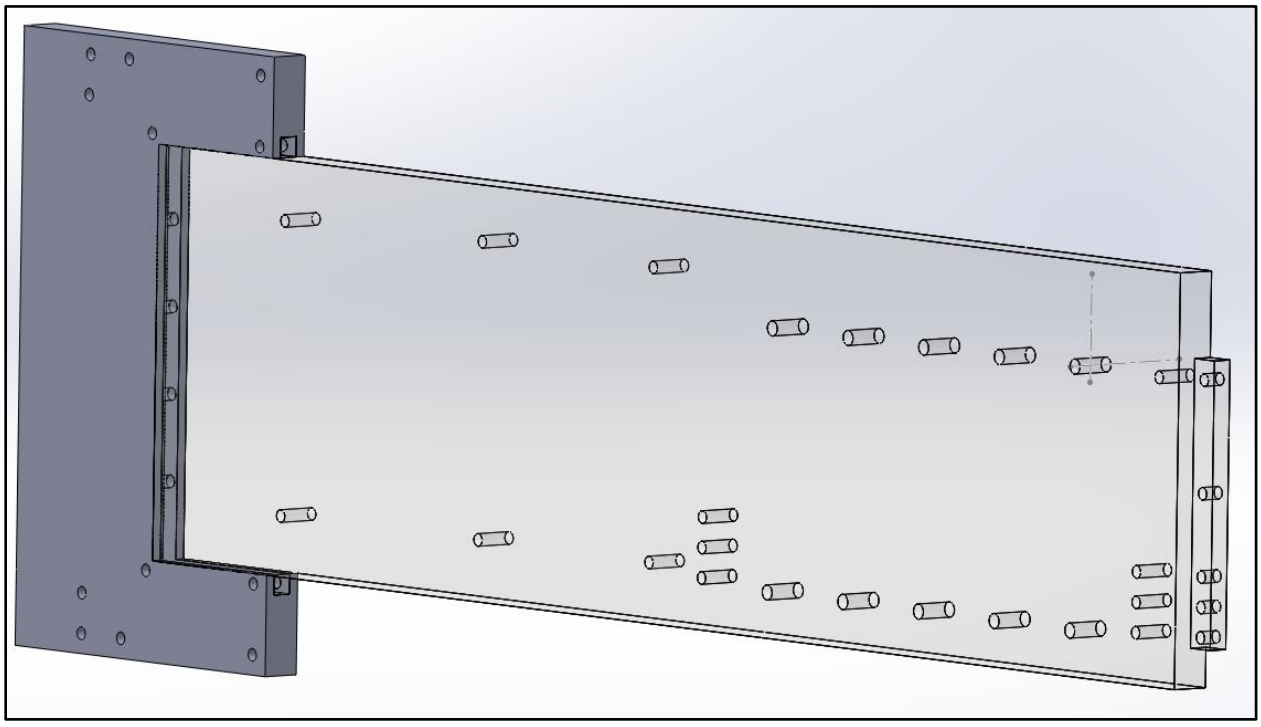

Figure 73: Left (top) and Right (bottom) Keyed Glass and Housing for Opposing Sides

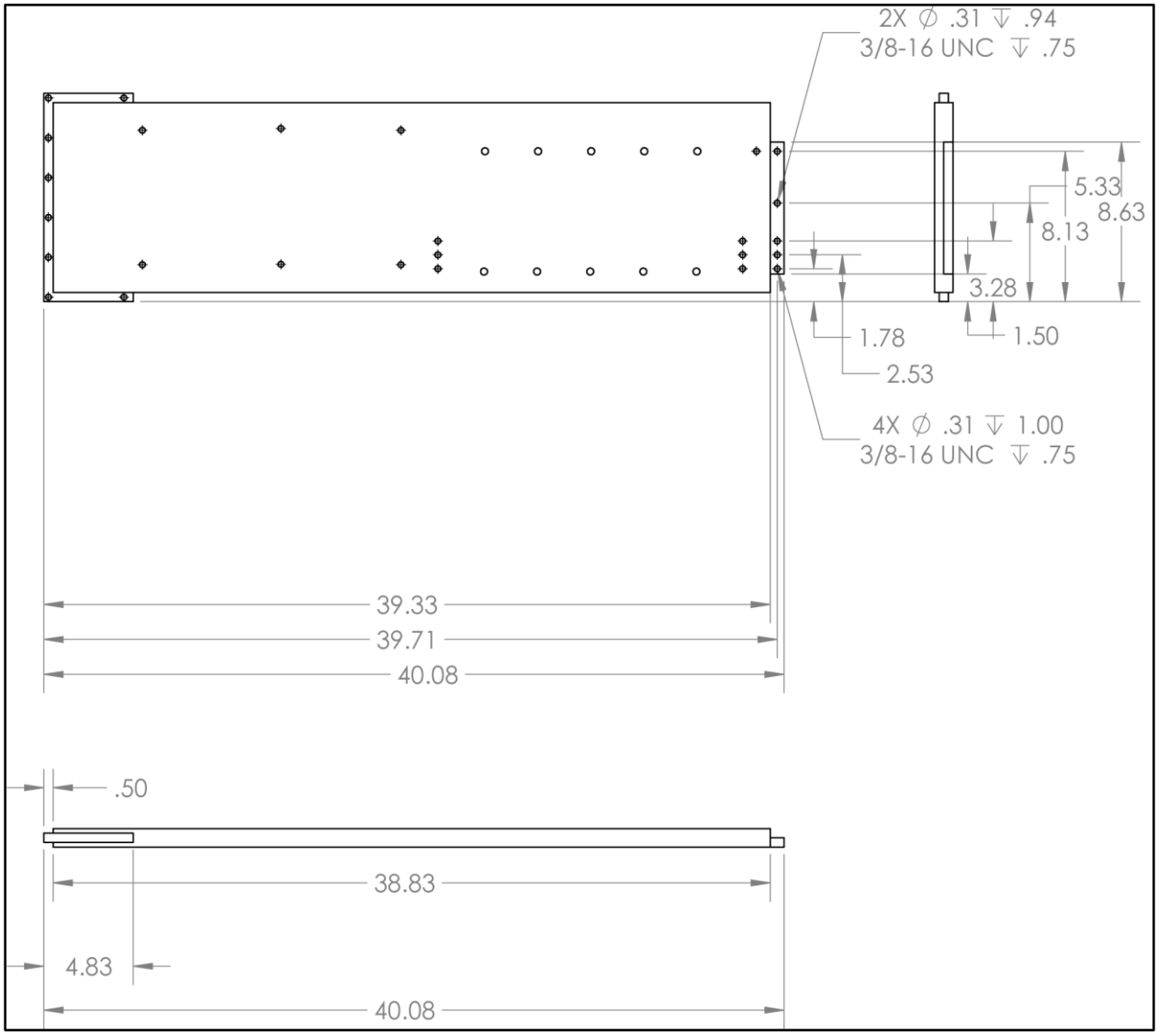

Figure 74: Optics Side Glass Drawing

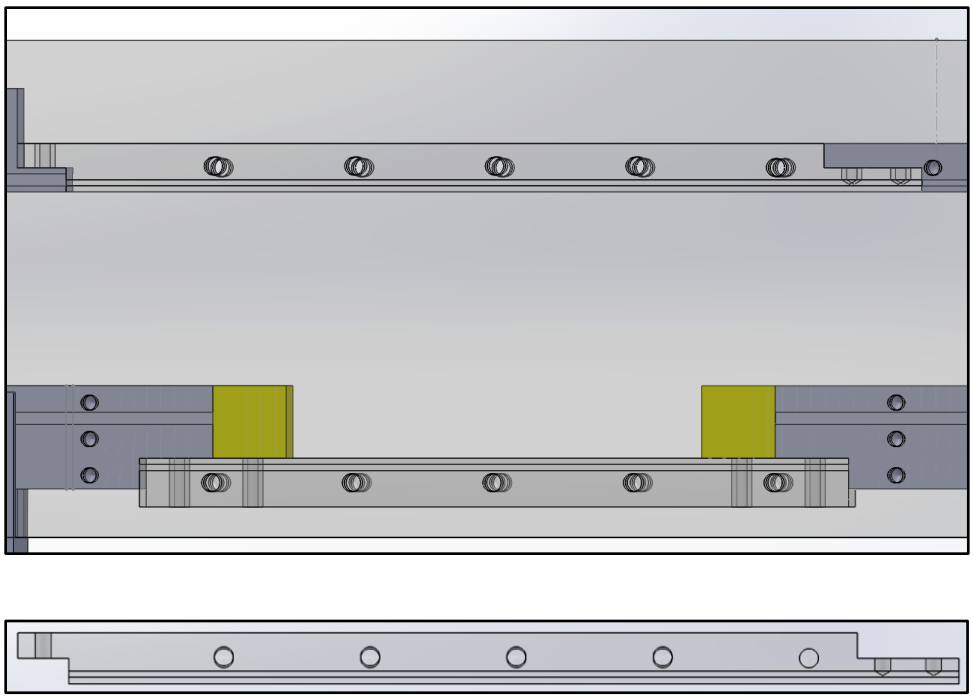

Figure 75: Cavity Ceiling Solid Model

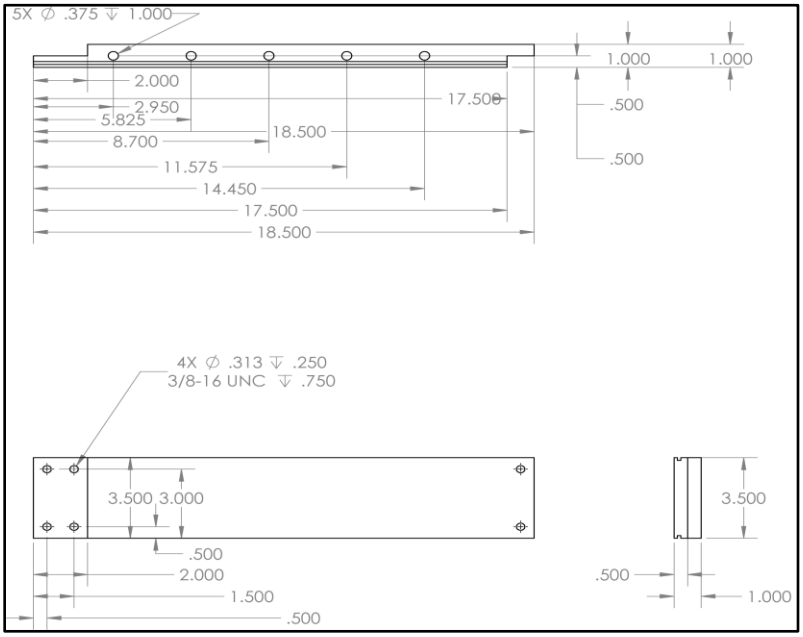

Figure 76: Cavity Ceiling Drawing

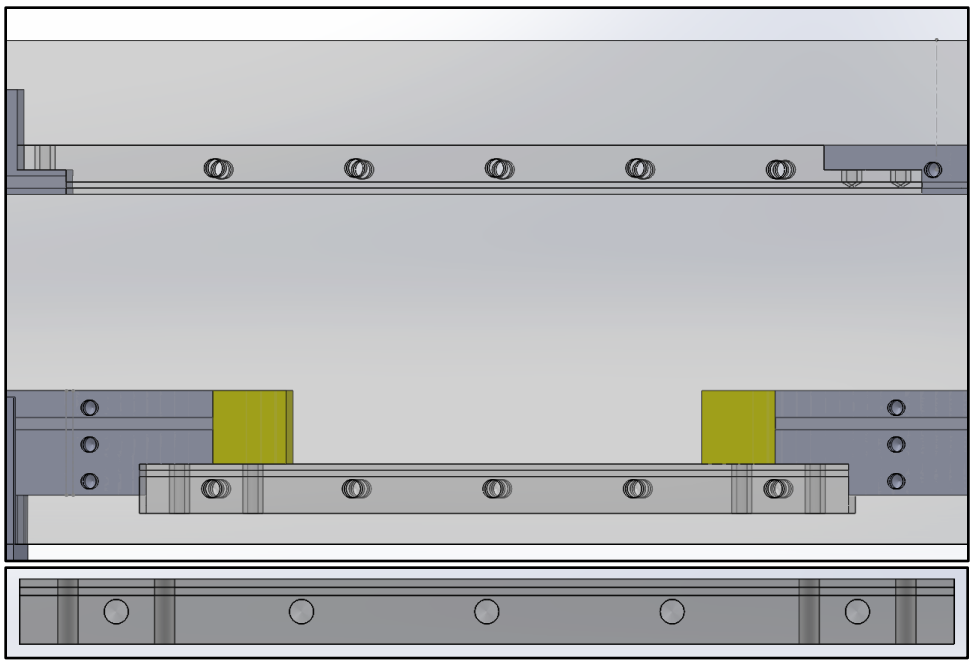

Figure 77: Cavity Base Solid Model

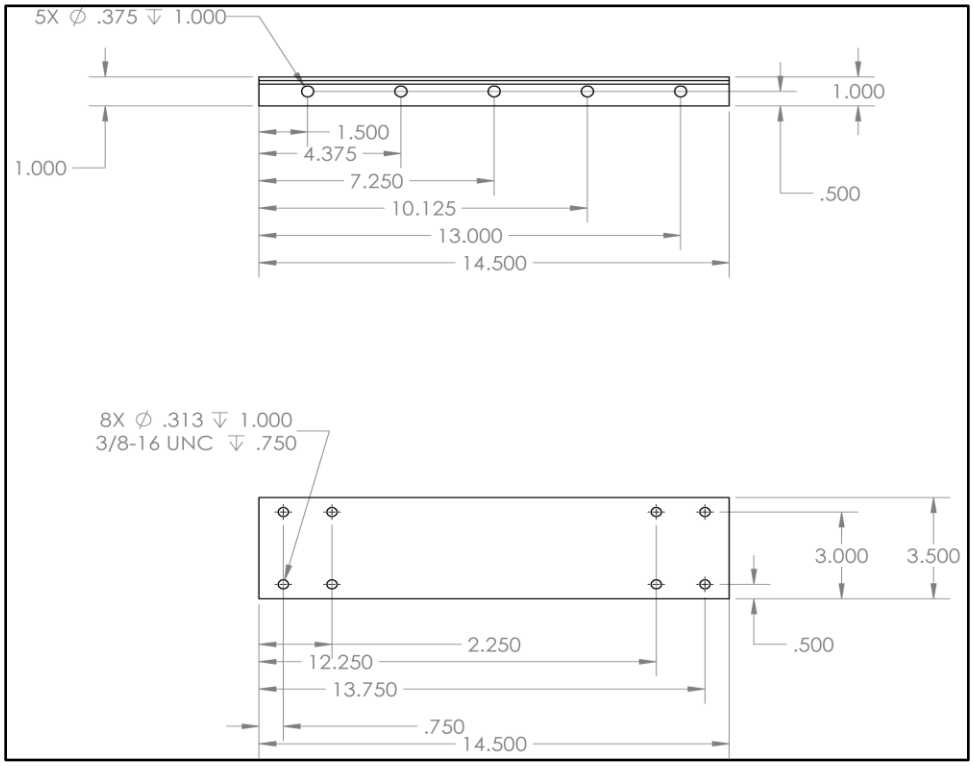

Figure 78: Cavity Base Drawing

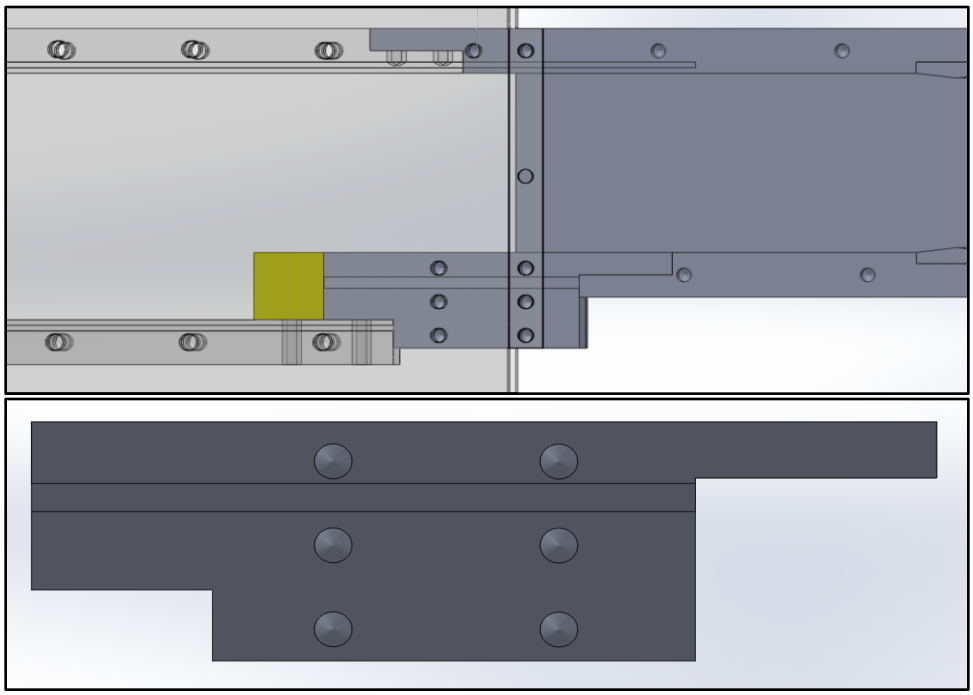

Figure 79: Tunnel Adapter Solid Model

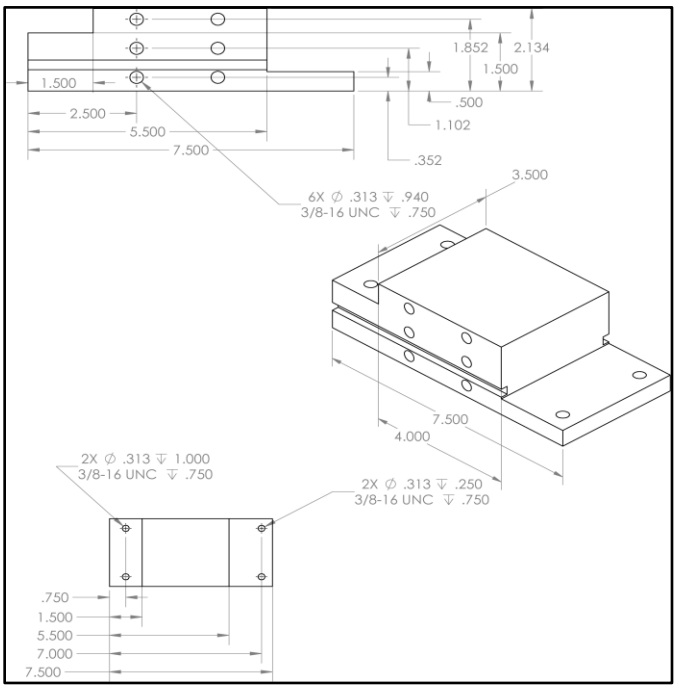

Figure 80: Tunnel Adapter Drawing

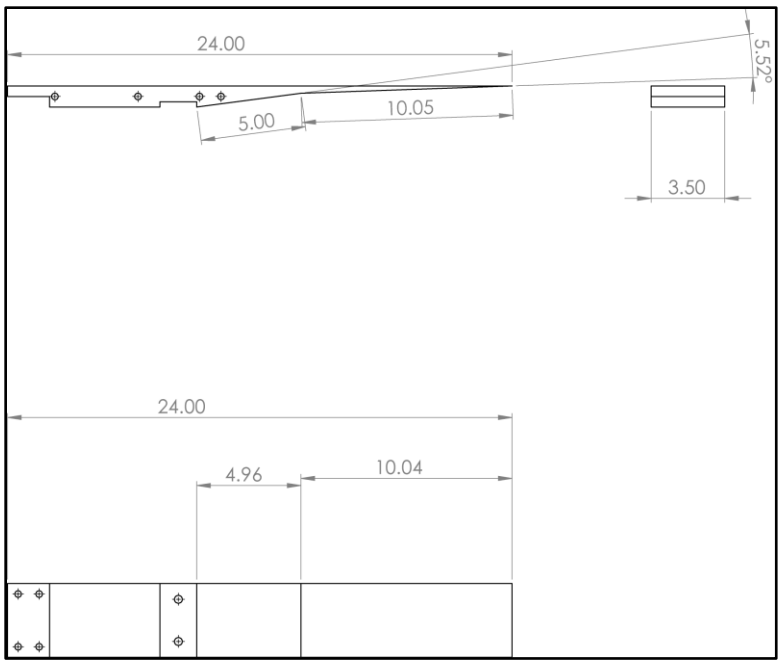

Figure 81: Diffuser Base Angled Housing For Diffuser Block, Drawing

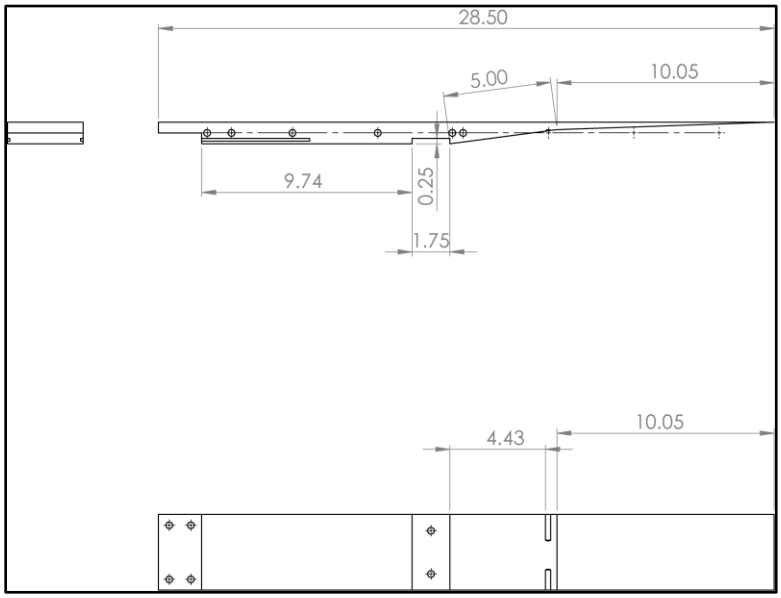

Figure 82: Diffuser Top Angled Housing for Diffuser Block, Drawing

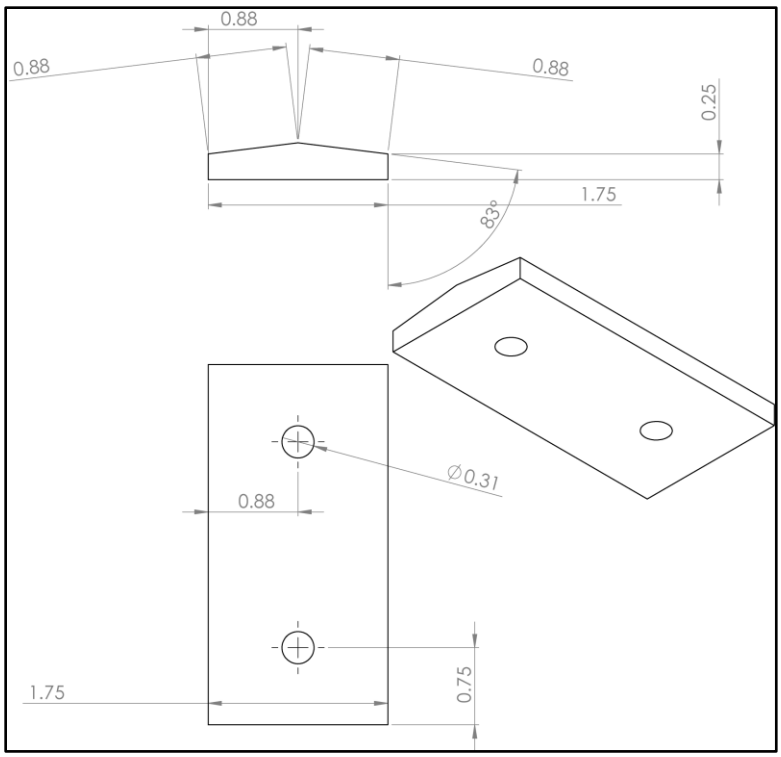

Figure 83: Diffuser Second Throat Sharp Blocks, Drawing

Appendix 6

SUPPORTING IMAGES

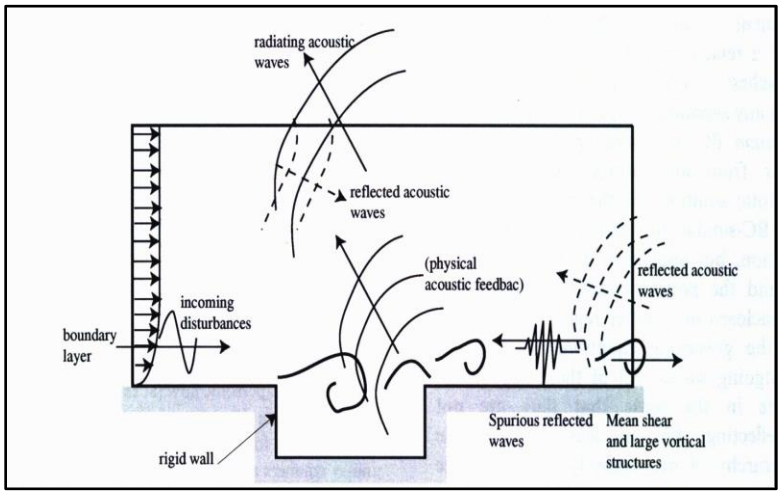

Figure 84: Sources of Acoustic Radiation

Appendix 7

MATLAB - ISENTROPIC WIND TUNNEL FLOW

The program Pertinent_Calculations.m calculated the values discussed in this thesis:

```
close all
clear all
clc

%Station 2 is where Mach 2 exists
%Station 1 is where Mach 1 exists ( i.e. Throat)

T_stagnation = 21.1111% Celsius equivalent to 70 F
T_stagnationK = 294.261 %Kelvin equaivalent to 70 F
P_stagnation = 416685.438 %Pascals equivalent to 60 psi
Rho_stagnation =P_stagnation/(287*T_stagnationK) %kg/m^3
%%
%isentropic variables for Mach 2
[MACH2, T2_Tstag, P2_Pstag, RHO2_RHOstag, A2_Astar] = flowisentropic(1.4, 2)

%isentroipic variables for Mach 1
[MACH1, T1_Tstag, P1_Pstag, RHO1_RHOstag, A1_Astar] = flowisentropic(1.4, 1)

%local values of temperature and pressure
%%
T1 = T1_Tstag*T_stagnation %Centigrade
T2 = T2_Tstag*T_stagnation %Centigrade

P2 = P2_Pstag*P_stagnation %Pascals
P1 = P1_Pstag*P_stagnation %Pascals

Rho2 = RHO2_RHOstag *Rho_stagnation %kg/m^3
Rho1 = RHO1_RHOstag *Rho_stagnation %kg/m^3

T1K = T1+273 %Kelvin
T2K = T2+273 %Kelvin

T1F=(1.8 * T1) + 32 %Farenheit
T2F=(1.8 * T2) + 32 %Farenheit

sound_speed1=sqrt(1.4*287*T1K) %m/s
sound_speed2=sqrt(1.4*287*T1K) %m/s

V1=MACH1*sound_speed1 %m/s
V2=MACH2*sound_speed2 %m/s
```

OUTPUT:
T_stagnation =
  21.1111
T_stagnationK =
 294.2610
P_stagnation =
  4.1669e+05
Rho_stagnation =
   4.9339
MACH2 =
    2
T2_Tstag =
   0.5556
P2_Pstag =
   0.1278
RHO2_RHOstag =
   0.2300
A2_Astar =
   1.6875
MACH1 =
    1
T1_Tstag =
   0.8333
P1_Pstag =
   0.5283
RHO1_RHOstag =
   0.6339
A1_Astar =
    1
T1 =
  17.5926
T2 =
  11.7284
P2 =
  5.3254e+04
P1 =
  2.2013e+05
Rho2 =
   1.1350
Rho1 =
   3.1278
T1K =
 290.5926
T2K =
 284.7284
T1F =

63.6667
T2F =
53.1111
sound_speed1 =
341.7018
sound_speed2 =
341.7018
V1 =
341.7018
V2 =
683.4035

The following code was used to generate the graphs discussed in this thesis and are repeated here: SUPERSONIC_MATLAB_CALCULATIONS.m

```
%12/1/2012
%Brian Davis  Thesis Calculations

%Conditions in the chamber
gamma=1.4 %ratio of specifiic heats cp/cv
P_stagnation=50 %psi
PascalstoPSI=6894.75729
P_stag= P_stagnation*PascalstoPSI %pascals
T_stagnationF=70%F
T_stagnationK=(T_stagnationF-32)*(5/9)
R=287%J/kgK
Rho_stag=P_stag/R*T_stagnationK%kg/m^3


%Nozzle Dimensions
TwoDnozzlewidthIN=3.5 % inches
Width_stagnationIN=12.0%inches
Width_throatIN=2.27 % inches
Width_NozExitIN=4.0 % inches
inches_meters=0.0254 % 1 inch equals 0.0254 meters
Width_stagnationM=Width_stagnationIN*inches_meters
Width_throatM=Width_throatIN*inches_meters
Width_NozExitM=Width_NozExitIN*inches_meters
TwoDnozzlewidthM=TwoDnozzlewidthIN*inches_meters

%Nozzle Areas
A_stagnationM2=Width_stagnationM*TwoDnozzlewidthM
A_throatM2=Width_throatM*TwoDnozzlewidthM
A_NozzleExit=Width_NozExitM*TwoDnozzlewidthM




%%
%CRITICAL PRESSURE
%--critical flow nozzles are also called sonic chokes.
%--the critical pressure ratio is the pressure ratio which will accelerate
%the flow to a velocity equal to the local velocity of sound in the fluid.
%By establishing a shock wave the sonic choke establishes a fixed flow rate
%unaffected by the differential pressure, any fluctuations or changes in
%the downstream pressure.

%the ratio between the critical pressure and the initial pressure for a
%nozzle is given by
```

```
pcritical_pstagnation = (2/(gamma+1))^(gamma/(gamma-1))%critical pressure ratio
critical_pressurePASCALS = pcritical_pstagnation*P_stag % Pa
critical_pressurePSI= critical_pressurePASCALS*(1/PascalstoPSI)

%from this we can calculate the mass flow at the particular point in the
%nozzle where the minimum pressure equals the critical pressure as long as
%there is sonic flow. This is the critical mass flow

mdot_critkgs=A_throatM2*(gamma*P_stag*Rho_stag)^(1/2)*(2/(gamma+1))^((gamma+1)/(2*(
gamma-1))) % mass flow at sonic flow in kg/s
% Because a supersonic wind tunnel requires a choked throat, the mass flow
% rate is considered to be constant at all points of operation


%%another mass flow rate calculation from
%http://www.wpi.edu/Pubs/E-project/Available/E-project-031410-175039/unrestricted/SWT-
MQP-JB3-SWT2.pdf
%page 37
counter4=1;
for Pstagn=20:0.1:80
   Pstagplot(counter4)=Pstagn;
   Pstagn2=Pstagn*PascalstoPSI;
mdot(counter4)=(Pstagn2*A_throatM2/sqrt(T_stagnationK))*sqrt((gamma/R)*(2/(gamma+1))^(
(gamma+1)/(gamma-1)));
counter4=counter4+1;
end
figure(4)
plot(Pstagplot,mdot)
xlabel('Stagnation Pressure PSI')
ylabel('mass flow kg/s')
grid on
grid minor



%% Pressure Ratio and Mach number
%The following plot illustrates how pressure ratio and Mach nummber vary
counter1=1
for MachRange=0:0.1:5
   MachNumber1(counter1)=MachRange
   PressureRatio(counter1)=(1+((gamma-1)/2)*MachRange^2)^(gamma/(gamma-1))
   counter1=counter1+1
end
figure(1)
plot(MachNumber1,PressureRatio)
xlabel('Mach Number')
```

```
ylabel('Pressure Ratio')
title('Pressure Ratio as a Function of Mach Number')
grid on
grid minor
 %By setting the Mach Number equal to 2  and implementing  and loking at
%total pressure
Ptotal_PMach2=(1+((gamma-1)/2)*2^2)^(gamma/(gamma-1))
counter2=1;
for Ptotal=1:0.1:100
   Pressure(counter2)=Ptotal/Ptotal_PMach2;
   Total_pressure(counter2)=Ptotal;
   counter2=counter2+1;
end
figure(2)
plot(Pressure,Total_pressure)
title(' A look at total pressure vs pressure at Mach 2 for Isentropic Flow')
xlabel('pressure')
ylabel('total pressure')
grid on
grid minor

%assuming that we were going to put a Pitot static Tube into the flow the
%following graph would illustrate the measurements visualized
%station 1 is before the shock
%station 2 is after the shock
counter3=1;
for MachRange2=1:0.1:5
part1=(gamma+1)/2;
part2=((gamma+1)^2*MachRange2^2)/(4*gamma*MachRange2^2-(2*(gamma-1)));
part3=1/(gamma-1);
Ptotal2_pressure1(counter3)=part1*part2^part3;
MachVar(counter3)=MachRange2;
counter3=counter3+1;
end
figure(3)
plot(MachVar,Ptotal2_pressure1)
title('Mach Number vs Pressure ratio of pressure after and Before Bow Shock on a Pitot Probe In
Supersonic Flow')
xlabel('Mach Number')
ylabel('Pressure ratio')
grid on
grid on
```

Appendix 8

MATLAB - MASS FLOW RATE FOR CHOKED FLOW & IDEAL DIFFUSER THROAT

```
close all
clear all
clc

STAGNATIONP= 344.7378645%kpa equal to 50 psi
k=1.4;
throatMach=1
[~,tempRatioIsenthroat, presRatioIsenthroat, ~, areaRatioIsenthroat] = flowisentropic(k,
throatMach);
PTHROAT=presRatioIsenthroat*STAGNATIONP%between 26 and 27 psi for 50 psi stagnation
disp('kpa')


steadyPicture = astsswtschematic('steady');
%diameter = 25/100;  % Diameter of the cross-section [m]
Nozzle_exitlentgth = 0.1016; %m= 4inches
Nozzle_exitwidth = 0.0889; %m=3.5 inches
height   = 214;    % Design altitude [m]
testMach = 2.0;     % Mach number in the test section [dimensionless]
k  = 1.4;        % Specific heat ratio [dimensionless]
cp = 1.004;     % Specific heat at constant pressure [kJ / (kg * K)]
testSectionArea = Nozzle_exitlentgth * Nozzle_exitwidth;
[testSectionTemp, testSectionSpeedOfSound, testSectionPressure, testSectionDensity] =
atmosisa(height);

% This function uses the following units:
%
% testSectionTemp = Static temperature in the test section        [K]
% testSectionSpeedOfSound = Speed of sound in the test section    [m / s]
% testSectionPressure = Static pressure in the test section       [kPa]
% testSectionDensity = Density of the fluid in the test section   [kg / m^3]


%% Calculation of the Stagnation Quantities
%
% You must calculate many of the stagnation (total) quantities in the test
% section. The ratios of local static conditions to the stagnation conditions
% can be calculated with flowisentropic.
[~,tempRatioIsen, presRatioIsen, ~, areaRatioIsen] = flowisentropic(k, testMach);
ENDNOZZLEP=presRatioIsen*STAGNATIONP% between 6 and 7 psi for 50 psi stagnation
disp('kpa')
%%
```

```
%All of the left hand side quantities are dimensionless ratios. Now we
%can use the ratio of static temperature to stagnation temperature
%to calculate the stagnation temperature.

testSectionStagTemp = testSectionTemp / tempRatioIsen;

%The optimum condition for steady-state operation of a supersonic wind
%tunnel with a fixed-area diffuser occurs when a normal shock is present
%at the diffuser throat. For optimum condition, the area of the diffuser
%throat must be smaller than the area of the nozzle throat. Assuming a
%perfect gas with constant specific heats, calculate the factor by which
%the diffuser area must be smaller than the nozzle area. This calculation
%is from a simplified form of the conservation of mass equation involving
%total pressures and cross-sectional areas:

%Calculate the total pressure ratio using the normal shock function
%from the Aerospace Toolbox:
[~, ~, ~, ~, ~, stagPressRatio] = flownormalshock(k, testMach);

%The area ratio at the shock is:
%We have the following expression using the conservation of mass


areaRatioShock = stagPressRatio;

%Calculate the area of the diffuser:

diffuserArea = testSectionArea / (areaRatioShock * areaRatioIsen);

%Because the diffuser throat area is smaller than the
%test section area, the Mach number of the flow must converge
%toward unity. Using flowisentropic with the area ratio as the input,
%calculate the Mach number just upstream of the shock:

diffuserMachUpstreamOfShock = flowisentropic(k, (1 / areaRatioShock), 'sup');

%Use flownormalshock to calculate the flow properties through the shock
%wave. Note, here again, we will only need the total pressure ratio:

[~, ~, ~, ~, ~, P0] = flownormalshock(k, diffuserMachUpstreamOfShock);


massFlowRate = testSectionDensity * testSectionArea * testMach * testSectionSpeedOfSound %
[kg / s]
disp('kg/s')
```

```
%Calculation of Work and Power Required for the Steady State Case

%The work done by the compressor per unit mass of fluid equals the
%enthalpy change through the compressor. From the definition of enthalpy,
%calculate the specific work done by knowing the temperature change and
%the specific heat of the fluid at constant pressure:

%Temperature into the compressor is the same as the test section stagnation
%temperature
tempDiff = testSectionStagTemp * ((1 / P0)^((k - 1) / k) - 1); % [K]

%Specific Work

specificWork = cp * tempDiff; % [kJ / kg]

%The power required equals the specific work times the mass flow rate.
%During steady-state operation, the mass flow rate through the
%test section is given by: all flow quantities are the values in the test
%section:

massFlowRate = testSectionDensity * testSectionArea * testMach * testSectionSpeedOfSound;
% [kg / s]

%Power required by the compressor in the steady state operation
powerSteadyState = specificWork * massFlowRate;  % [kW]
%Calculating Work and Power Required During Startup
startupPicture = astsswtschematic('startup');
%For the startup condition the shock wave is in the test section.
%The Mach number immediately before the shock wave is
%the test section Mach number.
[~, ~, ~, ~, ~, stagPressRatioStartup] = flownormalshock(k, testMach);
%Now, calculate the specific work of the isentropic compressor.
specificWorkStartup = cp * testSectionStagTemp * ((1 / stagPressRatioStartup)^((k - 1) / k) - 1);
% [kJ / kg]
%Then, calculate the power required during startup:
powerStartup = specificWorkStartup * massFlowRate;   % [kW]
%These power required results represent the optimum
%and worst-case operation conditions, respectively.
% power = [powerSteadyState powerStartup];
% barGraph = figure('name','barGraph');
% bar(power,0.1);
% ylabel('Power required [kilowatts]')
% set(gca,'XTickLabel',{'powerSte
```

APPENDIX 8

THOR LABS INSTRUMENTATION

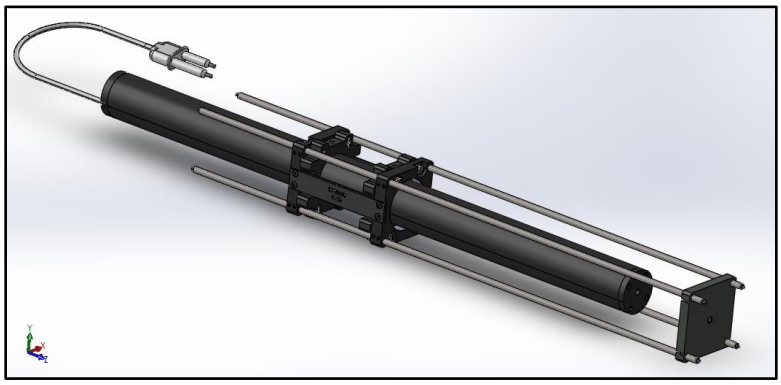

Figure 85: Thor Labs Light Source Custom Assembly

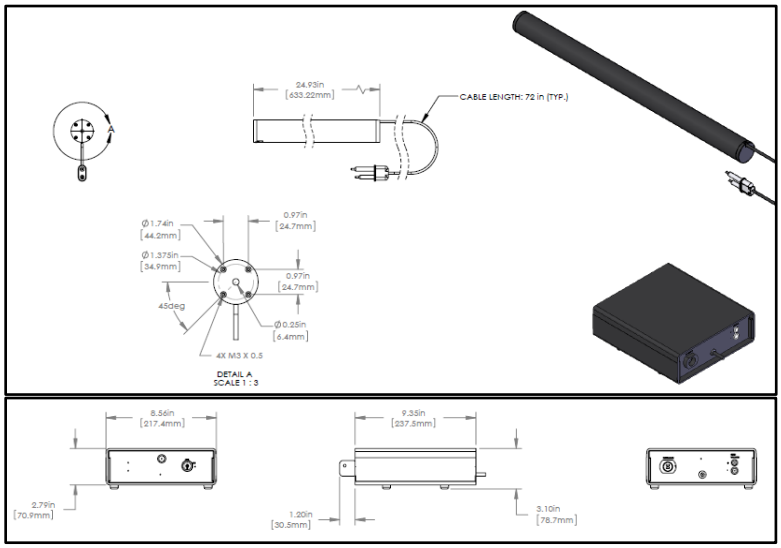

Figure 86: Thor Labs Coherent Laser Light Source [53]

Figure 87: Thor Labs HCM2- XY Mount for 60mm Cage System [53]

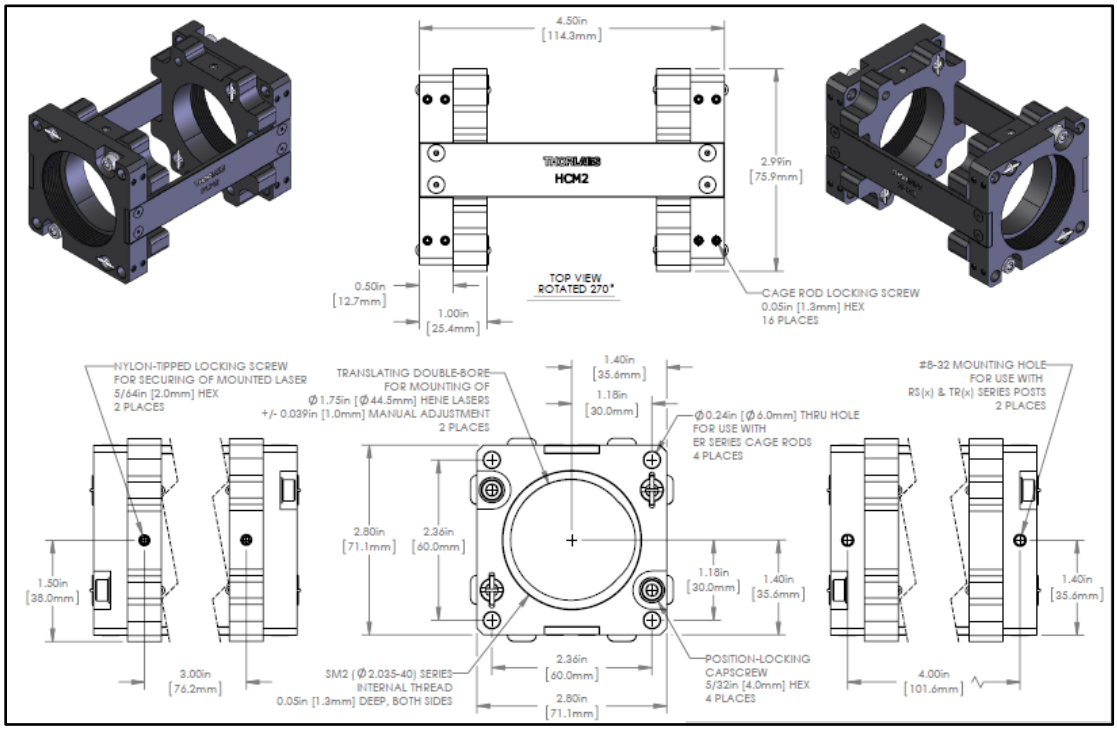

Figure 88: Thor Labs HCM2- XY Mount for 60mm Cage System, Drawing [53]

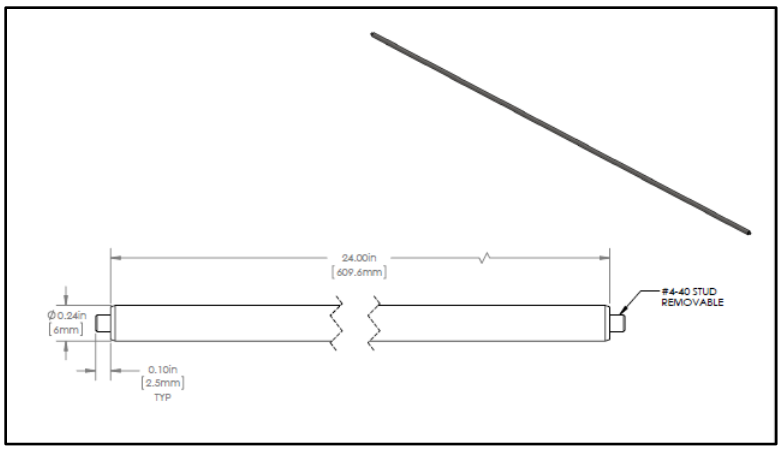

Figure 89: Thor Labs ER24- 24 in Cage Assembly Rod, Drawing [53]

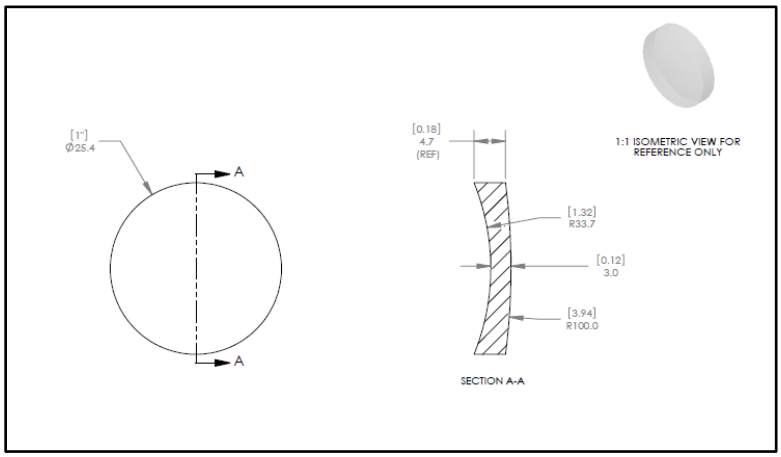

Figure 90: Thor Labs LF1822 –f =-100.0 mm, Ø1” Meniscus Lens, Drawing [53]

Figure 91: Thor Labs LA1540-A-ML -Ø1/2” Plano Convex Lens f=15.0 millimeter, Image [53]

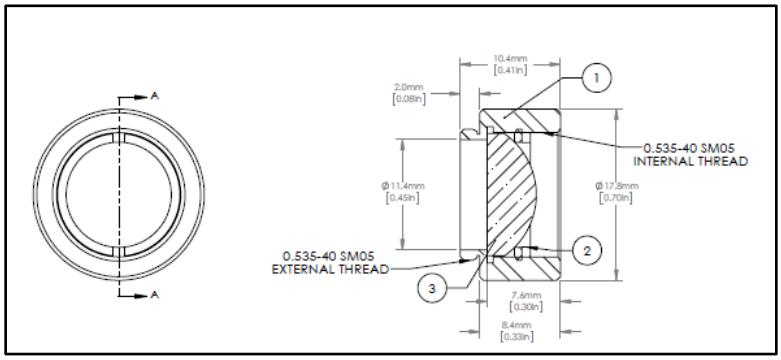

Figure 92: Thor Labs LA1540-A-ML -Ø1/2” Plano Convex Lens, f=15.0 mm, Drawing [53]

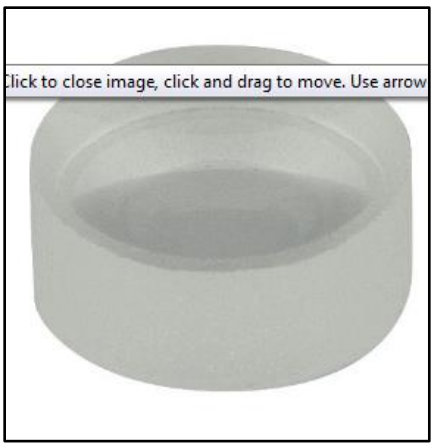

Figure 93: Thor Labs LD2746-N-SF11 Bi-Concave Lens, Ø6mm f=-6.0mm, Image [53]

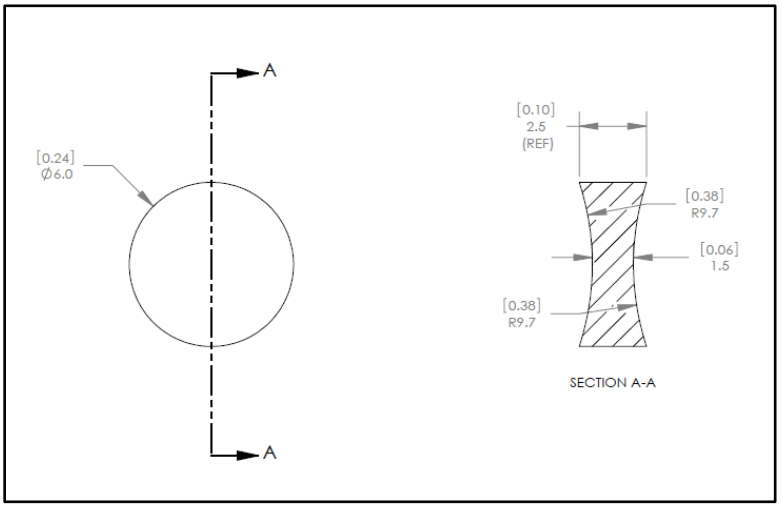

Figure 94: Thor Labs LD2746-N-SF11 Bi-Concave Lens, Ø6mm f=-6.0mm, Drawing [53]

Figure 95: Thor Labs LCP02 - 60mm Cage Plate Adapter Image [53]

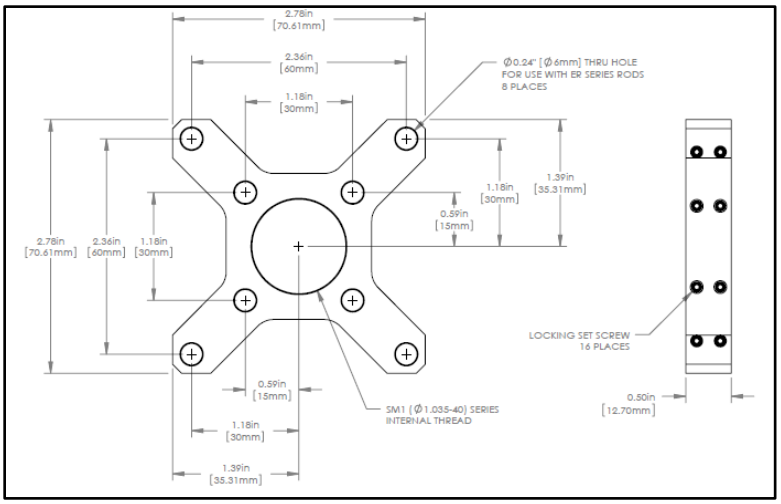

Figure 96: Thor Labs LCP02 - 60mm Cage Plate Adapter Drawing A [53]

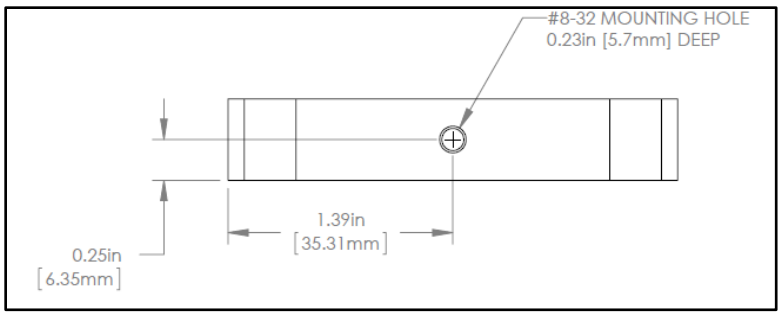

Figure 97: Thor Labs LCP02 - 60mm Cage Plate Adapter Drawing B [53]

Figure 98: Thor Labs SM1A6- Adapter, 0.15” Thick Image [53]

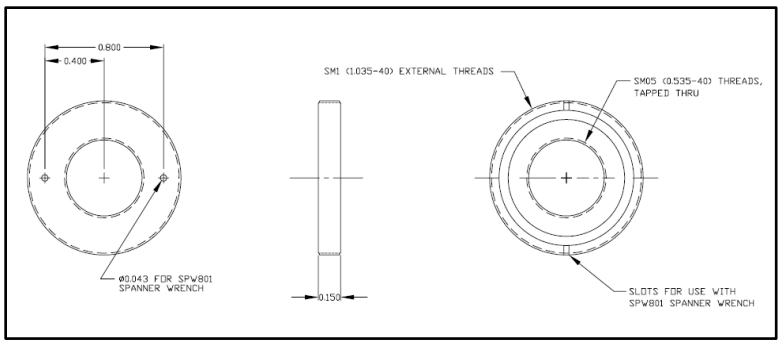

Figure 99: Thor Labs SM1A6- Adapter, 0.15” Thick Drawing [53]

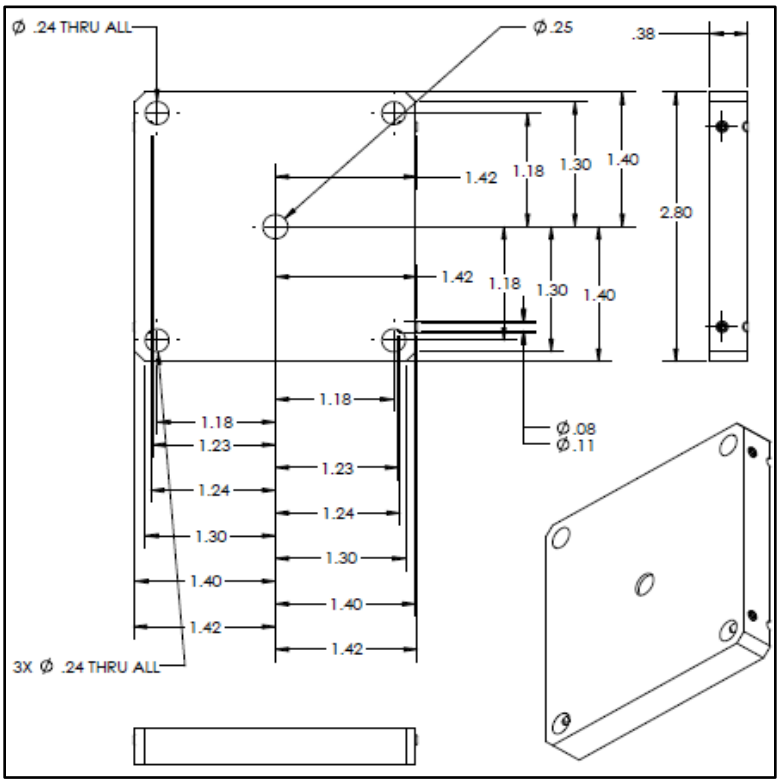

Figure 100: Custom Designed Cage Plate for 6mm Optics Drawing

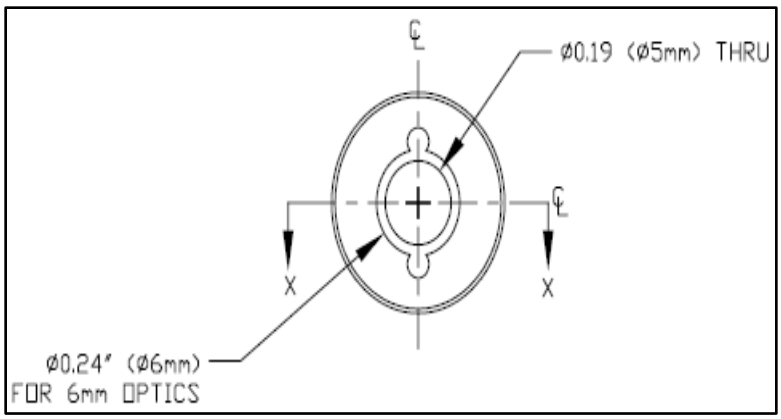

Figure 101: Thor Labs LMRA6 Drawing A [53]

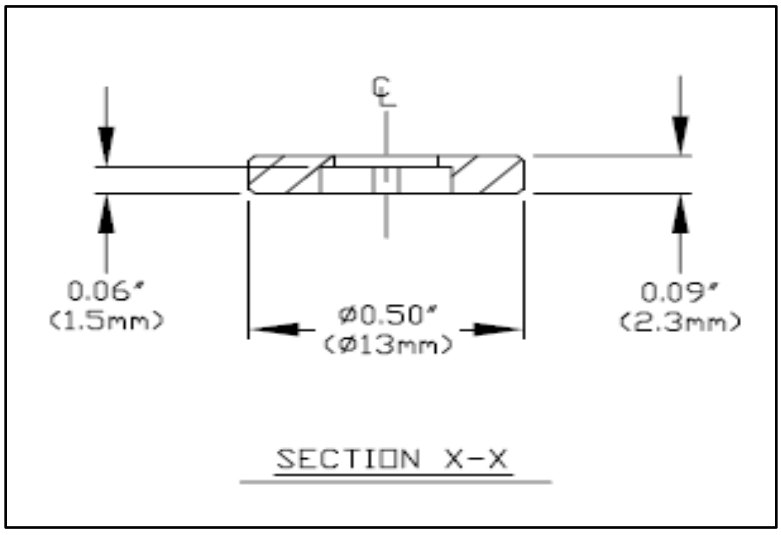

Figure 102: Thor Labs LMRA6 Drawing B [53]